Dissertation

submitted to the

Combined Faculty of Mathematics, Engineering and Natural Sciences

of

Heidelberg University, Germany

for the degree of

Doctor of Natural Sciences

Put forward by

Tim Sailer

born in Villingen-Schwenningen

Oral examination: February 16, 2022

Direct Bound-Electron *g*-Factor Difference Measurement of Coupled Ions at ALPHATRAP

Referees: Prof. Dr. Klaus Blaum

PD. Dr. Wolfgang Quint

Direct Bound-Electron *g*-Factor Difference Measurement of Coupled Ions at ALPHATRAP

Abstract – The ALPHATRAP experiment is a cryogenic Penning-trap setup with the main objective to determine the *g* factor of the electron bound to heavy nuclei. Within this thesis, the results of several such measurements are presented. Among these, the measurement of the *g* factor of $^{20}\mathrm{Ne}^{9+}$ exhibits a 3σ discrepancy between theory and experimental value, which has been attributed to the required input parameter of the atomic mass of $^{20}\mathrm{Ne}$. An independent measurement has recently confirmed the deviation of the mass, fully resolving the discrepancy. Furthermore, a measurement of $^{22}\mathrm{Ne}^{9+}$ can be used to improve the precision of the atomic mass of $^{22}\mathrm{Ne}$ by a factor 8 compared to the literature value, when using the theoretically predicted *g* factor as an input. However, the main focus of this thesis is the development of a novel technique, which, based upon the coupling of two ions as an ion crystal, enables the most precise determination of a *g*-factor difference to date. This difference, determined for the isotopes $^{20}\mathrm{Ne}^{9+}$ and $^{22}\mathrm{Ne}^{9+}$ with a relative precision of 5.6×10^{-13} with respect to the *g* factor, improves the precision for isotopic shifts of *g* factors by about two orders of magnitude. Based upon the agreement with theory, the quantum electrodynamic contribution to the nuclear recoil can be confirmed. Alternatively, the result can be applied to improve the precision of the charge radius difference of the isotopes by about one order of magnitude or to constrain new physics by limiting a potential fifth-force of the Higgs-portal mechanism.

Direkte g-Faktor Differenzmessung des gebundenen Elektrons von gekoppelten Ionen in ALPHATRAP

Zusammenfassung – Das ALPHATRAP Experiment ist ein kryogener Penningenfallen Aufbau mit dem Hauptziel, den g Faktor des an schwere Kerne gebundenen Elektrons zu messen. In dieser Arbeit werden die Ergebnisse von mehreren solcher Messungen präsentiert. Bei einer dieser, weist die Messung des g Faktors von $^{20}\mathrm{Ne}^{9+}$ eine 3σ Diskrepanz zwischen Theorie und experimentellem Wert auf, die der als Eingangsparameter benötigten atomaren Masse von $^{20}\mathrm{Ne}$ zugeschrieben wurde. Eine unabhängige Messung konnte kürzlich die Abweichung der Masse bestätigen und damit die Diskrepanz gänzlich auflösen. Weiterhin kann eine Messung des g Faktors von $^{22}\mathrm{Ne}^{9+}$ dazu verwendet werden, die Genauigkeit der atomare Masse von $^{22}\mathrm{Ne}$ um einen Faktor 8 gegenüber dem Literaturwert zu verbessern, wenn die theoretische Vorhersage des g Faktors als Eingangsparameter verwendet wird. Der Schwerpunkt dieser Arbeit liegt jedoch auf der Entwicklung einer neuartigen Technik, welche, basierend auf der Kopplung zweier Ionen zu einem Ionenkristall, die bislang genauste Messung einer g Faktor Differenz ermöglicht. Diese Differenz, gemessen für die Isotope von $^{20}\mathrm{Ne}^{9+}$ and $^{22}\mathrm{Ne}^{9+}$ mit einer relativen Genauigkeit von 5.6×10^{-13} bezüglich des g Faktors, verbessert die Genauigkeit der Isotopieverschiebung von g Faktoren um ungefähr zwei Größenordnungen. Basierend auf der Übereinstimmung mit der Theorie kann der quantenelektrodynamische Beitrag zum Kernrückstoß verifiziert werden. Alternativ kann das Ergebnis verwendet werden, um entweder die Genauigkeit der Ladungsradiendifferenz der Isotope um eine Größenordnung zu verbessern oder um Einschränkungen für neue Physik zu liefern, indem eine mögliche fünfte Kraft des Higgs-Portal Mechanismus limitiert wird.

Contents

List of Figures

Introduction

The Simple Picture

As a side-effect of my PhD time over the last four years, I have gained certain insights on how to best explain what I have been working on to non-physicists.

The main gist of working with a Penning trap as a tool to store and work with single charged particles in electric and magnetic fields for several months seems to be general enough to understand. At this point it becomes slightly more complicated, as the electron spin has to be introduced. This works well, when over-simplified to picture the electron as a *rotating* charged sphere, but is less helpful when explaining that classical physics fails to predict the implications of such an assumed rotation already by about a factor of 2 – the so-called g factor.

Therefore, it has proven to work significantly better to simplify and explain our measurements as to *how magnetic an electron is*, which is expressed by the g factor. The purpose of this work can than be summarized as the hunt to measure the precise deviation of the g factor from 2, which is where relativistic corrections and quantum electrodynamics (QED) enter. The theory of QED is best described as the theory of interaction between light and matter and manages to predict this value to extreme precision. This unfailingly results in the follow-up question, why this value is of such importance to justify all of my work.

Well, that's where you can begin to smile as your listener has now entered the realm of physicists. We do not care about the *exact* value. We do however care about how *precise* this value can be determined. This becomes important when considering the aforementioned prediction of the g factor by theoretical calculations based upon QED, in the framework of the Standard Model (SM) of particle physics. As it is now possible to compare the measured value with the prediction, the combined precision for theory and experimental values directly yields a benchmark for the performance of QED.

This concept is the defining principle of much of the work performed in physics in general – taking a theory and testing it with ever increasing precision until a deviation might be observed.

While there are many reasons why such a search is of interest, the most straightforward one might be the missing explanation for the imbalance between existing matter and anti-matter. The current SM predicts a symmetry, or at least a much better balance, for the existence of both. Therefore, having such a discussion in an obviously existing universe whose very existence is not explained by a theory that otherwise works rather well, should be motivation enough to try to advance our understanding.

If this is not yet convincing enough, and your listener is astronomically inclined, the observations of dark matter [1] and dark energy [2] are related to the movement of astronomical bodies, that cannot be explained by the gravity of the observable mass alone, which has already been pointed out almost 150 years ago by Lord Kelvin [3]. Despite dedicated experiments [4], no conclusive signal to allow for a direct detection of such dark matter could be observed yet. This is intriguing, as its very existence might influence properties of atoms and ions, for example again the g factor. As the coupling to *normal* matter for such an influence is expected to be extremely weak or would already have been observed otherwise, precision measurements are required. Within this thesis, I will show that specifically the difference of g factors is a sensitive probe for new physics, that goes beyond the current SM. Such a g-factor difference and the methods I have developed to access it with unprecedented precision and finally the results of this measurement are the main topic covered within this thesis.

Testing QED and the Hunt for Precision

The SM is considered to be the most complete theory of physics, as it currently combines three of the four known forces of our universe in a unified model of quantum field theories. While this works astoundingly well for the electromagnetic, weak and strong force, the gravitational force resists these unification attempts into a single such framework and can only be described by general relativity.

Within the SM, the most stringently tested theory is QED, which describes the interaction of charged particles and electromagnetic fields by means of exchanges of photons. This theory links different fields of physics by predicting experimentally accessible values. This began with the introduction of QED to explain the observed Lamb shift [5] in the fine-structure of hydrogen and culminates in the spectroscopy of the $1S - 2S$ transition in hydrogen [6].

Furthermore, one of the properties that can be predicted by this theory is the g factor of the electron, which expresses the magnetic moment of an electron in terms of the Bohr magneton. The measurement of the free electron g factor [7] in combination with QED theory [8], yields one of the most precise values for the fine-structure constant α. The agreement of the thus extracted fine-structure constant, based upon the framework of the SM, with the measured fine-structure constant via a recoil measurement of rubidium atoms [9] yields a stringent test for QED and confirms the electron to be an elementary particle without substructure, as the value would have to differ if that were the case [10]. It has to be noted however, that there is still an open question left as a 5σ discrepancy from the value obtained in the rubidium measurement compared to the fine-structure constant obtained in caesium recoil measurements [11] is currently unexplained. Another improved determination of the fine-structure constant could help to resolve this discrepancy. Additionally, a large deviation compared to the prediction of the SM has been observed in the muon g - 2 experiment [12] with a 4.2σ discrepancy at the time of writing this thesis. This intriguing result might be a hint for physics beyond the SM and further investigation is required to determine the source of this deviation.

While the so far mentioned g-factor measurement have been performed for the free electron and muon, the theoretical prediction is also possible for the g factor of an electron bound to a nucleus, which is therefore considered as bound-state QED (BS-QED). Compared to the free electron, the most important difference can be seen in the additional electric field due to the nucleus the electron is bound to. Specifically in the case of hydrogen-like ions, with only a single electron left, it is subject to the extremely strong electric field in close proximity (or even overlap) with this nucleus. This field can range up to $10^{16}\,\frac{\mathrm{V}}{\mathrm{cm}}$ in the case of $^{238}\mathrm{U}^{91+}$, which is close to the Schwinger limit [13], where the field strength becomes strong enough for the vacuum to break down and electron-positron pairs can be created.

However, despite such extreme conditions, for example in the measurements of the Lamb shift in $^{238}\mathrm{U}^{91+}$ [14], the hyperfine splitting in $^{208}\mathrm{Bi}^{80+}$ [15, 16] or the g factor of hydrogen-like $^{28}\mathrm{Si}^{13+}$ [17], no deviations between experiment and theory have been found, making the latter the most stringent test of BS-QED in strong fields.

To further advance such tests in the strongest fields, the ALPHATRAP experiment [18] has been built. As a Penning-trap setup, it is designed to perform measurements of the g factor of heavy highly charged ions (HCI) and, for this purpose, is connected to external ion sources. Combined with the ability to store and work with single ions for several months, the setup is well equipped to perform high-precision measurements.

While there have been several such measurements of an absolute g factor performed during this thesis, the main focus will rest upon the development and application of a novel measurement technique, based upon coupled ions in a magnetron crystal. This method has enabled the extraction of the isotopic difference of the g factors of the neon isotopes $^{20}\mathrm{Ne}^{9+}$ and $^{22}\mathrm{Ne}^{9+}$ with unprecedented precision in our field and overcome limitations such as inherent fluctuations of the magnetic field or the requirement of precise ion masses as external input parameters.

Content

I will begin this thesis with a brief introduction to g factors, different contributions and the basic knowledge required to understand the subsequent measurements and their motivation. Subsequently, Penning-trap physics will be discussed at a level required to make this thesis self-consistent. Here, important terminology used throughout this thesis will be introduced and potential sources of frequency shifts and the corresponding systematic uncertainties will be investigated.

I will then move on to describe the experimental setup to allow the reader to gauge the measurement possibilities of ALPHATRAP and to gain an idea of the layout of the experiment. In this part, I will also briefly describe the additions made to the setup during the course of this thesis.

Subsequently, the measurements and results of the individual g factors of $^{12}\mathrm{C}^{5+}$, $^{22}\mathrm{Ne}^{9+}$ and $^{20}\mathrm{Ne}^{9+}$ will be presented. These measurements have yielded important information about the performance of the trap and the scope of systematic uncertainties, improvements to atomic masses as well as parameters that will be important for the measurement with the coupled ions.

Thereafter, I will discuss the dynamics of coupled ions to derive the expected behaviour of such a system. This will be important to understand the principle of the main measurement to determine the g-factor difference as well as the systematic uncertainties of the obtained result.

Following this, the basic measurement procedure is explained, with a focus on the techniques that have been developed and applied to enable such a measurement. Finally, the data analysis and how the coherent signal of a Larmor frequency difference can be obtained will be explained. This will include the results and what their implications and applications are.

I will then conclude this thesis with a brief summary of all obtained results and provide an outlook on further possibilities of how the method can be improved and applied.

1 The *g* Factor . . .

In the following chapter I will discuss the basics concerning the g factor of the free and bound electron. This will be kept brief, but detailed enough to ensure a self consistent work and allow the reader to understand the measurements and impacts of the results performed in the context of this thesis. For a much more complete overview, see for example [19–21].

1.1 . . . of the Free Electron

The g factor of the free electron g_e is a proportionality constant to express the intrinsic magnetic moment $\boldsymbol{\mu_e}$ of an electron in units of the Bohr magneton μ_B as

$$\boldsymbol{\mu_e} = -g_e \mu_B \frac{\boldsymbol{S}}{\hbar} \tag{1.1}$$

with the spin $\boldsymbol{S}$ and the reduced Planck constant $\hbar = h/2\pi$. The Dirac equation [22], already including the spin property of an electron, predicts the value for a free electron to be exactly $g_e = 2$.

However, with increasing experimental precision and the discovery of the Lamb shift [5] in hydrogen, a deviation from that value was established over the following years [23]. The most precise measurement of this deviation to date, known as the electron $g-2$ measurement [7], has determined the *anomalous magnetic moment* a_e of a free electron to be

$$a_e = \frac{g-2}{2} = 0.001\,159\,652\,180\,73(28) \tag{1.2}$$

with a relative precision of 2.4×10^{-10} (or 2.8×10^{-13} relative to the absolute g factor). To theoretically derive this value, QED contributions have to be evaluated in several orders, foremost correcting for the effects of the charged electron on its environment due to its own field (self-energy) and the interaction with vacuum surrounding it (vacuum polarization). The first correction, the Schwinger term [24], achieves this by taking a virtual emission and absorption of a photon into account. Evaluating this to ever higher orders [8, 25] by taking more such emission and absorption vertices into account, the theory today is able to accurately predict this anomalous magnetic moment to comparable precision as the experimental values [26]. Combined with the precise experimental access this allows for stringent tests of the Standard Model, search for deviations as indication for physics beyond the Standard Model or for determining fundamental constants such as the fine-structure constant α [7].

1.2 …of the Bound Electron

While the absolute precision of the free-electron g-factor measurement cannot easily be challenged, an electron bound to a spinless nucleus offers access to an entirely different regime. The extremely strong field an electron experiences when bound to a highly charged ion (HCI), poses the potential to discover new effects that cannot be observed in weaker fields. When only a single electron is left bound to the nucleus, the ion is described as hydrogen-like and the electrostatic potential of the nucleus changes the wave function from a plane wave for the free electron to the hydrogenic wave functions instead. The solution of such a system, when assuming a point-like charge distribution, an infinite mass and therefore stationary nucleus, known as the *Furry picture* [27], can be written in terms of the nuclear charge Z and the fine-structure constant α as

$$g_{e,bound} = \frac{2}{3}\left[1 + 2\sqrt{1-(Z\alpha)^2}\right] \tag{1.3}$$

and was first derived by Breit, therefore often called the *Breit term* [28]. This term, derived from the relativistic solution of the Dirac equation for the 1s electron leads to the g factor of hydrogen-like ions becoming smaller for larger proton numbers Z.

1.2.1 Radiative Correction

Similar to the free electron, the radiative corrections as described by QED theory have to be included in the bound electron case as well. Here however, the coupling of the electron to the binding potential of the nucleus changes the Dirac equation and has to be included by a series expansion in terms of $(Z\alpha)$. There are two main approaches on how to treat this in the theoretical calculation.

In the regime of low Z, the calculation can be performed by keeping these effects as separate pertubative contributions to the general solution, treating each individually. Due to the scaling with $(Z\alpha)$, this approach is only feasible for small Z, where the series does converge quickly.

For higher Z, bound-state QED (BS-QED) deals with this problem by using the full solution of the Dirac equation in an idealized Coulomb potential instead. While this significantly reduces the amount of Feynman diagrams that have to be calculated, the quickly

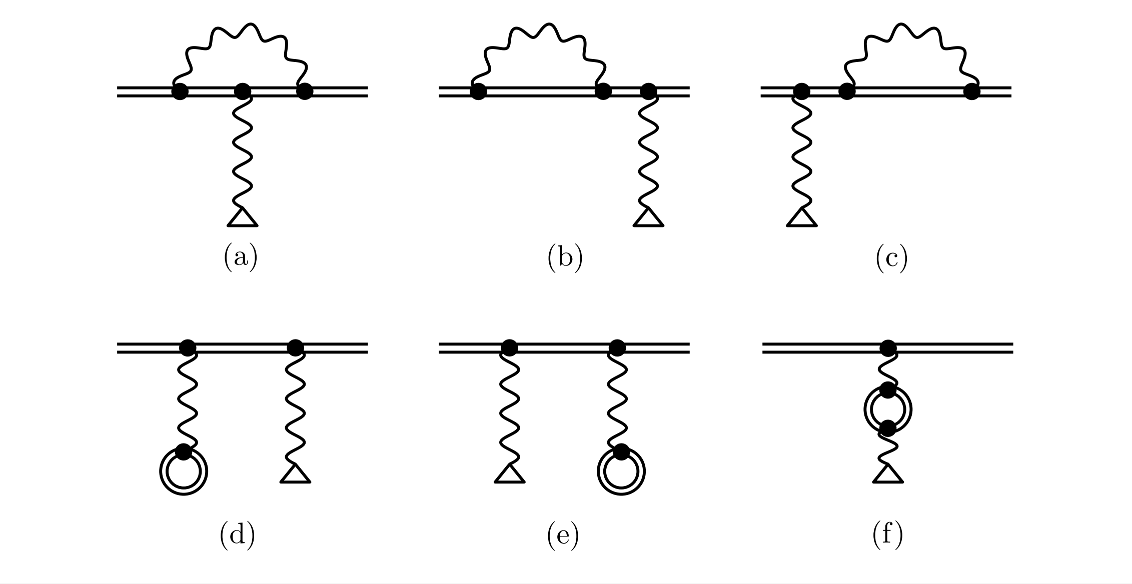

Figure 1.1: The six first order QED contributions to the bound-state g factor . The double line represents the combination of electron propagator in presence of the Coulomb field of the nucleus, with the pertubating field interaction indicated by the triangle. Graphs (a) to (c) show self-energy and (d) to (f) vacuum polarization contributions. Figure taken from [18].

growing complexity requires a numerical calculation of each diagram, making the process very time consuming. The estimation of the uncalculated contribution of higher order diagrams is the dominant uncertainty of the theoretical g-factor determination for high Z, hydrogen-like systems. In first order, or *one-loop* QED, there are six diagrams that have to be evaluated. These are shown in Fig. 1.1.

1.2.2 Nuclear Effects

The approximation of treating the nucleus as point-like and of infinite mass results in further corrections that need to be calculated when describing a real ion. The finite size, mass and internal structure of the nucleus lead to deviations from a static Coulomb potential, which can be categorized into different parts. Calculating these effects for the g factor is considered to be *beyond the Furry picture* and requires a fully relativistic treatment [29].

The **nuclear size** can be modelled via a charge radius in different ways, the most commonly used for QED calculations [30] is the root-mean-square (RMS) value of the radius, describing the nucleus as an uniformly charged sphere, that would produce the same charge distribution as experimentally observed if it had the identical charge and radius r_{RMS}. This leads to a correction of the energy level of the bound electron, changing the interaction with the field and giving rise to a relative g factor correction of about 2×10^{-9} in the case of hydrogen-like neon which scales as [30]

$$\Delta g, \mathrm{FNS} = \frac{8}{3}(\alpha Z)^4 \left(\frac{m_e c}{\hbar}\right)^2 r_{\mathrm{RMS}}^2 \tag{1.4}$$

for electronic s-states with the mass of the electron m_e and the speed of light c.
Nowadays, measurements of charge radii are utilizing optical spectroscopy to increasing precision [31], but are still limited in precision due to the requirement of the field shift factor, which is used to translate the measured transition frequency change to a change of radii. Due to this limitation, the charge radii of the neon isotopes – the main protagonists of this thesis – are still based on the evaluation of muonic spectroscopy [32] and the conversion to an r_{RMS} value [33]. This conversion is required for the corresponding QED calculations of electronic systems and can possibly give rise to problems, which will be discussed in more detail in the section regarding the experimental results and possible sources of error.
Another contribution arises from the finite mass of the nucleus and the resulting **nuclear recoil**, when the nucleus cannot be considered stationary anymore due to the interaction with the electron. The leading order, non-QED contribution due to this effect can be expressed as [29]

$$\Delta g^{1s} = \frac{m_e}{m_{nucleus}} \left[(\alpha Z)^2 - \frac{1}{12}(\alpha Z)^4 + ... \right]. \tag{1.5}$$

For $^{20}\mathrm{Ne}^{9+}$, this equates to a relative shift of 7.3×10^{-9} in first order, dominating the nuclear contributions by far. This contribution has been experimentally verified by measuring the isotopic shift of g factors in lithium-like calcium $^{40}\mathrm{Ca}^{17+}$ and $^{48}\mathrm{Ca}^{17+}$ ions [34].
Additionally, as the nucleus has only been treated as a source of a classical electromagnetic field, a QED treatment of the nucleus itself yields an additional correction. This treatment correctly accounts for the quantized momentum exchange between nucleus and bound electron, but does require a fully relativistic evaluation [29]. This QED contribution to the nuclear recoil, albeit small compared to the total nuclear recoil (about 2.4×10^{-10} relative shift for $^{20}\mathrm{Ne}^{9+}$), is interesting in itself as it has not been experimentally resolved so far since either theory [17] or additionally required parameters such as ion masses [34] were insufficient in precision. However, as it does already contribute on the level of the current theoretical precision, an experimental confirmation would be beneficial to allow further advancement of similar calculations for even heavier systems.
Depending on the examined ion species, additional nuclear effects may have to be considered. For the current considerations at ALPHATRAP , ions with a nuclear magnetic mo-

	^{20}Ne^{9+}	^{22}Ne^{9+}
Dirac value (point nucleus)	1.996 445 170 898(2)	1.996 445 170 898(2)
Finite nuclear size, FNS	0.000 000 004 762(7)	0.000 000 004 596(12)
QED, one loop (α)	0.002 325 473 294(1)	0.002 325 473 294(1)
QED, two loop $(\alpha)^2$	−0.000 003 547 780(117)	−0.000 003 547 780(117)
QED, ≥three loop $(\alpha)^{3+}$	0.000 000 029 524	0.000 000 029 524
Nuclear recoil		
Non-QED	0.000 000 146 093 420	0.000 000 132 810 693
QED	0.000 000 000 478 954	0.000 000 000 434 499
$(\alpha/\pi)(m/M)$	−0.000 000 000 113 2(6)	−0.000 000 000 102 9(5)
$(m/M)^2$	−0.000 000 000 044 1(2)	−0.000 000 000 036 5(2)
Hadronic effects	0.000 000 000 003	0.000 000 000 003
***g* factor total theory**	1.998 767 277 114(117)	1.998 767 263 640(117)
Difference (in 10^{-9})		
FNS	0.166(11)	
Recoil, non-QED	13.283	
Recoil, QED	0.043	
Recoil, $\alpha(m/M)$	−0.010	
Recoil, $(m/M)^2$	−0.0076	
Deformation	< 0.0001	
Polarization	< 0.002	
Δg **Total theory**	$13.474(11)_{\text{FNS}}$	
Δg **Experiment**	$13.47524(53)_{\text{stat}}(99)_{\text{sys}}$	

Table 1.1: Contributions to the calculation [36, 37] of the *g* factors of ^{20}Ne^{9+} and ^{22}Ne^{9+} and their differences.

ment other than zero are excluded from this discussion for now. This leaves the effects of the nuclear susceptibility, deformations of the nucleus and the nuclear polarizability [35]. Table 1.1 shows a full exemplary overview of all significant contributions to the theoretical calculation of the *g* factor of ^{20}Ne^{9+} and ^{22}Ne^{9+} and their differences [36]. For the individual *g* factors, the uncertainty stems almost exclusively from the uncalculated two-loop contributions (α^2) of orders $(Z\alpha)^6$ and higher. However, when looking at the difference, or the *isotopic shift* of the *g* factor, the uncertainty of this contribution becomes irrelevant since they are identical. The main contribution is then the relativistic part of the nuclear recoil, which has so far been tested to about 10 % [34]. The remaining uncertainty is now only dependant on the uncertainty of the charge radius difference of the isotopes. The QED contribution to the nuclear recoil has to date not been experimentally resolved, making this one of the goals of the work performed during this thesis. To perform a test of a contribution with a relative size of 5×10^{-12}, being visible with only four sigma compared to the uncertainty of the calculation due to the FNS, the experimental result needs to be of at least similar, preferably better precision to enable a stringent test. Since the relative precision of the masses of these ions is only 8.0×10^{-11} for $^{20}\mathrm{Ne}^{9+}$ and 8.6×10^{-10} for $^{22}\mathrm{Ne}^{9+}$ [38], a test of this contribution via an approach where the masses are required impossible. As this is the case for the determination of absolute g factors, as will be shown in the next chapter, a different method to determine such a difference has to be applied.

2 The Penning Trap

To determine the g factor to extreme precision, a Penning trap is used. In this chapter I will introduce how such a trap can be used to store and manipulate ions. Furthermore, I will establish terms and definitions that are to be used throughout this thesis. However, as many detailed descriptions of Penning-trap physics have already been given, for example in [39, 40] or more recently by both F. Köhler [41] and M. Höcker [42], these works should be considered as a much broader basis for general Penning traps instead. Here, I will first discuss the simplest case of an ideal trap with a single charged particle, then further expand the description to treat imperfections. For an in-depth description and derivation of This will also serve as a basis to derive and understand the coupled motion of two ions later on.

2.1 The Ideal Penning Trap

To radially confine a charged particle, a Penning trap uses a magnetic field of the form

$$\boldsymbol{B} = B_0 \boldsymbol{e}_z. \tag{2.1}$$

The the free-space cyclotron frequency ω_c is the angular frequency of the circular motion of a charged particle perpendicular to such a homogeneous magnetic field. It is given with the particle charge q and mass m as

$$\omega_c = \frac{q}{m} B_0. \tag{2.2}$$

The plane of this motion is defined as the radial direction. As the particle is not confined parallel to the magnetic field yet, an electric field along the magnetic field direction is superimposed. This prevents the escape of the particle along this *axial direction*, trapping it in all directions. Ideally, this electric potential is solely of quadratic order, thus achieving a harmonic oscillation. This can be well approximated by a cylindrical design, when adding additional *correction* electrodes, designed to null higher order contributions to

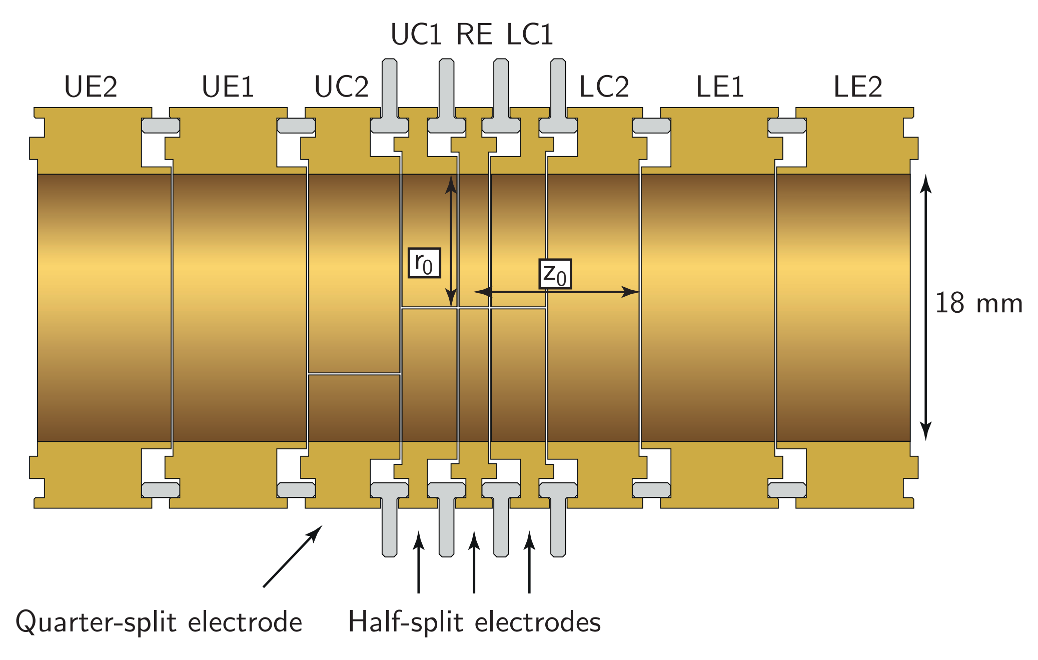

Figure 2.1: The precision trap (PT) of the ALPHATRAP setup, consisting of ring electrode (RE), two sets of upper and lower correction electrodes (UC & LC), and two sets of upper and lower endcaps (UE & LE). Figure adapted from [18].

the electric field. Such an ideal potential can then be written as

$$\Phi(z,\rho) = \frac{V_r}{2}\frac{C_2}{d_{\text{char}}^2}\left(z^2 - \frac{\rho^2}{2}\right) \tag{2.3}$$

with an applied ring electrode voltage V_r, an electrode geometry dependent C_2 parameter. Furthermore, the characteristic trap size is defined as $d_{\text{char}} = \sqrt{1/2(z_0^2 + r_0^2/2)}$, with the dimensions z_0 from the centre of the trap to the beginning of the first endcap electrode and r_0 as the radius of the electrodes as shown in Fig. 2.1.

While this field exerts a confining force in axial direction with a resulting axial frequency of

$$\omega_z = \sqrt{\frac{q}{m}\frac{V_r C_2}{d_{\text{char}}^2}} \tag{2.4}$$

it also introduces an outwards directed radial force. In combination with the Lorentz force of the magnetic field, this gives rise to the so-called $\boldsymbol{E}\times\boldsymbol{B}$ drift due to the repeated acceleration and deceleration of the ion. The full equation of motion can then be split and described by three individual harmonic oscillations, with the axial frequency ω_z as given above and the two radial frequencies

$$\omega_\pm = \frac{1}{2}\left(\omega_c \pm \sqrt{\omega_c^2 - 2\omega_z^2}\right). \tag{2.5}$$

Here, ω_+ is called modified cyclotron frequency and ω_- is the magnetron frequency. The stability criteria for a Penning trap can be derived from this equation as well, requiring $w_c^2 - 2\omega_z^2 > 0$, which is often referred to as a *weak* electric field in comparison to the magnetic field. Typical values for ions at ALPHATRAP are $\omega_+ \approx 2\pi \cdot 25\,\mathrm{MHz}$, $\omega_z \approx 2\pi \cdot 650\,\mathrm{kHz}$ and $\omega_- \approx 2\pi \cdot 8\,\mathrm{kHz}$. These frequencies are directly related to the free-space cyclotron frequency via the so called invariance theorem by Brown and Gabrielse [39]

$$\omega_c^2 = \omega_+^2 + \omega_z^2 + \omega_-^2. \tag{2.6}$$

Using this relation, the derived ω_c becomes invariant to possible imperfections, such as a trap tilt with respect to the magnetic field axis or an ellipticity of the electric potential [39]. The kinetic energy of each mode is given as [43]:

$$E_+ = \frac{1}{2}m(\omega_+^2 r_+^2 - \frac{1}{2}\omega_z^2 r_+^2) \approx \frac{1}{2}m\omega_+^2 r_+^2 \tag{2.7a}$$

$$E_- = \frac{1}{2}m(\omega_-^2 r_-^2 - \frac{1}{2}\omega_z^2 r_-^2) \approx -\frac{1}{4}m\omega_z^2 r_-^2 \tag{2.7b}$$

$$E_z = \frac{1}{2}m\omega_z^2 \hat{z}^2, \tag{2.7c}$$

where the negative sign of the magnetron mode should be noted. This is due to the applied electric field pushing the ion outward, resulting in a metastable motion, as the energy is larger for smaller magnetron radii. The same potential energy also applies to the cyclotron mode, but due to the much higher frequency the energy is mainly given by the kinetic term.

In addition to the motion of the ion in the Penning trap, one has to consider the effects on the electron bound to the nucleus. Specifically, upon placing the ion in a magnetic field, the spin-state $m_s = \pm\frac{1}{2}$ of the electron results in an energy splitting $\Delta E = \hbar\omega_L$ due to the Zeeman effect, with the Larmor frequency given as

$$\omega_L = \frac{g}{2}\frac{e}{m_e}B. \tag{2.8}$$

providing the relation to the g factor.

2.2 The Real Penning Trap

While the ideal-trap treatment is instructive for the definition of all frequencies, all possible contributions that induce shifts of those frequencies have to be considered. Here, the electric and magnetic inhomogeneities are first discussed separately. Combined effects, which are usually significantly smaller, will only be treated subsequently. While all these effects are derived for a single particle, most will directly correlate to the coupled ion measurement as well.

2.2.1 Electric Field Imperfections

The most natural way to achieve an electric quadrupole field is to use hyperbolic shaped electrodes, directly producing the required potential shape. This does however restrict axial access into the trap, making loading and transporting of ions as well as optical access into the trap, as already used in ALPHATRAP for optical spectroscopy [44], more challenging. An alternative is to use a cylindrical stack of of electrodes as shown in Fig. 2.1. The idea is to implement a specific geometry that achieves cancellation of higher order contributions to the electric potential caused by a single ring electrode by adding sets of correction electrodes. To this end, the measurement trap or *Precision Trap* (PT) of ALPHATRAP consists of a seven-electrode design with ring electrode, two sets of correction electrodes and two sets of end-cap electrodes[a]. The general potential (assuming rotational symmetry) in the centre can be written in terms of dimensionless coefficients C_n as [45]

$$\Phi(r,\theta) = \frac{V_r}{2}\sum_{n=0}^{\infty}\frac{C_n r^n}{d_{\text{char}}^n}P_n(\cos(\theta)) \tag{2.9}$$

with the Legendre polynomials P_n and the angle $\cos(\theta) = {}^{z}/_{r}$. To achieve the desired potential with only a C_2 contribution, the geometry of a seven-electrode trap (see Fig. 2.1) allows for tuning the even-ordered coefficients $C_4 = C_6 = C_8 = C_{10} = 0$ by design and corresponding applied voltages. However, due to machining or assembly imperfections, this will not hold true in the actual setup. Here, the two sets of correction electrodes will always allow to experimentally tune $C_4 = C_6 = 0$ by varying the applied voltages symmetrically. Due to the geometrical symmetry and symmetric voltages, this also allows us to neglect odd order coefficients, which are then typically small and also do not result in first-order frequency shifts [45]. Residual odd order coefficients can however still arise from patch potentials, when a charge accumulates on the surface of an electrode due to non-conductive contaminations or manufacturing imperfections. While these are

---

[a] The end-caps are split into two sets to simplify the transport of ions, but are treated as a combined electrode as they are typically all set to 0 V during measurements.

typically neglected, during this thesis asymmetric potentials have been used to axially shift the ion position out of the centre of the ring electrode, thus breaking the symmetry. The benefits of such a positional shift will be discussed much later, but, as it results in significant odd order contributions, the related frequency shifts have to be considered as well.

The tuning of even order coefficients is achieved by varying the voltage ratio of correction to ring electrodes, the so called *tuning ratio* (TR), while measuring the axial frequency dependence on different magnetron radii. Such measurements will be discussed in chapter 4.2.5 and are shown in Fig. 4.7. The first order frequency shifts from such electrostatic imperfections in a symmetric potential are given as [45]

$$\frac{\Delta\omega_z}{\omega_z} = \frac{3}{4}\frac{C_4}{C_2 d_{\text{char}}^2}(\hat{z}^2 - 2\rho_+^2 - 2\rho_-^2) \tag{2.10}$$

$$\frac{\Delta\omega_\pm}{\omega_\pm} = \mp\frac{3}{2}\frac{C_4}{C_2 d_{\text{char}}^2}(2\hat{z}^2 - \rho_\pm^2 - 2\rho_\mp^2). \tag{2.11}$$

The next orders have been derived similarly and can be found in [45] as well. An asymmetric potential in cylindrical coordinates can be written as

$$\Phi(z,r) = \frac{V_r}{2}\left[\frac{C_2}{d_{\text{char}}^2}\left(z^2 - \frac{r^2}{2}\right) + \frac{C_3}{d_{\text{char}}^3}\left(z^3 - \frac{r_\pm^2 z}{2}\right)\right] \tag{2.12}$$

using the above definitions. When no further forces along the axial direction[a] are present, a trapped ion moves about the equilibrium position where $C_1 = 0$. Therefore, care has to be taken to evaluate the electric potential around this position, rather than simply using the geometrical symmetric position in the centre of the ring electrode which will typically yield different results.

An analytical solution [46] of such a potential shows, that this can be described by a harmonic oscillator with a shifted equilibrium position Δz, compared to harmonic case [47]. The shift is dependent on the individual energies of the modes of the ion. For simplicity, here only the cases where either $\hat{z} \gg r_\pm$ or $r_\pm \gg \hat{z}$ are considered. In the case of large axial amplitudes (neglecting the $r_\pm^2$ term), this yields

$$\Delta z \approx -\frac{3}{4}\frac{C_3}{C_2 d_{\text{char}}}\hat{z}^2. \tag{2.13}$$

A series expansion around the new equilibrium position of the asymmetric potential

---

[a] These can stem from a B_1 or B_2, which will be discussed shortly

yields the corresponding frequency shift as

$$\frac{\Delta\omega_z}{\omega_z} \approx -\frac{15}{16}\frac{C_3^2}{C_2^2 d_{\text{char}}^2}\hat{z}^2. \tag{2.14}$$

In the case of large radial amplitudes (neglecting the $\hat{z}^3$ term), the positional shift evaluates to

$$\Delta z \approx \frac{3}{4}\frac{C_3}{C_2 d_{\text{char}}} r_{\pm}^2 \tag{2.15}$$

and performing a series expansion around the new motional equilibrium gives the relative frequency shift as

$$\frac{\Delta\omega_z}{\omega_z} \approx \frac{9}{8}\frac{C_3^2}{C_2^2 d_{\text{char}}^2} r_{\pm}^2. \tag{2.16}$$

One has to take note of the scaling of the axial frequency shift with $r_{\pm}^2$, which is the identical scaling as for the C_4 shift as in equation (2.10). When optimizing the axial frequency shift observed as a function of $r\pm^2$ one does therefore not achieve $C_4 = 0$ but will rather end up with $C_4 = {}^{3C_3^2}/_{4C_2}$ for the quadratic dependency. This can become a significant source of error when not using symmetric potentials, so that the C_3 term becomes large. Due to this, a full optimization of all frequency shifts depending on the different motional amplitudes can be necessary to fully tune – or at least limit – both, C_3 and C_4.

2.2.2 Magnetic Field Imperfections

When charging the magnet, the goal is to achieve a homogeneous field B_0 in the central area of the magnetic coil, where the measurement trap will be located. To achieve this, a superconducting magnet typically accommodates additional shimming coils beside the main coil that are used to correct for magnetic field inhomogeneities. When the magnet is first charged or needs to be tuned, an NMR probe can be used to characterize the magnetic field in the critical volume[a] of the magnet and the residual magnetic field inhomogeneities can be reduced. Here, the linear magnetic field gradient B_1 as well as the quadratic dependency B_2 are of most interest, as defined and discussed in more detail in [45]. For the ALPHATRAP PT these values are [18] $B_1 = 2.638(24)\,\frac{\text{mT}}{\text{m}}$ and $B_2 = 64.3(32)\,\frac{\text{mT}}{\text{m}^2}$. These values are measured with the complete setup in the magnet and different from the shimming, mostly due to the ferromagnetic ring electrode of the AT.

---

[a] At the very least for the PT

A linear gradient B_1 can be written in cylindrical coordinates as

$$\boldsymbol{B_1} = B_1 \left(z\boldsymbol{e}_z - \frac{r}{2}\boldsymbol{e}_r \right). \tag{2.17}$$

While odd order magnetic inhomogeneities do not produce frequency shifts in first order [45], they should be considered for their quadratic contribution in case they become large and, more importantly, in combination with effects causing an axial positional shift. An ion on a circular motion, here for the magnetron and cyclotron mode, can be described as a circular current $I_\pm = {}^{q\omega_\pm}/_{2\pi}$. This current produces a magnetic moment

$$\mu_\pm = -I_\pm \pi r_\pm^2. \tag{2.18}$$

This magnetic moment causes an additional force $F_z = \mu_\pm B_1$ in z-direction in a gradient field, thus shifting the equilibrium position depending on the radii of magnetron or cyclotron motion by

$$\Delta z \approx -\frac{B_1}{B_0}\frac{\omega_\pm \omega_c}{2\omega_z^2} r_\pm^2. \tag{2.19}$$

For the full calculation, see App. 8.3.1. The relative shift of the magnetic field now scales as ${}^{\Delta B}/_{B} = {}^{B_1}/_{B_0}\Delta z$, resulting in quadratic frequency dependence on B_1.
The next higher order, a quadratic contribution B_2 to the magnetic field, can be parametrized in similar fashion as

$$\boldsymbol{B_2} = B_2 \left[\left(z^2 - \frac{r^2}{2} \right) \boldsymbol{e_z} - zr\boldsymbol{e_r} \right]. \tag{2.20}$$

Contrary to the B_1 contribution, this contribution does produce first order frequency shifts on all modes, given as [41, 45, 48]

$$\frac{\Delta\omega_z}{\omega_z} = \frac{B_2}{4B_0}\frac{\omega_+ + \omega_-}{\omega_+\omega_-}(r_-^2\omega_- + r_+^2\omega_+) \tag{2.21a}$$

$$\frac{\Delta\omega_+}{\omega_+} = \frac{B_2}{2B_0}\frac{\omega_+ + \omega_-}{\omega_+ - \omega_-}\left(\hat{z}^2 - r_+^2 - r_-^2\left(1 + \frac{\omega_-}{\omega_+}\right)\right) \tag{2.21b}$$

$$\frac{\Delta\omega_-}{\omega_-} = -\frac{B_2}{2B_0}\frac{\omega_+ + \omega_-}{\omega_+ - \omega_-}\left(\hat{z}^2 - r_+^2\left(\frac{\omega_+}{\omega_-} + 1\right) - r_-^2\right) \tag{2.21c}$$

$$\frac{\Delta\omega_L}{\omega_L} = \frac{B_2}{2B_0}\frac{\omega_+ + \omega_-}{\omega_+ - \omega_-}\left(\hat{z}^2 - r_+^2 - r_-^2\left(1 + \frac{\omega_-}{\omega_+}\right)\right), \tag{2.21d}$$

where the identical scaling for ω_+ and ω_L should be noted. Thus, when measuring these frequencies simultaneously – or at the very least on the same radii – only the additional influence on the axial and magnetron modes have to be considered for the ratio of Larmor to cyclotron frequency. To measure this anharmonicity, one typically excites the modified cyclotron mode, r_+, to a known radius and measures the resulting shift of the axial frequency. However, one has to take care to exclude other effects that scale with $\propto r_+^2$ as well, to not accidentally cancel frequency shifts against each other. The shift of the axial frequency stems from the same effect as discussed for the positional shift due to B_1. The ions magnetic moment, depending on the radial energies, gives rise to an additional force in z-direction. Instead of a positional offset however, the quadratic B_2 contribution gives rise to an increased or decreased effective potential that directly affects the frequency scaling linearly with the B_2 contribution.

The resulting force from the total magnetic moment is given as $F_z = 2\mu_z B_2 z$. Adding this to the force from the electrostatic potential, the frequency shift can then also be written as

$$\frac{\Delta\omega_z}{\omega_z} = \frac{\mu_z B_2}{m\omega_z^2}. \tag{2.22}$$

2.3 Combined Effects

While most of the higher-order contributions stemming from the mixed effects are typically neglected, they will have to be considered in the context of this thesis. The effect of a shifted equilibrium position due to a C_3 and the resulting frequency shift depending on both, axial and radial energies has already been discussed. Similarly, B_1 does produce a shift of the position, but does not shift the axial frequency directly.

However, the same analysis as for the positional shift due to C_3 in a C_3 potential, leading to a quadratic dependency (Eq. (2.16)) has to be considered. Here, the shifted position due to B_1 in a C_3 potential will give rise to a shift depending on $B_1 \cdot C_3$. This is evaluated by using a series expansion of the potential in the position given by Eq. (2.19). For simplicity $r_\pm \gg \hat{z}$ is again assumed, neglecting the $\hat{z}^3$ contribution. The resulting frequency shift is given as

$$\frac{\Delta\omega_z}{\omega_z} = -\frac{3B_1 C_3 \omega_c \omega_\pm}{4B_0 C_2 d_{char} \omega_z^2} r_\pm^2. \tag{2.23}$$

The scaling with r_+^2 allows for an error when trying to determine the B_2 coefficient via cyclotron excitation and simply observing the axial frequency shift. Therefore, the uncertainty of C_3 will directly determine the uncertainty on B_2 as well, scaling with the size of B_1.

2.4 Measurement of Frequencies

To extract any information about the ion stored in the trap, the individual frequencies have to be measured. To non-destructively do so, one typically uses the image current induced by the moving ion. This current is typically in the range of some fA, depending

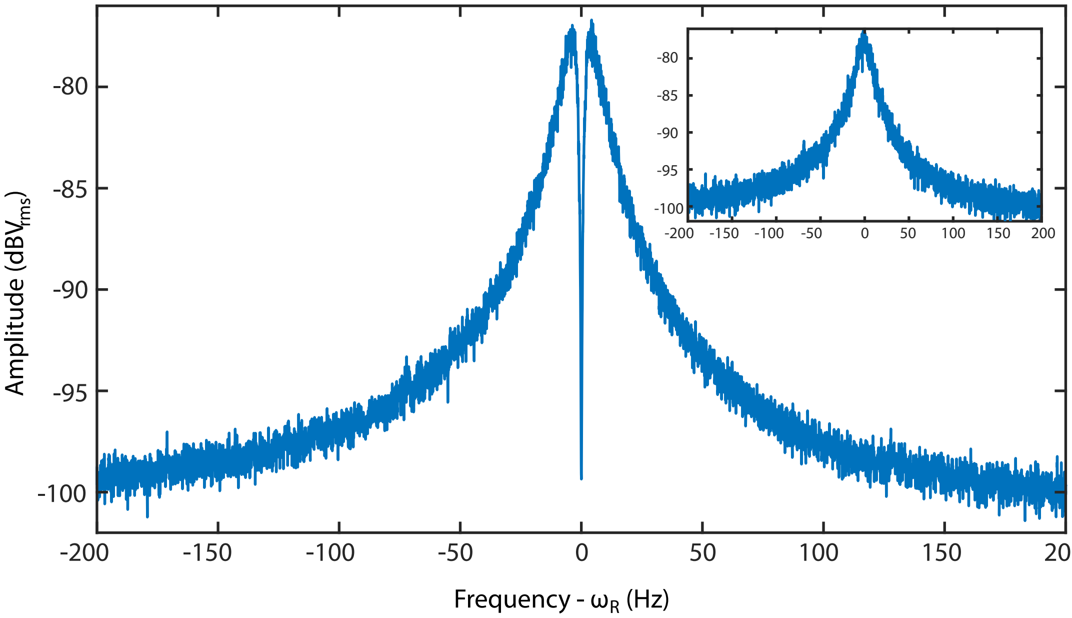

Figure 2.2: The axial signal of a single $^{20}\mathrm{Ne}^{9+}$ ion in the PT, fully thermalized with the tank circuit. The signal is mixed down to about 15 kHz to allow for the use of an FFT audio analyser to produce this spectrum. The small inset shows the same spectrum but without an ion in the trap, which consists only of the signal of the resonance circuit excited by thermal noise.

on the trap size, ion species and the electrode geometry used to detect it. To measure such a tiny current, a large impedance is required to produce a measurable voltage drop which can be achieved by a using resonant tank circuit that is matching the ion's frequency.

While axial and magnetron frequency can be tuned over a large range by simply changing the applied ring voltage, the axial frequency has to match the resonator frequency to allow for a detection of the ion, basically fixing both frequencies. The modified cyclotron frequency is fully determined by the chosen ion and the magnetic field which cannot be simply changed in our case. While some ideas allow to slightly tune the resonating circuits in frequency even after installation [49], different ions would still require different resonators for the cyclotron frequency, making the detection of the axial frequency the most practical as the voltage can be adjusted accordingly. Exactly at the resonance frequency ω_R of the tank circuit, the impedance consists only of the real part with an effective ohmic resistance $R_{\mathrm{eff}} = Q\omega_R L$, with the quality factor Q and the inductance L of the tank circuit. The alternating current now produces a voltage drop over the effective resistance, which can be amplified and finally measured by an external device [49].

This electric current through the resonator, induced by the ion, effectively results in the ions motion being damped by the effective resistance of the resonator until a thermal equilibrium between ion and resonating circuit is achieved. While the resonator is cooled by liquid helium to about 4.2 K, additional noise produced by the required amplifier and other electronics can increase the actual ion temperature. The definition and the measurement of the ion temperature will be discussed in chapter 4. Fig. 2.2 shows the measured voltage after performing a fast Fourier transformation (FFT) of the amplified[a] and down-mixed[b] signal. The inset figure shows the case without an ion in resonance, when only the thermal Johnson noise [51] is measured. If the ion is tuned into resonance, it produces the drop in amplitude, called dip, by shorting the noise at its motional frequency once it is fully thermalized with the tank circuit. In the case of $^{20}\mathrm{Ne}^{9+}$, this corresponds to an axial amplitude of $\hat{z} \approx 20\,\mu\mathrm{m}$. The lineshape of the noise density from the combination of ion and resonator can be calculated and fitted, allowing for a frequency determination with a precision of some 10 mHz [17], while directly compensating for shifts such as frequency pulling and pushing [52]. While there is a dedicated resonator for cyclotron measurements in the ALPHATRAP setup, the frequency has been tuned for $^{40}\mathrm{Ar}^{13+}$ and can only be used for very similar q/m ratios making it irrelevant for this thesis.

2.5 Measurement of the Radial Frequencies

Since the radial frequencies cannot be measured directly for all ions that will be discussed in this thesis, a different approach has to be taken. The radial modes can be coupled to the axial mode by applying a radio-frequency drive via dedicated split electrodes [53], which are indicated in Fig. 2.1. This process will generally be called *sideband coupling* throughout this thesis. Depending on how an electrode is split and on the position of that electrode, different electric-field contributions are achieved when a drive is applied. A dipolar excitation in the radial x direction D_x can be applied via the half-split ring electrode. Any offset of this electrode with respect to the geometric trap centre will additionally result in a contribution D_z in axial direction which can also used to excite the ion axially. These drives are applied at the frequency of the mode, resulting in the amplitude of that mode to linearly change[c] over the duration of the drive. The rate of this

---

[a] Details about the cryogenic detection electronics can be found in the thesis of Dr. A. Weigel [49].

[b] A single-sideband mixer [50] is used to shift the frequency of the amplified signal into a range that is covered by an audio analyser.

[c] If the drive is 90° shifted relative to the ion's phase (as there is an additional 90° phase lag), it will first decrease the amplitude to zero, then increase it again. Otherwise, it will result in a linear displacement in combination with the initial radius.

change depends linearly on the applied amplitude U_D. The general form of the applied electric field can be written as

$$E_D = -\frac{U_D}{d_{\mathrm{eff}}} \cos(\omega_{\mathrm{rf}} t + \phi_{\mathrm{rf}}) \tag{2.24}$$

with the parameter d_{eff} given by the geometry of the electrode that is used for the excitation. If the excitation is much larger than the initial amplitude of the ion, its phase is determined by the applied drive, lagging 90° behind the phase of the excitation ϕ_{rf}. Such an excitation can, when starting with a cold ion, be used to excite it to a known amplitude with a fixed phase, which will be used in phase sensitive measurements, as will be discussed in the next chapter. One should note that the interaction with the resonator will strongly affect the behaviour for excitations of the axial frequency. This is due to the coupling between ion and resonator, while the resonator itself is excited by a drive applied at a close-by frequency as well. Simultaneously, it is still cooled due to its coupling to the liquid helium (LHe) reservoir, which makes a calibration of the excitation amplitude complicated as one has to consider the different time-scales and coupling strengths of these interactions. For precision measurements, the radial excitations are more crucial and significantly less affected by this effect[a].

Similarly to this, another excitation that can be used is of quadrupolar geometry. Such an excitation can be achieved by applying the drive to an electrode that is both, split in half and offset from the geometrical trap centre, breaking radial and axial symmetry at the same time, optimized to achieve a Q_{xz} excitation. Contrary to the dipolar field, such a type of drive does depend on the position of the ion and can be written as

$$E_{Q_{\mathrm{xz}}} = -\frac{U_{\mathrm{xz}}}{d_{\mathrm{eff}}^2} \cos(\omega_{\mathrm{rf}} \cdot t + \phi_{\mathrm{RF}}) \begin{pmatrix} z \\ 0 \\ x \end{pmatrix}. \tag{2.25}$$

While the individual contributions can be used to excite the ion in axial or radial direction, depending on which frequency ω_{rf} is applied, the main purpose of this drive is the coupling of the normally independent modes. This is achieved by choosing ω_{rf} as any of the sidebands of $\omega_+ \pm \omega_z$ or $\omega_z \mp \omega_-$. Depending on the chosen sideband, this induces either a Rabi oscillation between the modes[b] or an exponential increase of both modes [18]. The former can be used to cool the radial modes, as energy is transferred with the

---

[a] For highest precision, one still has to be careful as an active drive might cause a heating of resonator, increasing the axial temperature. This can influence temperature measurements, determined from the thus thermalized modes.

[b] When the quantum mechanical model is studied, it can be shown that the coupling (or the Rabi oscillation) actually occurs for the quantum numbers n_z and $n_\pm$ of the modes [54].

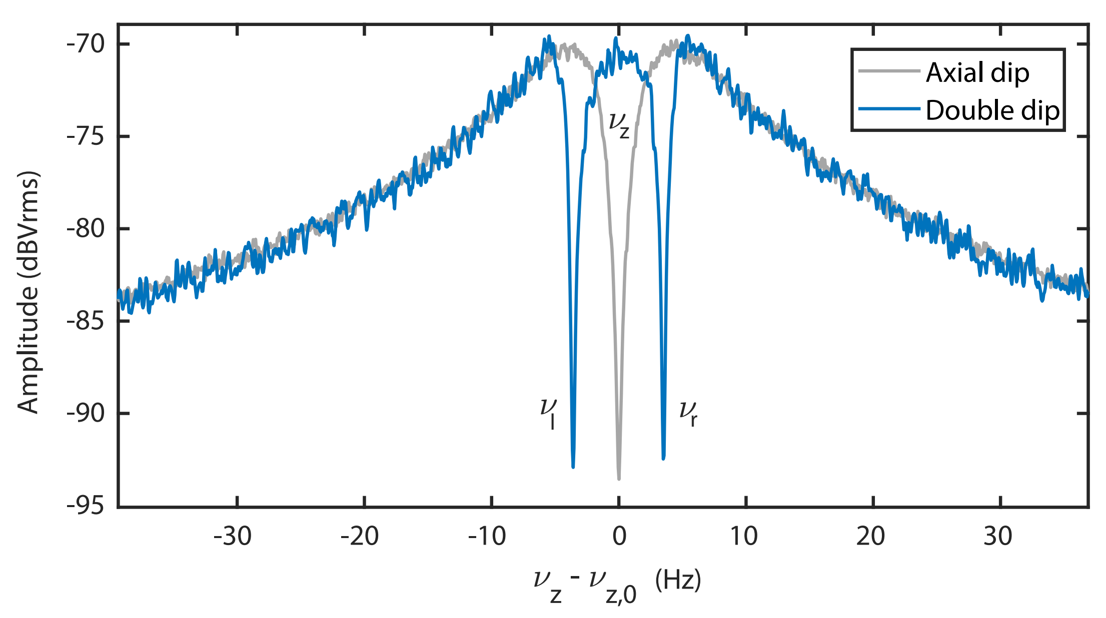

Figure 2.3: Spectrum of a modified cyclotron double-dip with $^{20}\mathrm{Ne}^{9+}$ (blue), the ion's spectrum without an applied drive (grey).

Rabi frequency to the axial mode, which is still coupled to the resonator and therefore permanently dampened.

The thus achieved coupling leads to a splitting of the single dip spectrum into a so-called double-dip as shown in Fig. 2.3, which can be used to infer the modified cyclotron frequency as

$$\omega_+ = \omega_l + \omega_r - \omega_z + \omega_{\mathrm{RF}}, \tag{2.26}$$

where ω_{RF} is the frequency of the applied drive, ω_l and ω_r are the left and right dips, and ω_z is the axial frequency. The determination of the axial frequency is crucial for measurements based on this method, as it directly enters the modified cyclotron frequency. When coupling the modes, the radial energy in thermal equilibrium is given by the expectation value of the axial energy and the frequency ratio:

$$< E_\pm >= \frac{\omega_\pm}{\omega_z} < E_z > . \tag{2.27}$$

The sideband causing an exponential increase of both modes is used for example during phase sensitive measurements, where it allows to transfer the phase information of radial to axial mode where it can then be measured via an axial detection.

2.5.1 Phase Sensitive Measurements

While the dip detection, combined with sideband coupling, allows for the measurement of all motional frequencies, it is limited in resolution by the long sampling time required to resolve the dip spectrum in the recorded thermal noise spectrum as well as the required knowledge of the exact line shape used fitting the measured signal. With the modified cyclotron frequency being the most critical to measure as it contributes most to the determination of the cyclotron frequency ω_c, it is beneficial to keep the measurement time as short as possible to minimize all effects due to drifts and jitter.

To this end, the measurement technique of pulse and amplify (PnA) introduced in [55] has been applied for the determination of the g factors of the neon isotopes. Here, the ion is excited in the modified cyclotron mode to a radius significantly exceeding the typical thermal radius $r_p \approx 2\,\mu\mathrm{m}$, here typically chosen to be 16 to 19 µm, where the trade-off between resolution and introduced systematic shifts is most reasonable. By exciting this mode, a fixed phase is imprinted on the motion, which then is allowed to evolve freely for a fixed time. At the end of the evolution period, the current phase is transferred into the axial motion by applying a quadrupolar (sideband) pulse.

The recorded axial phase will then depend on the phase of the modified cyclotron frequency at the time of this pulse. With a typical phase resolution, including all sources of phase jitter stemming from the initial thermal distribution of the ion amplitude as well as all additional jitter introduced by measurement devices, a phase stability of about 20° is achieved for an evolution time of about 8 s. This corresponds to a relative frequency resolution of

$$\frac{\Delta\omega_+}{\omega_+} = \frac{20^\circ}{360^\circ}\frac{1}{8\,\mathrm{s}\cdot 25\times 10^{6}\,\mathrm{Hz}} \approx 3\times 10^{-10} \tag{2.28}$$

for a single[a] measurement. While this method has been developed and used in the Mainz HCI g factor experiment (Liontrap now) for several years already, it was only incorporated into the measurement routines of Alphatrap during the course of this thesis.

2.6 Measurement of the Larmor Frequency

The spin magnetic moment of the electron, projected on the z-axis can be written in terms of the g factor and the Bohr-magneton $\mu_B = {e\hbar}/{2m_e}$ as

$$\mu_z = \mp\frac{1}{2}g\mu_B. \tag{2.29}$$

---

[a] This is a very simplified description; in reality this measurement does require an input frequency, which is determined via a double-dip as well as multiple shorter evolution time measurements to correctly unwrap the total phase. The measurement of the frequency is done over a much shorter time interval, however, reducing drifts and fluctuation effects compared to the double-dip.

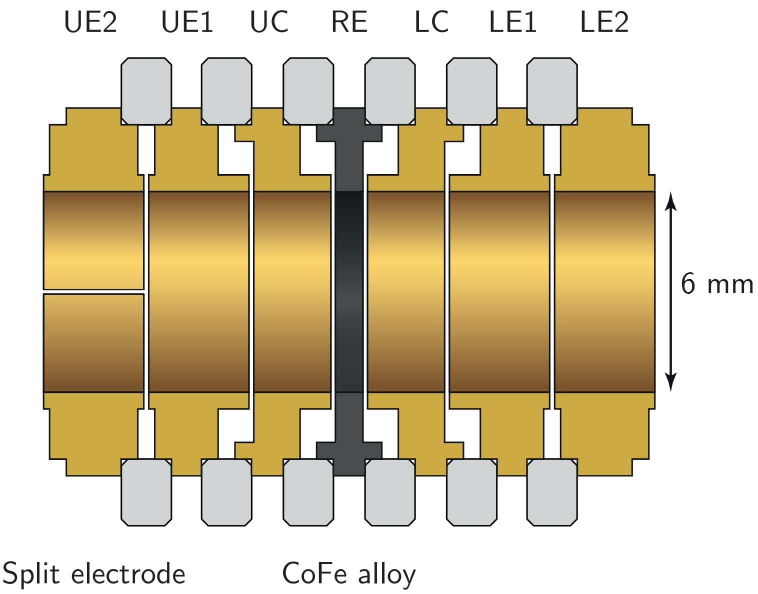

Figure 2.4: The analysis trap, with the much smaller diameter of 6 mm compared to the PT (18 mm) and a ferro-magnetic ring electrode to produce a strong B_2. Figure taken from [18].

Similar to the ion's magnetic moment, as discussed in section (2.2.2), the axial frequency is dependent on the magnetic moment of the electron spin. This frequency shift can be expressed as

$$\Delta\omega_z^{SF} = \pm \frac{g\mu_B B_2}{2m_{ion}\omega_z}. \tag{2.30}$$

The orientation of the spin (or spin state) and therefore the spin magnetic moment can be reversed, if a photon of frequency ω_L is absorbed or emitted[a]. To this end, the required microwave frequency can be irradiated into the trap to achieve such a reversal, typically referred to as *spinflip*. However, the PT has already been discussed with the requirement of a very homogeneous magnetic field, where the resulting axial frequency change would not be detectable. The approach to solve this is the double-trap technique, which utilizes a second Penning trap, the analysis trap (AT), where the B_2 is large. In our case, this is achieved by using a ferro-magnetic CoFe (Vacoflux50) ring electrode as shown in Fig. 2.4 to achieve a $B_2 \approx 44\,\frac{\mathrm{kT}}{\mathrm{m}^2}$ [18]. With these values, Eq. (2.30) predicts a frequency change of $\Delta\nu_z^{SF} \approx 1.8\,\mathrm{Hz}$ or $\Delta\nu_z^{SF} \approx 1.6\,\mathrm{Hz}$ in the cases of $^{20}\mathrm{Ne}^{9+}$ and $^{22}\mathrm{Ne}^{9+}$ respectively, which can easily be resolved. A sequence of microwave irradiations and the observed change in axial frequency of $^{22}\mathrm{Ne}^{9+}$ is shown in Fig. 2.5.

One has to note, that not only changes of the magnetic moment due to the spin orientation, but also due to changes of the amplitudes of the radial modes of the ion will

---

[a] By stimulated emission, spontaneous emission is highly improbable for these states.

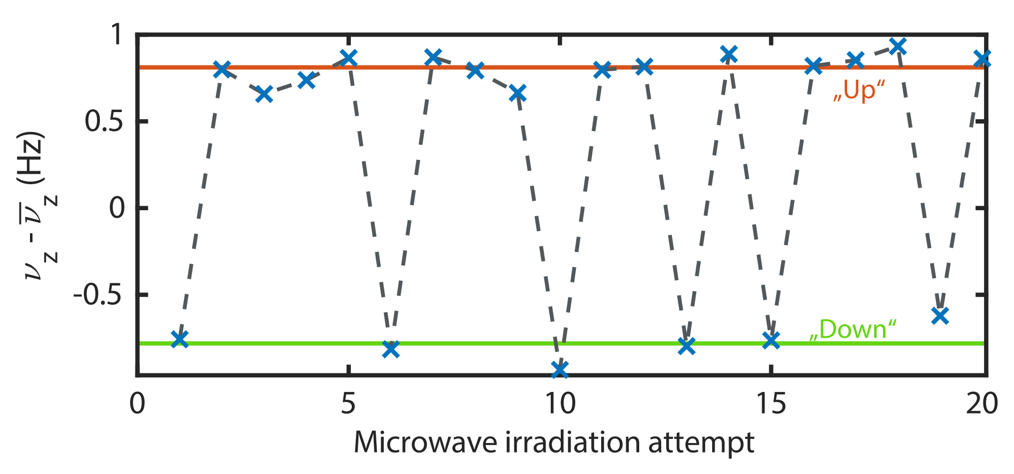

Figure 2.5: Axial frequency change due to spinflips in the analysis trap. At each point, the microwave is irradiated for a few seconds and the axial frequency is compared with the one measured before.

now affect the axial frequency. The observed axial frequency shift of the ion between subsequent measurement cycles is mostly caused by the varying cyclotron radius. This frequency shift is generally much larger compared to that of a spinflip. However, the cyclotron radius is typically stable enough[a] during the time in the AT to allow for a detection of the instantaneous frequency change in case of a spinflip.

Especially for heavier ions where the frequency change due to a spinflip becomes smaller, the axial frequency stability can pose serious problems for the determination of the spin state. For all purposes discussed here, this is however not of concern.

While the Larmor frequency can be measured in the AT by determining the most likely irradiated microwave frequency to achieve a spin transition, the large B_2 does not allow for precise measurements. Therefore, rather than measuring the Larmor frequency in the AT, the idea is to prepare the ion with a known spin state by observing a transition in the AT first, the subsequently transporting it to the PT. Here, one can measure the cyclotron frequency while simultaneously irradiating the microwave frequency again. Finally, the ion is brought back to the AT and the spin orientation is compared to the initial one, which then allows to infer if a spin transition has been achieved during the irradiation in the PT.

The probability of a spinflip occurring in the PT is maximized, when the irradiated microwave matches the Larmor frequency. Since the Larmor frequency is dependent on the magnetic field, this is typically expressed instead in terms of the frequency ratio $\Gamma = \frac{\omega_L}{\omega_c}$. The g factor can then be expressed in terms of the ratio, where the maximum probability

---

[a] Heating effects can cause a random fluctuation of the mode.

of a spin transition to occur has been observed as

$$g = 2\Gamma \frac{q_{\mathrm{ion}}}{e} \frac{m_e}{m_{\mathrm{ion}}}, \tag{2.31}$$

For such a determination, the knowledge of the precise ratio of ion mass m_{ion} to electrons mass m_e is additionally required from independent measurements. The process of actually extracting the g factor will be described in the sections corresponding to the individual measurements (4).

2.7 Measurement of Amplitudes and Temperatures

The knowledge of the ion temperature as well as the radii after an excitation are important parameters to correct for systematic shifts or simply calibrate excitations to achieve a certain amplitude deterministically. To determine the amplitude of the ion after an excitation, the easiest way is to make the axial frequency dependent on that radius. This can be achieved by applying an anharmonic electric field contribution, typically a C_4. According to formula (2.10), if the C_4 is known, there is a direct relation between amplitude and the observed axial frequency. The additional C_4 contribution for a certain deviation from the ideal potential is extracted from an electrostatic Comsol model of the trap.
Another approach is to use the magnetic B_2 frequency shift of the axial mode, which is dependent on the magnetic moment of the ion and therefore mainly on the cyclotron radius. To utilize this for a temperature measurement, the axial mode can be coupled to the cyclotron mode in the PT until the modes are thermalized. After transporting the ion back to the AT, the observed axial frequency each cycle despite identical voltages then allows to determine the cyclotron radius and thus its energy. Recording the distribution of such shifts, the temperature of cyclotron and axial temperature can be extracted. Such a measurement is shown later in section 4.2.5.

3 Experimental Setup

In this chapter I will describe the experimental setup. This will include information to gauge the possibilities of the ALPHATRAP experiment and understand how the external infrastructure is operated to produce, transport and load ions. There will also be explanations of modifications made to the setup during the course of this thesis, including the connection to two new ion sources. Furthermore, the specifics that differ in the setup during this work from the much more extensive description that can be found in our Review paper [18], which comprises parts of this thesis, will be covered.

3.1 The Trap(s)

The heart of the setup is, as suggested by the name ALPHATRAP , the Penning trap. The trap actually consists of a stack of three separate trap sections. The analysis trap (AT) has already been briefly discussed in section 2.6 and is mostly distinguished by a $B_2 \approx 44\,\frac{\mathrm{kT}}{\mathrm{m}^2}$, produced by the ferromagnetic ring electrode. The purpose of the AT is mainly the electronic spin-state detection (see 2.6), it can however also be used to measure temperatures (see 4.2.5) or to separate coupled ions (see 6.2.6). However, while essential for the measurements performed at ALPHATRAP, the huge B_2 makes it impossible to achieve the high precision frequency measurements that are aimed for.

For the purpose of such measurements the other main trap, the precision trap (PT) as introduced in section 2, is utilized. The extremely homogeneous magnetic field here allows for such precise frequency measurements. With a seven-electrode design, both the C_4 and the C_6 contribution to the electric potential can effectively be tuned to zero, while the geometry is designed such, that even C_8 and C_{10} are supposed to be very small [56]. Therefore, the PT is optimized to be used for all spectroscopic measurements.

The third part is the capture trap (CT), which is mostly distinguished by the first three electrodes where the applied voltage can be changed rapidly. While all other trap electrodes are filtered to allow only slow voltage changes on the order of some ms, the three topmost electrodes can be pulsed to a different voltage quickly ($\approx 1\,\mu\mathrm{s}$) by several 100 V to facilitate the capture of injected ions. This capture process and the layout of the trap is shown in Fig. 3.1.

The black cone shown on the left in Fig. 3.1 is made of PEEK, infused with carbon nanotubes [57], meant to absorb the microwaves irradiated from the other end of the trap. Thus, reflections should be prevented which might otherwise cause a standing wave in the trap cavity.

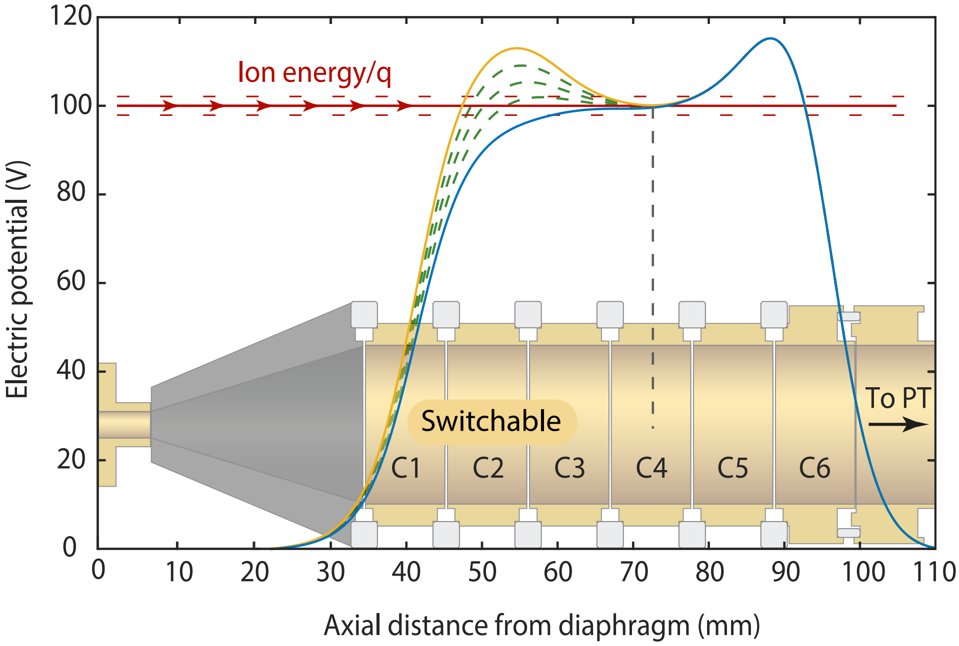

Figure 3.1: The CT and the capture process of injected ions. Electrodes C1 to C3 can be quickly pulsed to a different voltage to trap incoming ions. For such a trapping, the potential is altered starting from the blue curve, which is still allowing the ions to surpass the initial potential while slowing them down. Once they have passed, the potential is pulsed to a higher voltage (indicated by the green dashed lines) and achieves the shape as represented by the yellow curve, resulting in the ions to be trapped in the C4 electrode. Figure adapted from [18].

After injection, the CT can be used as a storage trap, keeping a cloud of ions ready to extract single ones for the measurement without having to reload from external sources every time an ion is lost. This happens mostly due to the erroneous handling of the ions or device crashes, as losses due to recombinations with residual gas typically only occur after months of storage time, depending on the charge state of the ions. The complete trap tower is shown in the inset of Fig. 3.2.

3.2 The Cryostat

The trap stack and all electronics are situated in a 4 T super-conducting magnet with a warm bore. However, as the trap is meant to be operated at cryogenic temperatures, a dedicated cryostat is required for cooling it and the detection electronics to liquid helium temperature of around 4 K. The design of this cryostat, as inserted into the magnet, is shown in Fig. 3.2. It consists of an outer 70 K shield at liquid nitrogen temperature (blue), and an inner 4 K section (pink), which is thermally coupled to the LHe vessel. The cryogenic valve (white) [49] allows for a connection to a room temperature ultra-high vacuum (UHV) beamline without impairing the cryogenic vacuum quality when it is closed. This design allows the flexibility of being able to externally produce and inject the desired ions while still achieving storage times of several months for the captured ions. The trap and the detection electronics are shown in the central area of the magnet [18, 49].

The complete 4 K section, with trap and electronics, can be lifted out of the cryostat separately to access and modify these parts without having to remove the complete cryostat from the magnet. Additionally, the warm bore of the magnet also facilitates access to the trap from below. This is used for both, optical [44, 58] and microwave access as shown in the Fig. 3.2.

3.3 The Beamline and Ion Sources

The main part of the UHV room temperature beamline of the ALPHATRAP experiment is situated at the floor above the magnet room. Here, three different ion sources are connected to allow for the production of different ions.

The most commonly used source thus far has been a Heidelberg compact electron beam ion trap (HC-EBIT) [60], where ionization energies of around 4 keV have been reached. This source operates by emitting and accelerating electrons to ionize gas upon impact in the centre of a magnet field, produced by permanent magnets. Additional electrodes (called drift-tubes) allow for control and ejection of the thus produced ions by pulsing the applied voltages. The application of this source is highly versatile, as it can be used for any species that can be injected in a gaseous phase via a needle valve. This allows for switching to different ion species within only a few hours.

The second ion source, a laser ion source [61], has been connected and used to inject $^{9}\mathrm{Be}^{+}$ ions during the course of this thesis. First laser cooling tests of these ions have been successfully conducted [44] and will be used for sympathetic laser cooling in the ALPHATRAP setup in the future. The ion source operates by using an external Nd:YAG

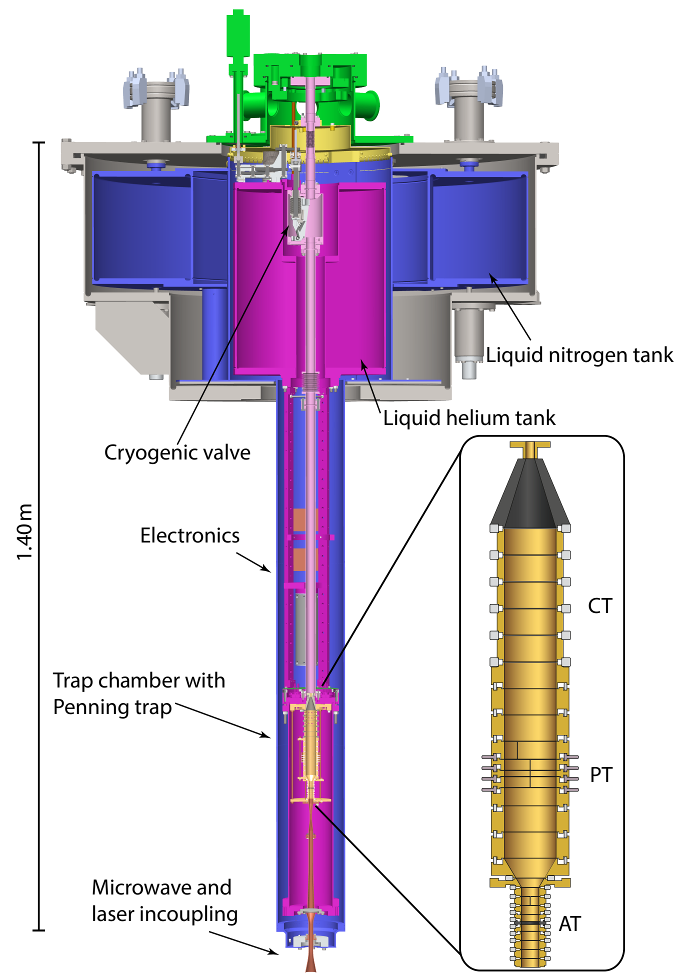

Figure 3.2: The ALPHATRAP cryostat setup, consisting of a 70 K section (blue), a 4 K section (pink), the trap stack (inset), the electronics and resonators in the centre and a cryogenic valve (grey). The inner 4 K section can be removed independently, together with the hat flange (green) that supports the complete section with low-thermal conducting Vespel® [59] rods. Figure adapted from [18].

laser [62], which ablates material and ignites a plasma when a laser pulse is shot onto a target. In combination with an applied voltage, ions can be extracted and guided towards the trap. However, without additional means of ionization, mostly singly charged ions are produced here.

The third ion source is the Heidelberg EBIT (HD-EBIT), a functionally much larger scale version[a] of the HC-EBIT. While the working principle is identical, this EBIT instead uses a superconducting magnet and can currently be used with ionization energies of up to 50 keV. The connection to this EBIT has been established via a 5 m beamline section as part of this thesis. This connection has already been used to load ions, first $^{40}\mathrm{Ca}^{17+}$

---

[a] It is placed in a separate large container building of about 7 m × 8 m, required due to the high-voltage operation.

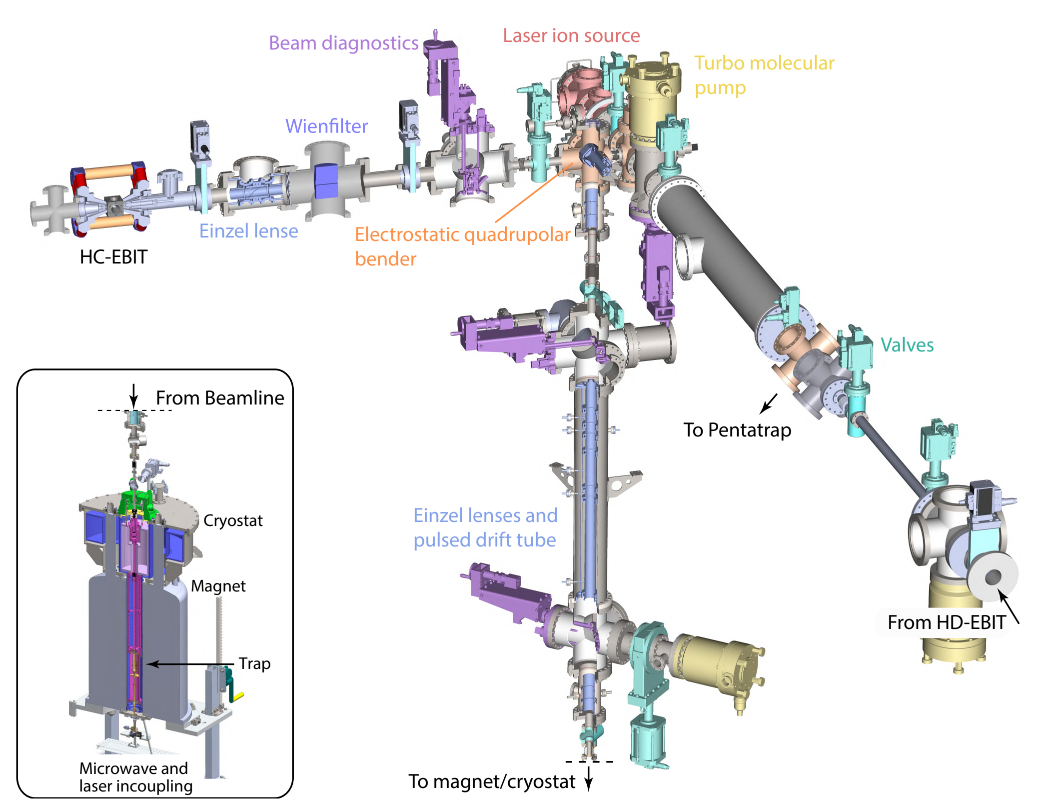

Figure 3.3: The ALPHATRAP beamline with connections to three separate ion sources (see text). The beamline facilitates several ion optical elements as well as units for beam diagnostics. The ions are transported with energies of some $\frac{\mathrm{keV}\, q_{\mathrm{ion}}}{\mathrm{C}}$ towards the trap. When they are close to the magnet, they are first slowed down by a pulsed drift tube in the vertical section before entering the cryostat region. They are then captured in the CT section of the trap stack.

and later on also $^{118}\mathrm{Sn}^{49+}$, where the g factor has been measured as part of the thesis of J. Morgner (ongoing). The new part of the beamline consists of a straight connection, with ion diagnostic units on both ends. The largest tube also includes two sets of Einzel lenses, one at either end of the tube. In between, two sets of steering plates allow for a deflection of the beam before entering the first of the two electrostatic benders at the main beamline. Here, the ions are first steered 90° to the left, then again 90° down towards the setup as seen from the direction of the ions.

This new beamline also features the possibility of a future connection to our neighbouring experiment PENTATRAP [63], enabling them to access ions produced by the HD-EBIT. To this end, a currently empty cross, meant to house an electrostatic quadrupolar bender, is already included in the design. To facilitate craning of the PENTATRAP setup through a hole in the floor underneath this connection, the tube above their experiment is designed to be easily removable. An overview of the complete ALPHATRAP beamline is shown in Fig. 3.3.

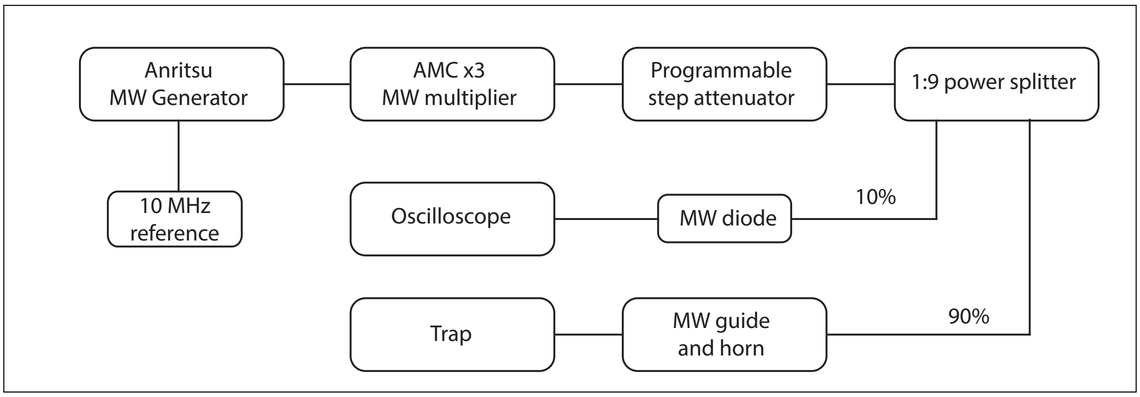

Figure 3.4: The schematic microwave setup. For details see text.

3.4 Microwave Setup

The microwave setup used during the course of this thesis consists of several devices and safeguards to ensure a stable operation. Especially in case of the coupled ions measurement, both pulse times and microwave power have to remain consistent over the course of the measurement campaign of several weeks. To monitor this during the measurement, a 10:90 power splitter and microwave diode [64] is used to monitor the irradiated microwave pulse shape and amplitude for every run. The schematic setup is shown in figure 3.4. The Anritsu [65] produces a microwave at a frequency of $1/3\omega_L$, as it is connected to an active multiplier chain (AMC) [66] with a frequency multiplication of 3. The nominal output power of this amplifier is 20 dBm when the input is saturated. Next in line is a motorized and calibrated microwave attenuator [67] which can be used to reduce the power in a controlled way. The 10 MHz unit is connected to all measurement devices, including the microwave generator, FFT analyzer and all function generators. This ensures a stable operation and provides a reference to enable the measurement of absolute frequencies.

4 Measurements and Results: Single Ion Measurements

In this chapter, I will discuss the results of all the single ion g-factor measurements. These consist of a total of almost 20 individual resonances of three different hydrogen-like ion species, which will be presented in the chronological order they were measured in. This begins with a systematic test performed with a carbon ion, followed by the g-factor measurements of the neon isotopes $^{20}\mathrm{Ne}^{9+}$ and $^{22}\mathrm{Ne}^{9+}$, through which it is possible to improve the precision of the atomic mass of the latter by almost an order of magnitude when using the theoretical calculation of the g factor as an input.

During the campaign on $^{20}\mathrm{Ne}^{9+}$, a tension of a combined 3σ between experimental and theory values of the g factor have been observed and were had been attributed to the atomic mass of $^{20}\mathrm{Ne}$. While this could initially not be resolved, further investigation is being conducted as of finishing this thesis. Preliminary results of the measurement performed by the PENTATRAP group strongly indicate that the deviation of the atomic will soon be confirmed, leading to an agreement between experiment and theory for the g factor .

This section will also include systematic studies related to the two-ion method, as the characterization of the trap was performed during this campaign, preparing everything for the measurement on the coupled ions. Note, that all specified shifts (or systematic effects) are given as relative shifts with respect to the frequency ratio $\Gamma_0 = \frac{\omega_L}{\omega_c}$ as

$$\Delta_{\mathrm{rel}} = \frac{\Gamma' - \Gamma_0}{\Gamma_0}, \tag{4.1}$$

where Γ_0 is the true value and Γ' the measured (uncorrected) value, shifted by the given amount. Therefore, the correction that has to be applied is of opposite sign as the given shifts.

4.1 Carbon *g* Factor

The measurement of the g factor of $^{12}C^{5+}$ is the first that has been performed during the course of this thesis, after I became responsible for the control of the trap. At this stage, the measurement campaigns of Dr. I. Arapoglou, with the g factor of $^{40}Ar^{13+}$ [56], as well as the laser-spectroscopic measurement of the fine-structure of the same ion by Dr. A. Egl [58], had both been finished. However, as ALPHATRAP was still quite new, the choice for the initial measurement fell on the g factor of $^{12}C^{5+}$ as an accuracy check. This ion had been used to extract the most precise value for the electron mass in the predecessor experiment of ALPHATRAP in Mainz [68, 69] and remeasuring it therefore provides both, a decent starting point to learn to operate the trap as well as information about the performance of our setup and possible unknown systematic effects.

4.1.1 Measurement Procedure

The measurement begins with the cold ion in the AT. Here, the microwave is irradiated, until a spinflip is observed, thus allowing to determine the spin state the ion is in now. Subsequently, the ion is transported to the PT, where one waits for a short time to allow the voltages to settle after the transport.

After cooling both radial modes by shortly coupling them to the axial mode, the first axial dip is recorded. Afterwards, the microwave is irradiated at a pre-determined value close to the expected Larmor frequency. Simultaneously, a cyclotron double-dip is recorded, which will serve to determine the magnetic field during this irradiation. Finally, a second axial dip is recorded to determine, if the frequency has drifted during the measurement of the modified cyclotron frequency. After again cooling both radial modes, the ion is transported back to the AT, where the spin state is again determined.

The resulting 10 resonances recorded during this measurement campaign are summarized in Tab. 4.1, including their systematic uncertainties. Those only applicable to this specific carbon measurement are explained in the following, the general systematic effects that have to be considered for any g-factor measurement are discussed at the end of this chapter.

4.1.2 Axial Frequency Drift

The measurement has been performed using the double-dip technique (see section 2.5) for the determination of the modified cyclotron frequency as PnA had not been implemented into the setup yet. This means that after preparing the spin state in the AT, the ion is transported to the PT, where, after a waiting time to allow voltages to settle, the ax-

Combined (uncorrected) Γ'	$4376.210\,499\,27(116)$
shifts and error budget	
ICS	$1.5(1) \times 10^{-11}$
rel. shift	$3(1) \times 10^{-12}$
ν_z drift	$0(2) \times 10^{-10}$
Lineshape dip	$0(1) \times 10^{-10}$
C_4 shift	$< 0(6) \times 10^{-13}$
$\geq C_{n\geq 6}$	$< 0(3) \times 10^{-16}$
T_z	$7.1(4)\,\mathrm{K}$
corrected Γ_0	$4376.210\,499\,19(116)_{\mathrm{stat}}(94)_{\mathrm{sys}}$
stat. uncert.	2.7×10^{-10}
sys. uncert.	2.1×10^{-10}
$\Gamma_{e_{\mathrm{mass}}}$	$4376.210\,500\,872(102)_{\mathrm{stat}}(69)_{\mathrm{sys}}$ [69]
combined deviation	1.4σ
Electron mass	
$m_{e,\mathrm{exp}}$	$\mathbf{5.485\,799\,093\,3(15)_{\mathrm{stat}}(12)_{\mathrm{sys}} \times 10^{-4}}\,\mathrm{u}$
$m_{e,\mathrm{CODATA}}$	$5.485\,799\,090\,65(16) \times 10^{-4}\,\mathrm{u}$
Input parameters	
g factor	$2.001\,041\,590\,179\,8(47)$ [69]
Mass of $^{12}\mathrm{C}^{5+}$	$11.997\,257\,680\,291\,7(18)\,\mathrm{u}$ [69]

Table 4.1: The combined analysis for the determination of the electron mass at Alphatrap by means of measuring the $^{12}\mathrm{C}^{5+}$ g factor .

ial frequency is measured first. Directly after, a double-dip is sampled for roughly 3 min, during which the microwave is continuously irradiated. Finally, a second axial dip is recorded to check for potential drifts. Since this drift was one of the former limitations [56, 70], care has been taken to further minimize the effect. This is mainly achieved by simply waiting longer for the voltage to settle after the ion transport, combined with an increased sampling time for the individual dips.

To verify the systematic effect of the axial frequency drift, the sequence has been modified to sample three individual axial dips in the same period during which in the actual measurement the first axial frequency, then a double-dip and finally another axial frequency have been recorded. The result of this study is shown in Fig. 4.1. The complete drift between first and second axial dip of the measurement could already be significantly reduced to 44 mHz and 29 mHz for two different settings respectively, compared to previously almost 100 mHz [70]. However, this measurement shows, that a correction of 9(4) mHz and 7(5) mHz of the axial frequency is still required, where the uncertainty is the standard deviation of the mean observed drift. This corresponds to a 2×10^{-10}

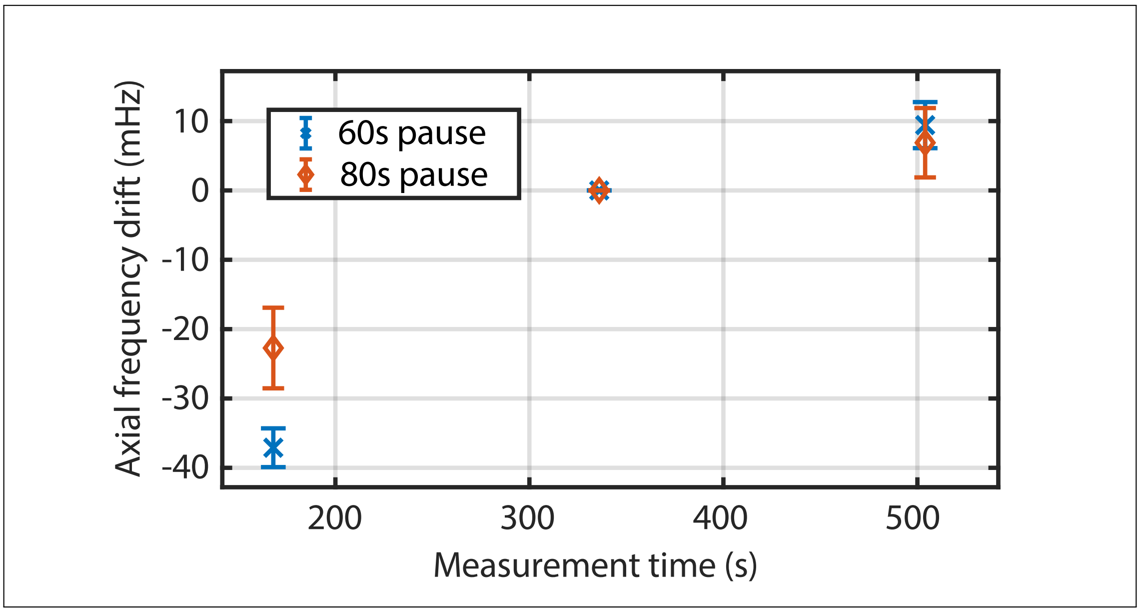

Figure 4.1: The modified measurement sequence to determine the axial frequency drift for two different waiting times after transport. The centre frequency measurement happens here during the exact time where the double-dip was recorded in the resonance measurements. The indicated measurement time for each point corresponds to the end of the interval during which the spectrum was recorded.

systematic uncertainty on ν_c since, in the double-dip measurement, the axial frequency contributes linearly to the determination of ν_p (see Eq. (2.26)). The measurement time is given as the end of each interval during which a dip has been recorded. As the times are chosen to be identical when compared to the actual measurement point, each frequency gives the average of that interval, where the centre one would be the *true* average axial frequency, during which the double-dip has been recorded.

To further improve upon this problem, the development of a dedicated transport switch box has been started. This will allow to switch between two voltage sources, which will enable us to keep the voltage of the precision supply *StaReP* [71] unchanged. The device then used for transport does not have to be as stable, completely eliminating the problem of the thermal voltage drift after ion transports. As the drift is much less critical when using PnA however, both because of a reduced dependency on the axial frequency as well as longer times before the actual modified cyclotron frequency measurement, the box has not yet been integrated into the setup.

4.1.3 Dip Lineshape and Resonator Frequency

The second factor limiting the precision of a double-dip measurement is the uncertainty associated with the fit and line shape of the axial dip and cyclotron double-dip. There have been recent investigations considering shifts associated with an erroneous determination of the resonance frequency of the tank circuit, as well as the ion being not exactly centred on the resonator [72], with both effects leading to an increased uncertainty of the axial frequency determination. These issues are mostly critical for double-dip measurements and only of diminishing concern when using phase sensitive techniques as the modified cyclotron frequency can be determined independently of the axial frequency which is one of the main advantages.

To study the dip line shape effects, all fitting parameters of the resonator are varied to check for variations of the derived modified cyclotron frequency. With most of these concerns only arising well after this measurement campaign had been concluded, there have been no specific investigations performed with the carbon ion, such as for example comparing the determined cyclotron frequency on resonance frequency versus a determination of the centre. Following the evaluation performed by S. Rau [72], the fitted frequency of the resonator is varied within the observed range of the results and dependencies of the input parameters. For the parameters of ALPHATRAP, one finds a dependency of the axial frequency on the resonator frequency offset $\Delta\nu_{\mathrm{res}}$ as

$$\Delta\nu_z = -17\,\frac{\mathrm{mHz}}{\mathrm{Hz}}\Delta\nu_{res}. \tag{4.2}$$

To translate this into an uncertainty of the extracted axial frequency, the uncertainty of the fitting of the resonator frequency is evaluated by modifying the fitting range for the resonator frequency determination as well as the Q-factor[a], which yields a shift of up to $\Delta\nu_{\mathrm{res}} = 140\,\mathrm{mHz}$ and 12 mHz, respectively. This contributes to the uncertainty of the fitted axial frequency as 2.5 mHz, or 1×10^{-10} as a relative uncertainty on ν_c, as the axial dip is required to determine ν_+ via the double-dip technique. The change of the Q-factor can additionally influence the determined axial frequency directly, however this effect seems to be small compared to the effect of the uncertainty of the resonance frequency, which already mostly depends on the chosen fitting range, rather then the Q-factor. This correction, of less than 1 mHz within reasonable values for Q, can be neglected for the study conducted here.

Additionally, a related effect arises for the fitting of the double-dip itself. The shift of the fitted ion frequency with respect to the resonator frequency seems to be related to the width of the dip, as both the left and right dip are only shifted by about half as much as the axial frequency. Therefore, one finds a (partial) cancellation in the effect when

---

[a] The quality factor of a resonator.

determining the modified cyclotron frequency via the relation

$$\nu_+ = (\nu_l + \Delta\nu_l) + (\nu_r + \Delta\nu_r) - (\nu_z + \Delta\nu_z) + \nu_{\mathrm{RF}}, \tag{4.3}$$

as given in Eq. (2.26). Ideally, if $\Delta\nu_l + \Delta\nu_r = \Delta\nu_z$, a full cancellation of the systematic shift would be observed. However, the extend of this cancellation seems to be further related to the position of the dip with respect to the resonator and working best, when being exactly at resonance frequency. Since this has not been considered at the time of the measurement, this effect cannot be treated as a systematic correction but rather as a worst-case estimate, as the position of the dips with respect to the resonator vary over time and from measurement to measurement. Therefore, the full effect is treated as a systematic uncertainty, labelled *Lineshape Dip* in Tab. 4.1 and is mostly specific to the carbon measurement but will be briefly revisited for the neon measurements. To be able to discuss and minimize the systematic effect further, a dedicated measurement, comparing the cancellation for different dip positions with respect to the resonance frequency of the tank circuit, coupling strengths and different ions to achieve different widths of the dip would have to be conducted. As the phase sensitive techniques achieve both higher precisions and partially circumvent the problem however, this study is unlikely to be performed soon.

4.1.4 Resonance Lineshape

To achieve an unsaturated resonance where the observed spinflip probability is well below 50% despite the long irradiation time of the microwave, multiple measurements were performed with subsequently reduced microwave power, adjusted via a manual attenuator. Consequently, over a range of a total of 10 recorded resonances, each roughly 1×10^{-9} in precision, the resonance lineshape changes from a Lorentzian lineshape when fully saturated[a] to a Gaussian shape when well below the saturation threshold[b]. In between, a Voigt fit of the form

$$P_{\mathrm{SF}}(\Gamma) = \int_{-\infty}^{+\infty} G(\Gamma')L(\Gamma - \Gamma', \gamma)d\Gamma' \tag{4.4}$$

---

[a] That means, the Rabi frequency is much larger than the statistical fluctuations

[b] When the Rabi frequency is much smaller, the shape is mostly determined by statistical fluctuations and the uncertainty of ν_c

with

$$G(\Gamma) = \frac{1}{2} e^{-\frac{\Gamma^2}{2\sigma_0^2}} \text{ and} \tag{4.5a}$$

$$L(\Gamma, \gamma) = P_{\max} \cdot \frac{\gamma}{\pi(\Gamma^2 + \gamma^2)} \tag{4.5b}$$

has been applied by using a Maximum-Likelihood fitting routine. Here, the Gaussian contribution σ_0, interpreted as all statistical influences from double-dip fitting to magnetic field jitter, has been fixed to reduce the amount of free parameters. The value of this is determined from the unsaturated resonances, evaluated using a pure Gaussian lineshape, where the statistical fluctuations are expected to be similar. It should also be noted that each resonance has been evaluated using all three lineshapes, with the resulting Γ only changing by about 0.3σ of the combined statistical precision. This is to be expected, as all lineshapes are symmetrical, restricting the possible change of the centre value. Fig. 4.2 shows the decrease of amplitude and width corresponding to the reduced microwave power and the resulting change of lineshape from a Lorentzian (top), Voigt (middle) and finally Gaussian (bottom) profile. Γ_{used} is the ratio of Larmor to cyclotron frequency that has been irradiated for each specific attempt, normalized by the fitted value Γ_{fit}. The green and red dots show the individual attempts, indicating successful (green) and unsuccessful (red) spinflip attempts respectively for each run. The green line represents the best fit according to Maximum-Likelihood optimization for the individual lineshapes, with the shaded area around being the 1σ confidence interval of the fit. The error bars only visualize one possible binning but are not used for fitting. The final result agrees within a combined 1.4σ difference to the result of the measurement performed in Mainz [69] well enough, that systematic shifts larger than low 10^{-10} for a double-dip measurement can be safely excluded and shows that our setup is operating as expected.

4.2 Neon *g* Factors

In this section, the g factors that have been measured individually for the two neon isotopes, $^{20}\text{Ne}^{9+}$ and $^{22}\text{Ne}^{9+}$ will be discussed. These measurements have been performed as an initial test of the system with the PnA method (see section 2.5.1) implemented into the measurement routine after the $^{12}\text{C}^{5+}$ campaign. Additionally, with the mass of ^{20}Ne known to only 8×10^{-10} relative precision [38], a g-factormeasurement of this ion has the potential to significantly improve upon the precision of the ion mass, which is of particular interest as a discrepancy of the mass had been observed in the former THe-trap experiment [73]. The there reported combined deviation of 4.2σ with respect to

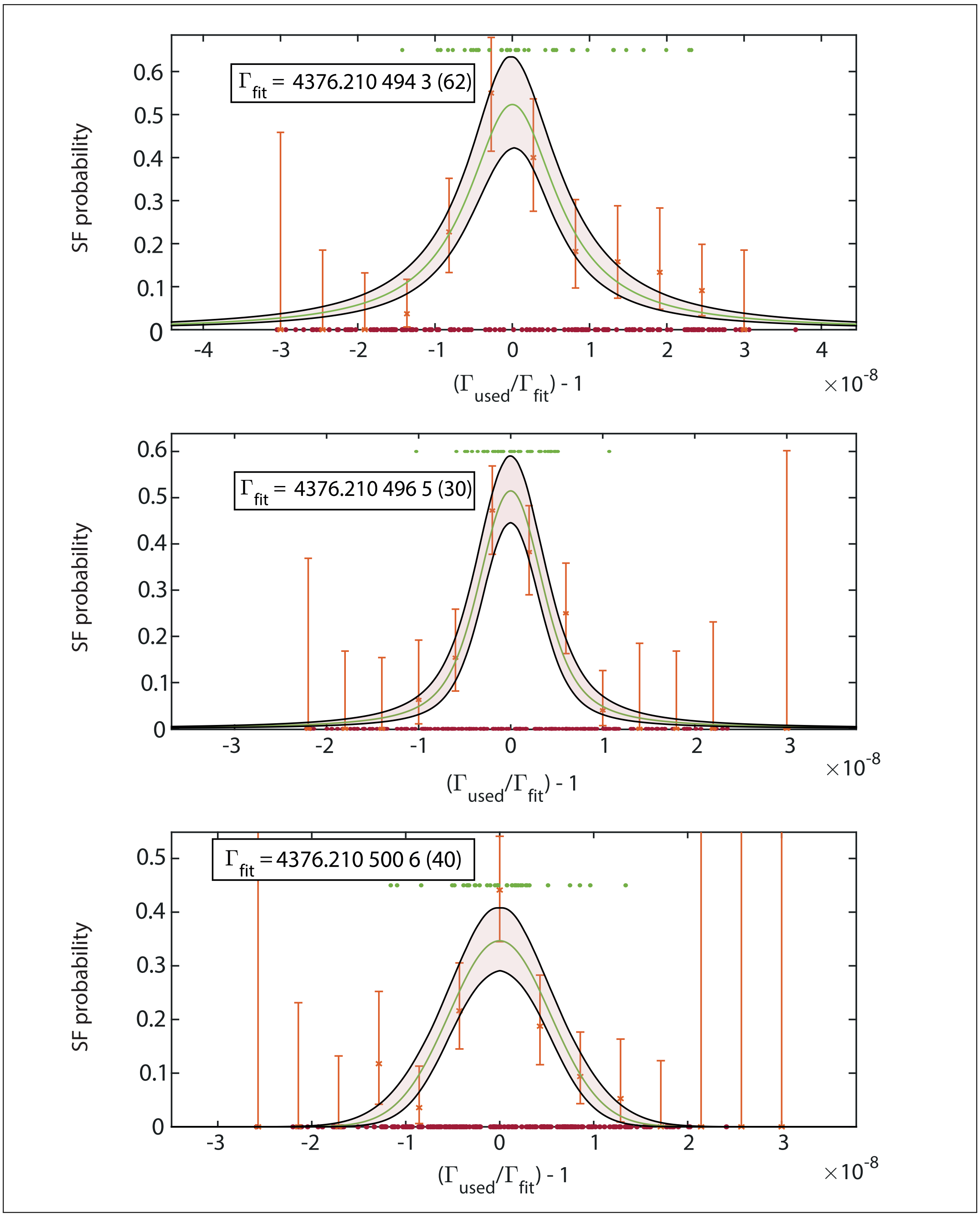

Figure 4.2: Comparison of different resonances, recorded for $^{12}C^{5+}$ with the microwave power being gradually lowered from top (Lorentzian), middle (Voigt) to bottom (Gaussian). For details see text.

the AME value could potentially be resolved by performing a *g*-factor measurement to extract the mass.

Here, first the measurement procedure will be described, which is similar for all six recorded resonances, three for each of the two isotopes. Subsequently, the possible sources of systematic errors, the impact of these results and potential future improvements will be discussed.

4.2.1 Measurement Procedure

The measurement cycle again begins with a single ion in the AT, where the initial spin state is determined as described in section 2.6. Upon successfully observing a spinflip to thus determine the spin state of the ion, it is transported into the PT by adiabatically[a] ramping the electrode potentials. Due to this transport and the uncertainty linked to the subsequent voltage drift observed in the carbon measurement, the waiting time upon arriving in the PT has been increased to 100 s instead of 60 s during former measurements. This allows for the voltages to settle, which ensures that the axial frequency is stable during the PnA measurement.

After briefly cooling both radial modes via sideband coupling, an axial dip spectrum is recorded and automatically evaluated to determine the axial frequency. If this is found to be different from the desired value by more than 1.5 Hz, the voltage is automatically adjusted to shift the ion exactly to the resonance frequency and yet another axial dip spectrum is recorded. While the axial frequency is not required to be of any specific value other than *close* to the frequency of the resonator, the phases of the signal during the PnA routine are always extracted from the same 2 Hz wide frequency bin.

The modified cyclotron frequency is first determined via a double-dip measurement, which is directly evaluated with the prior determined axial frequency to calculate the required frequencies for the PnA measurement sequence (2.5.1). This additional sampling of these two spectra adds yet more time to the sequence after the transport. The residual drift of the axial frequency is of no concern for these frequencies, and the actual determination of the cyclotron frequency begins subsequently with the PnA sequence. Here, the phases of both pulses of the sequence as well as the order of evolution times are randomized for each set, which helps to minimize possible systematic effects. One such effect is for example a dipole contribution of the second PnA pulse, [41] which is averaged when using random phases.

During the longest phase evolution time, 8.2 s for all measurements discussed here, the microwave is irradiated. This ensures, that the critical part[b] of the cyclotron frequency measurement occurs concurrently with the irradiation of the microwave, which makes the determination of the ratio of those frequencies as precise as possible. Finally, a second axial dip is recorded, that is used for the actual calculation of the free cyclotron frequency ν_c and compared to the first recorded one to exclude frequency drifts during

---

[a] The transport has been tested for possible heating effects during the work of I. Arapoglou [70]

[b] With respect to the magnetic field, as this frequency is used to "cancel" the magnetic field dependency

the PnA routine of more than some mHz[a]. The magnetron mode is cooled by coupling it to the axial mode before transporting the ion back to the AT, concluding the measurement cycle. The magnetron frequency itself is only recorded every 24th cycle, which corresponds to roughly 9 h with a single cycle taking on average 22 min. While the magnetron frequency is stable enough during a measurement campaign to not affect the derived cyclotron frequency, it significantly changes when the ring voltage is changed. This has to be kept in mind as the resonator frequency can experience shifts when filling the apparatus with liquid helium. If the ion is brought back into axial resonance then, the magnetron frequency should be updated correspondingly.

After concluding the measurement, a Maximum-Likelihood fit is performed to determine the ratio of Larmor to cyclotron frequency Γ. Here, all frequency pairs where a spinflip has been observed versus the ones without spinflip are evaluated using a lineshape according to microwave power and observed amplitude of the resonance[b]. For all fitting results, the parameters of amplitude, sigma and centre are additionally examined for possible correlation, which could allow for the centre to change when fitting a different amplitude or width, resulting in a nearby alternative optimum. This check is represented by 2D landscapes, where for each pairing of two parameters the optimal point of the third parameter is taken. For each of these points, the change of the Likelihood estimator is recorded. In Fig. 4.3, the change of the Likelihood function for each combination of parameters is colour coded to show the change in terms of σ compared to the optimum value. Each axis is scaled to show the change in that parameter in terms of its respective uncertainty σ. Ideally, one finds ellipses whose axis are aligned with the coordinate axes, indicating the correct convergence of the fit. A strong tilt or deviation from the ideal shape indicates a correlation between the parameters. Slight deviations from the ideal case are already included in the uncertainty of each parameter while fitting and can mainly be seen in the combination of σ and amplitude, where this is to be expected. Most importantly, the dependency of the centre value Γ_0 shows almost perfectly aligned axes with respect to both σ_0 and amplitude.

4.2.2 Resonances of $^{22}\mathrm{Ne}^{9+}$

The measurements for $^{22}\mathrm{Ne}^{9+}$ have been performed in the centre of the PT using the sixfold microwave multiplier over the course of three weeks. The first two resonances have been stopped with relatively low statistics of only 103 and 274 attempts to subsequently reduce the microwave power by several dB directly via the Anritsu microwave

---

[a] A drift of 5 mHz would for example correspond to a 5×10^{-12} relative shift on ν_c

[b] Here, the microwave power is adjusted to achieve about 30% maximum SF amplitude, which is well described by a Gaussian lineshape

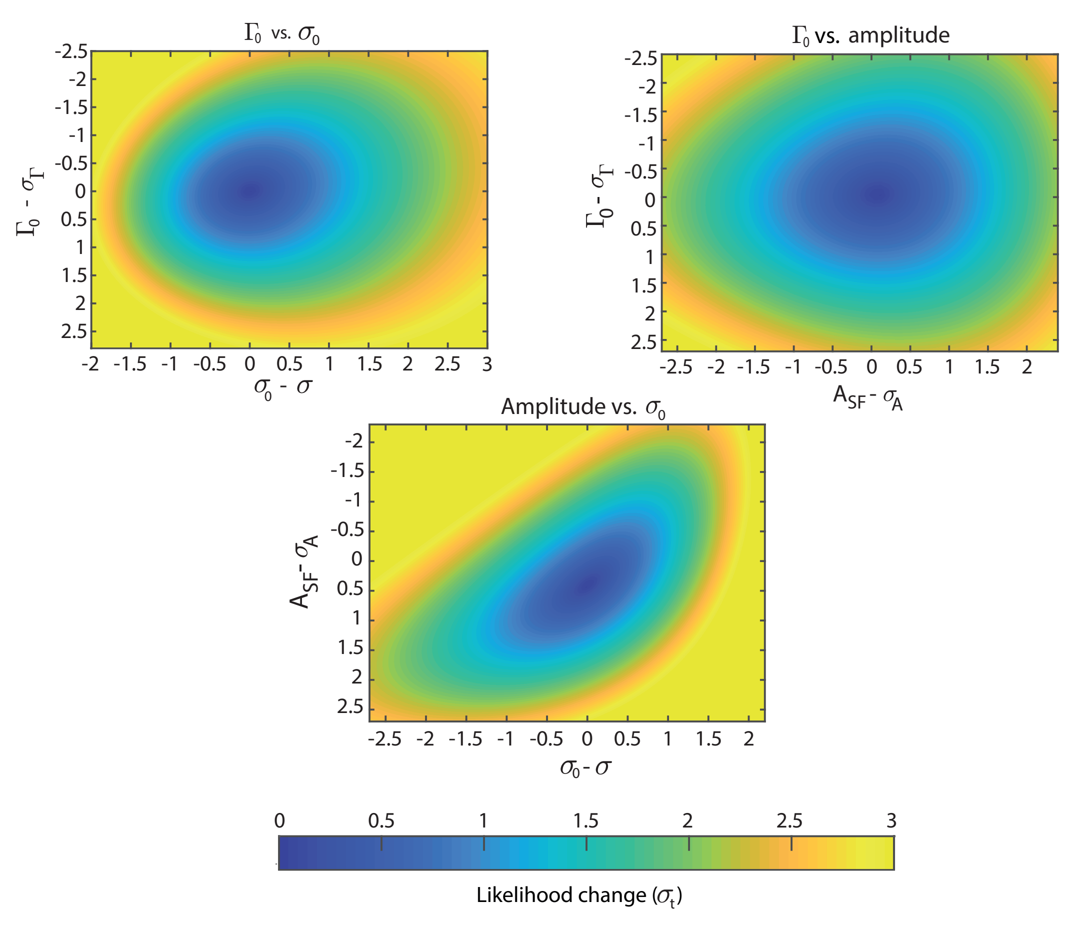

Figure 4.3: Investigation of parameters for a Maximum-Likelihood fit of a Gaussian profile, here for the example of a resonance for $^{20}\text{Ne}^{9+}$. While the two parameters on x and y axis are varied, shown here in terms of their respective uncertainty σ, the best value for the third parameter is taken, while recording the change of the Likelihood estimator compared to the best fit. The color scaling shows the overall Likelihood change normalized in terms of total uncertainty σ_t for all three plots.

generator output. Due to the highly non-linear behaviour of the multiplier in the non-saturated regime, this cannot be quantitatively translated to an actual reduction of irradiated power. However, the change can be qualitatively observed in both a reduction of resonance width and spinflip probability. With this probability thus adjusted to well below 50%, 594 attempts were recorded for resonance 3, which is shown in Fig. 4.4. Tab. 4.2 shows the evaluation summary of all recorded resonances and uncertainties, as well as the result for the atomic mass of ^{22}Ne.

To derive the atomic mass, Eq. (2.31) is re-written as

$$m_{\text{ion}} = \frac{\omega_L}{\omega_c}\frac{q_{\text{ion}}}{e}\frac{m_e}{g}, \tag{4.6}$$

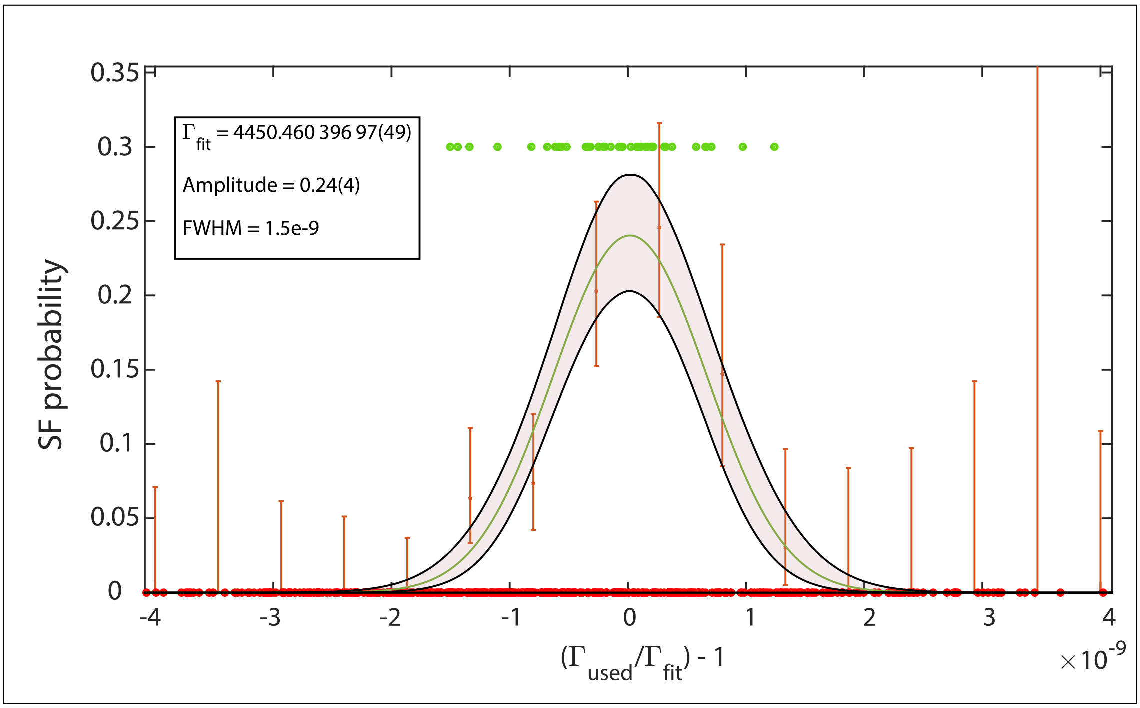

Figure 4.4: The main resonance for $^{22}\mathrm{Ne}^{9+}$. The green dots indicate the irradiated Γ where a spinflip has been observed, red ones indicate attempts without spinflip. This green line is the Maximum-Likelihood fit as a Gaussian distribution, the binned data is shown only for reference. The black lines around the shaded area show the 1σ confidence interval.

determining the mass of the ion first. Taking the theoretical prediction of the g factor and the electron mass as input parameters, one gains access to the atomic mass when correcting for the mass of the missing electrons and their binding energies. As this yields perfect agreement (within one combined σ) with the AME2020 and AME2016 value, the discrepancy seen in [73] seems to be stemming from other sources. Furthermore, this mass measurement yields an improvement to the current best value, taken from the AME2020 [38], by one order of magnitude, with the measurement being of similar precision as the state-of-the-art theoretical calculation [36, 37].

4.2.3 The Turbopump Setback

Just before starting the final measurement on coupled ions, one of our main (large! CF160, 600 $\frac{\mathrm{L}}{\mathrm{s}}$) turbopumps [75] of our room temperature beamline spontaneously burst[a]. The inner rotor was completely destroyed, producing tiny metal flakes and dust which covered most of the parts in the vertical part of the beamline, following the inrush of

---

[a] Thats the technical term, apparently. Extremely loud and violent explosion fits my experience more closely, though.

	Resonance 1	Resonance 2	Resonance 3
Start date	15.05.2020	20.05.2020	27.05.2020
Data points	103	274	594
stat. uncert.	3×10^{-10}	2.2×10^{-10}	1.1×10^{-10}
fitted Γ'	4450.460 395 95(133)	4450.460 398 90(99)	4450.460 396 97(49)
	relative shifts and uncertainties		
ν_z drift	$0(5) \times 10^{-12}$	$0(4) \times 10^{-12}$	$0(1) \times 10^{-11}$
spec. rel. shift	$5.1(13) \times 10^{-11}$		
ICS	$2.8(1) \times 10^{-11}$		
Lineshape dip	$0(2) \times 10^{-12}$		
T_z	5.0(3) K		
C_4 shift	$< 3 \times 10^{-13}$		
$C_{n\geq 6}$	$< 6 \times 10^{-15}$		
B_2 (ν_z PnA)	$-3(1) \times 10^{-12}$		
Cryo switch	$0(3) \times 10^{-11}$		
corrected Γ_0	4450.460 395 61(133)	4450.460 398 56(99)	4450.460 396 63(49)
Mean Γ	$4450.46039687(42)_{stat}(14)_{sys}$		
stat. uncert.	9.4×10^{-11}		
sys. uncert.	1.6×10^{-11}		
g (Theory)	1.998 767 263 640(117) [36]		
Masses			
$^{22}\mathrm{Ne}_{exp}$	**$21.991\,385\,098\,4(20)_{\mathrm{stat}}(7)_{\mathrm{sys}}(13)_{\mathrm{theo}}$** u		
$^{22}\mathrm{Ne}_{AME}$	21.991 385 114(19) u		
Input param.			
g factor	1.998 767 263 640(117) [37]		
m_e	$5.485\,799\,090\,65(16) \times 10^{-4}$ u [74]		

Table 4.2: The measurements performed for the single ion $^{22}\mathrm{Ne}^{9+}$ g factor. Rows with a single entry are valid for all three resonances. For the explanation of individual contributions see text.

air due to the ripped off pre-vacuum connection. Additionally, an electrically insulating ceramic vacuum part was broken, most probably due to the mechanical shock[a] of the beamline. This left the cryogenic section exposed to room pressure until the pneumatic valve, connected to an interlock system, was able to close. This seemed like an unfortunate and immediate end to the measurement campaign with the ions lost, trap and setup in an unknown state, but the next measurements already planned.
However, the help I received from all my colleagues, not only of the ALPHATRAP team, was amazing – we managed to clean the beamline, get the HC-EBIT back online (which had been vented while the cathode was heated) and our setup back into operation. Just

---

[a] A CF160 part was actually deformed and the rotating flange managed to turn quite a bit.

Figure 4.5: Sad left-overs of an Edwards STP-603 CF160 [75] turbo pump. Most pieces are completely stuck to the inner wall of the pump or to each other.

four weeks later, neon ions had already been loaded again and somewhat surprisingly, everything seemed to be still working. Being slightly shaken and not fully trusting the setup anymore, I decided to further delay the coupled ions measurement campaign again to record another single ion resonance, ensuring enough data to finish this thesis and to compare the state of the experiment to the prior one. As one of the most defining (or at least remembered) pictures of my PhD time, Fig. 4.5 shows the leftovers of this pump.

During the last weeks of writing this thesis, another pump of identical type burst as well, showing the same behaviour almost exactly one year later. The second pump burst without anyone directly present, but alarmed the technicians due to the explosion being heard in the complete building. The pump is from a different production batch according to the serial number. It is now planned to replace the last four identical pumps left in the setup as soon as possible.

4.2.4 The $^{20}\mathrm{Ne}^{9+}$ Resonances

In this section, the three individual measured resonances for the g factor of $^{20}\mathrm{Ne}^{9+}$ are presented. Fig. 4.6 shows the last and most precise of the recorded resonances for the

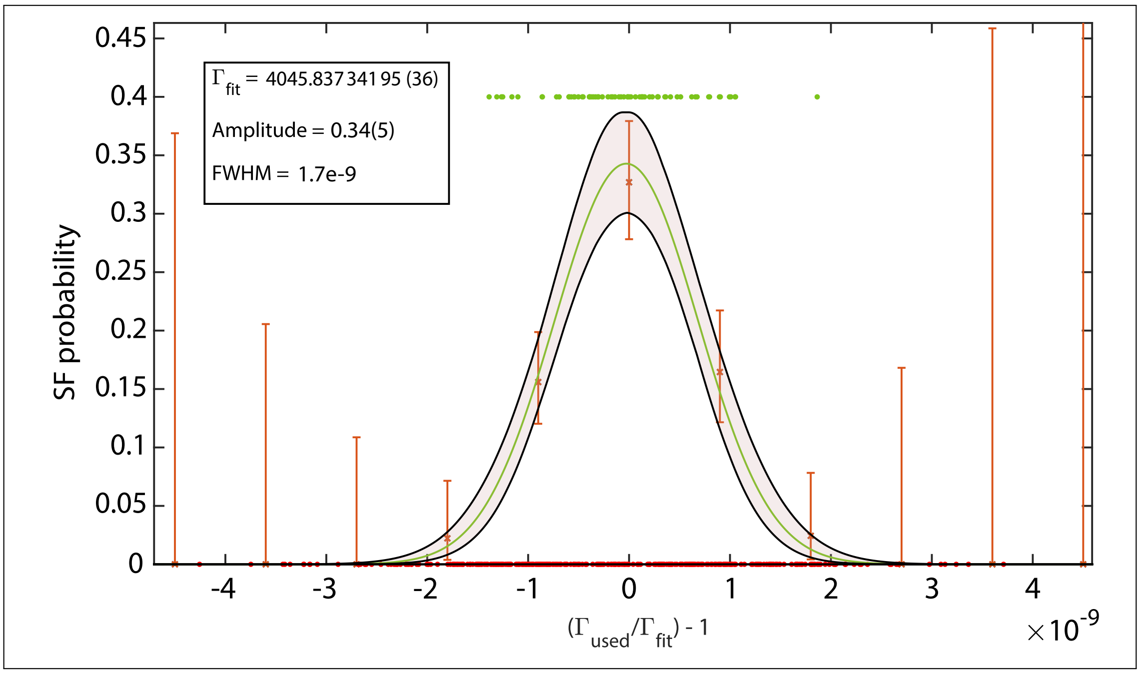

Figure 4.6: The most precise of the resonances for $^{20}\mathrm{Ne}^{9+}$, again with green dots for an irradiated ratio Γ, where a spinflip was observed, red ones without spinflip. The green line shows a Maximum-Likelihood fit of a Gaussian distribution, the binned data is shown only for reference. The shaded area indicates the 1σ confidence interval of the fit.

$^{20}\mathrm{Ne}^{9+}$ g factor, after the trap had been fully characterized again following the turbopump incident. The complete results are summarized in Tab. 4.3.

The last resonance is not only the most precise of the single ion measurements, but also still in agreement with the those measured initially, indicating that the setup is not unexpectedly performing in a different manner. While the mass determination from the combined value of all resonances is of similar precision as the current best value [38], a deviation of a combined[a] 3σ is observed. The same tension, already present with the combined first two resonances, triggered the further investigation of potential systematic effects as this is the first measurement performed at ALPHATRAP using PnA. Furthermore, it is also the first result that can be directly compared to literature values at similar precision.

Even after rigorous checks of both, the recorded data as well as the experimental parameters, no indication for a potential systematic shift to explain this deviation was found. It should also be noted, that the final resonance was recorded with different parameters, foremost after fixing a potential problem of the cryogenic switches (see section 4.2.5). This problem revolves around a transient DC voltage being generated by the switch

---

[a] This includes AME value, experimental and theory uncertainties

	Resonance 1	Resonance 2	Resonance 3
stat. uncert.	4.7×10^{-10}	2.7×10^{-10}	8.9×10^{-11}
Start date	29.04.2020	08.05.2020	20.11.2020
Data points	361	384	421
fitted Γ'	4045.837 342 07(190)	4045.837 341 89(110)	4045.837 341 95(36)[a]
		relative shifts and uncertainties	
ν_z drift	$0(2 \times 10^{-11})$	$0(3.5 \times 10^{-12})$	$0(1 \times 10^{-11})$
spec. rel. shift	$3.7(12) \times 10^{-11}$	$6.1(15) \times 10^{-11}$	$5.3(11) \times 10^{-11}$
ICS		$2.5(1) \times 10^{-11}$	
Lineshape dip		$0(2) \times 10^{-12}$	
T_z		5.7(3) K	
C_4 shift	$< 2 \times 10^{-13}$	$< 2 \times 10^{-13}$	$< 3 \times 10^{-13}$
$C_{n\geq6}$ shift	$< 4 \times 10^{-15}$	$< 7 \times 10^{-15}$	$< 6 \times 10^{-15}$
B_2 (ν_z PnA)	$-3(1) \times 10^{-12}$	$-3(1) \times 10^{-12}$	$0(1) \times 10^{-12}$
Cryo switch		$0(3) \times 10^{-11}$	
corrected Γ_0	4045.837 341 83(190)	4045.837 340 85(110)	4045.837 341 63(36)
Mean Γ		$4045.837\,341\,56(34)_{\text{stat}}(13)_{\text{sys}}$	
stat. uncert.		8.3×10^{-11}	
sys. uncert.		1.5×10^{-11}	
Masses			
$^{20}\text{Ne}_{\text{exp}}$		$\mathbf{19.992\,440\,167\,7(17)_{\text{stat}}(6)_{\text{sys}}(12)_{\text{theo}}}$ u	
$^{20}\text{Ne}_{\text{AME}}$		19.992 440 175 3(16) u [38]	
comb. diff.		3σ	
$^{20}\text{Ne}_{\text{Penta}}$		19.992 440 169 5(6) u (*Preliminary* [76])	
Input param.			
g factor		1.998 767 277 114(117) [36, 37]	
m_e		$5.485\,799\,090\,65(16) \times 10^{-4}$ u [74]	

Table 4.3: The results for the individual measurements performed for the single ion $^{20}\text{Ne}^{9+}$ g factor . Rows with a single entry are valid for all three resonances.

---

[a] This measurement has been performed in the asymmetric trap with $B_2 \leq 8\,\frac{\text{mT}}{\text{m}^2}$, reducing all related shifts even further.

upon starting and stopping an excitation drive. This leads to a shift of the axial frequency during the PnA pulses and immediately after, which affects the measured phase. The pragmatic solution was to keep the switch *off*[a] but use a longer pulse time and increased drive amplitude to achieve a similarly strong second PnA pulse for the ion. Additionally, resonance 3 was recorded in the asymmetric trap (see section 6.3.1), shift-

---

[a] With *off* I refer to it being of high impedance state for the applied drive, highly dampening it but not yielding the otherwise problematic DC potential anymore

ing the electrostatic minimum into a different and much smaller B_2, which also included a re-optimization of the electric potential. Due to the turbopump incident, this measurement was also done after a complete, involuntary thermal cycle of the cryogenic section, a reloading of ions and using a new, different microwave multiplier [66] combined with a programmable attenuator [67]. Despite all of these modifications, the last measured Γ is still in agreement with the ones measured initially, showing the same discrepancy, which was at that point considered to be most likely due to the wrong atomic mass of ^{20}Ne.

The unresolved deviation triggered a further investigation into the atomic mass of ^{20}Ne by our neighbouring experiment Pentatrap [63]. This Penning trap based mass spectrometer setup is currently[a] in the process of measuring the mass ratio of ^{20}Ne with respect to ^{12}C. First preliminary measurements indicate a likely deviation of 3.4σ with respect to the AME2020 value [38] and will most probably result in a reduction of the mass. The currently best preliminary result yields $^{20}\mathrm{Ne}_{\mathrm{Penta}} = 19.992\,440\,169\,5(6)\,\mathrm{u}$, which would show agreement within a combined 0.8σ with the result of the measurement performed here. If this value is to be officially confirmed once the final evaluation is finished, the result of the g factor of $^{20}\mathrm{Ne}^{9+}$ can instead by interpreted as a BS-QED test on the level of 9×10^{-11}.

Furthermore, this likely agreement highlights the performance of the setup and the newly implemented PnA technique. With the upcoming verification, the improvement of the ^{22}Ne atomic mass will further gain in credibility as well.

4.2.5 Discussion of Systematic Effects

In this section, all considered sources of systematic effects and measurements performed to evaluate these will be discussed. Many of these measurements will also apply for the characterization of the asymmetric trap as used in the coupled ions measurement 6.3.1.

Electric Anharmonicities

The discussion of systematic effects begins with the optimization of the electrostatic potential, as the first essential requirement to perform high precision measurements and determine the magnitude of other potential systematic contributions. The potential is optimized before each resonance measurement with a new ion by performing a tuning ratio measurement, where the ratios of the voltages applied to the correction electrodes versus the ring electrode voltage are varied. This is done as patch potentials, electrostatic variations across the electrode surfaces due to non-conducting depositions, could

---

[a] As of one week prior to handing in this thesis

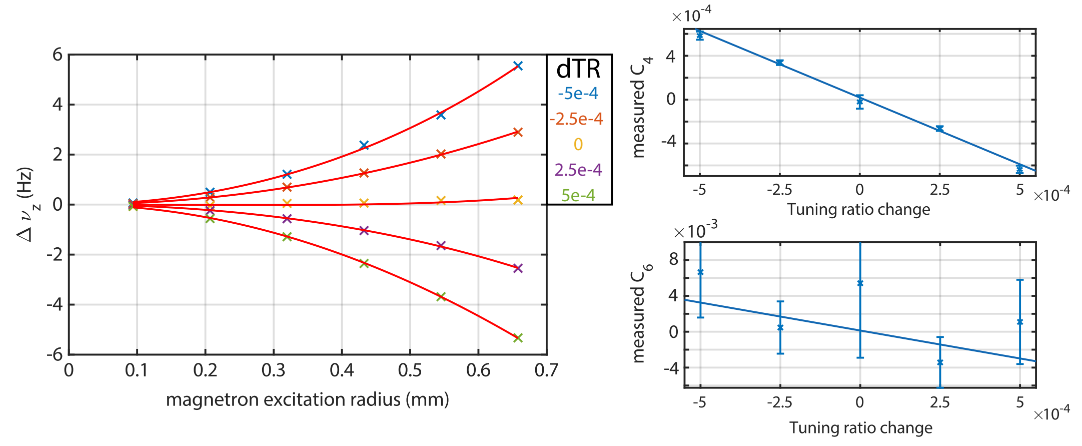

Figure 4.7: A tuning ratio scan performed with $^{20}\mathrm{Ne}^{9+}$, where the left hand side shows the axial frequency shift $\Delta\nu_z$ measured for different tuning ratio settings, where the ratio of voltages is changed by the offset dTR, different for each set of coloured marks. Each slope is fitted with a combined polynomial for C_4 and C_6, with the extracted contributions shown on the right hand side.

be altered when injecting ions or modify the harmonic potential, when working with significantly different ring voltages.

Despite this optimization, the residual uncertainties of C_4 or even C_6 have to be considered. One such measurement is shown in Fig. 4.7. Here one compares the axial frequency of the cold ion to an ion excited to a certain magnetron radius, while varying the tuning ratio. Each curve corresponds to a slightly altered tuning ratio, with the frequency shift $\Delta\nu_z$ being measured at the corresponding radius r_- compared to a thermalized ion. These points are then fitted with a polynomial fit to extract the C_4 and C_6 of the individual settings. Finally, the individually extracted anharmonicities are compared to the change in tuning ratio to extract the point where this contribution becomes zero. The uncertainty for this value determines the potential systematic shift when performing a PnA measurement. With a residual uncertainty for $|C_4| \leq 3 \times 10^{-5}$ and $|C_6| \leq 7 \times 10^{-3}$, the corresponding relative frequency shift on the free cyclotron frequency is less than 6×10^{-15} (for PnA, even less for double-dip) and can be safely neglected here. Additionally, the axial frequency is shifted during the PnA measurement, due to the excitation of the cyclotron mode. This amounts to a potential shift of $\Delta\nu_z = 0.3\,\mathrm{mHz}$ due to C_4, which causes the calculation of the free cyclotron frequency, performed with the axial frequency measured with a cold ion, to be wrong by about 3×10^{-13}. With more than two orders of magnitude below the statistical error, also this effect can be safely neglected here.

In principle, the observed axial frequency shifts also depend on other contributions, specifically C_3 and B_2. As these measurements are done with the magnetron mode in the PT where our B_2 contribution is small anyway, the additional effect of the magnetic field contributions can be neglected. It is helpful to remember that the axial frequency shifts caused by magnetic inhomogeneities are related to the magnetic moment of the ion and therefore small for magnetron excitations but considerably larger for the cyclotron mode.

Furthermore, as has already been pointed out in the beginning (see section 2.2.1), a $C_4 = 0$ is not actually achieved for zero observed shifts, but rather only the point where $C_4 = {}^{3C_3^2}/_{4C_2}$. For the symmetric trap, the C_3 contribution can be assumed to be small, as all voltages are applied symmetrically. The derived uncertainty for the additional C_4 is far below what can be resolve.

For the single measurement in the asymmetric trap, simulations of the electrostatic potential already yield $C_3 = 2 \times 10^{-3}$, which translates into a possible $C_4 \approx 5 \times 10^{-6}$. If when assuming a 100 % uncertainty for the simulation based C_3 contribution, this does not result in an additional uncertainty at this point but will be of interest when considering the coupled ions.

Relativistic Shift and Cyclotron Radii Calibration

Having thus optimized the electrostatic potential, the effect on the axial frequency can be compared between excitations of the magnetron mode and modified cyclotron mode. The latter is subject to the additional effects of magnetic inhomogeneities and the relativistic mass increase. As the effect of this mass increase only has a tiny impact on the axial frequency (single mHz even with several 100 µm of modified cyclotron radius), the comparison between the shifts can be used to place limits on the magnetic inhomogeneities.

However, the required radii to achieve measurable axial frequency shifts are significantly larger than the radius of the modified cyclotron mode during PnA, which culminates in the requirement of a linear interpolation from the large measured radii to the small radii then used. To limit the effect of a possible non-linear dependency of the radii on the excitation, one only scales the time of the excitation pulses rather than their amplitude, as one expects a possible non-linear transfer functions to be more likely to depend on applied power rather than time. This process, combined with possible magnetic inhomogeneities, leads to the error being conservatively estimated to 10% of the determined radius, based on simulations and the observed robustness for different ion species.

The mass increase during the measurement sequence of PnA results in a smaller cyclotron frequency, which in turn leads to a measurement of a too large Γ. The resulting relative shift of about $5(1) \times 10^{-11}$ is included as a systematic correction and contributes the second largest single systematic uncertainty due to the dependency on precisely determined radii.

To independently verify those radii, the cyclotron frequency dependence on the radius can be compared to the expectation of the relativistic shift. To this end, PnA is used to measure the phase evolution for different excitation radii. Here, one expects the shift of the modified cyclotron frequency ν_+ to follow [77]

$$\frac{\delta\nu_+}{\nu_+} = -\frac{\nu_+}{\nu_+ - \nu_-}\frac{v^2}{2c^2} \approx -\frac{(2\pi\nu_+ r_+)^2}{2c^2}, \tag{4.7}$$

with the corresponding radius r_+, the magnetron frequency ν_- and the vacuum speed of light c. This is fit to the data shown in upper part of Fig. 4.8. When comparing the scaling of this fit to the one expected from Eq. (4.7), one finds that the thus measured radii seem to be too small by 3.7%. This is well in agreement with the calibration of the C_4 method, given the assigned error of 10%. The small curvature that can be observed in the lower part of Fig. 4.8 is a quartic dependency, stemming from either a C_6 or a B_4 contribution. If this correction is extrapolated to radii around 20 µm, the relative shift is of less than 4×10^{-14}, assuming a scaling of at least $\propto r^4$ and can be neglected here. Finally it should be noted, that the uncertainty of the relativistic shift (or its correction) can be significantly improved by recording resonances for different PnA radii and then fitting the expected quadratic behaviour of the relativistic shift versus the chosen cyclotron radius. When extrapolating the thus obtained values for Γ to the zero radius point, this uncertainty can be strongly reduced as shown for example in [69], Fig. 17. As this was not performed here, the relativistic correction poses the second largest systematic uncertainty of these measurement, however still about one order of magnitude below the statistical precision. Finally, it has to be noted that the effect of special relativity also has an impact on the Larmor frequency. However, this effect is suppressed by a factor of $\Gamma = \nu_L/\nu_c \approx 4000$ [48]. This leads to a correction of 1.5×10^{-14} and can also be neglected for these measurements.

Magnetic Inhomogeneities

The modified cyclotron frequency is shifted due to the enlarged radius during PnA and the effective different magnetic field due to a B_2 contribution. This is mostly compensated by the Larmor frequency undergoing the same relative shift (see Eq. (2.21)). However, the axial frequency is shifted during the measurement of the modified cyclotron frequency due to the additional magnetic moment (see Eq. (2.22)) during the PnA cycle. This frequency shift amounts to roughly $\Delta\nu_z \approx 3\,\text{mHz}$ and requires a correction of the free cyclotron frequency of -3×10^{-12} for all but the measurement performed in the asymmetric trap with a significantly reduced B_2.

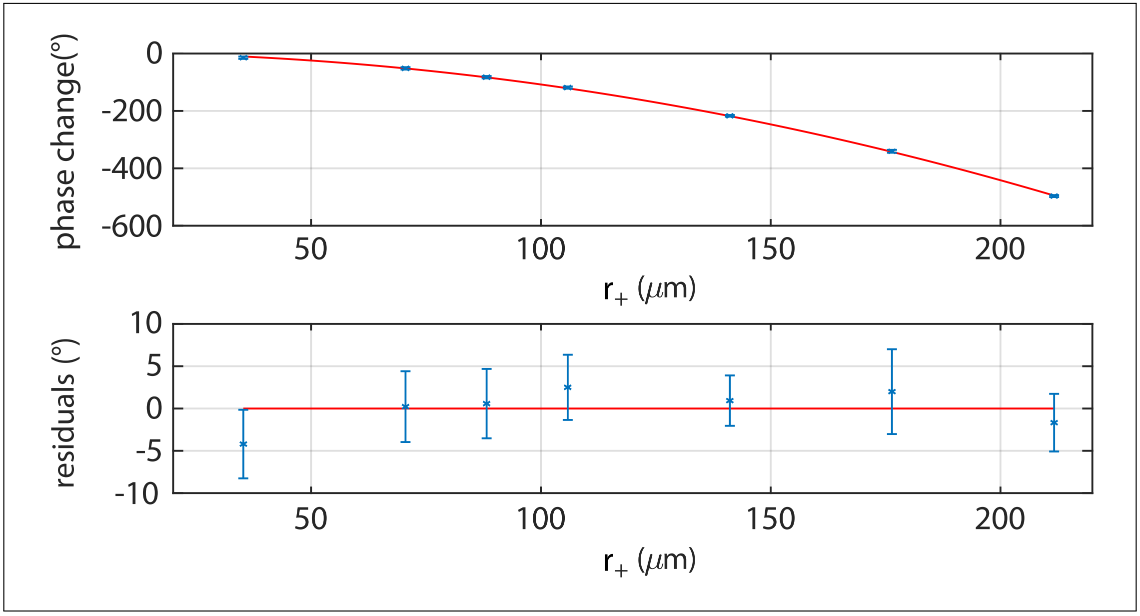

Figure 4.8: The change in measured phase for different excitation radii and the residuals when compared to the expected behaviour. For details see text

Image Charge Shift

The image charge shift (ICS) arises due to the image charges induced into the electrodes by the ion. This introduces an additional potential, that due to the back action on the motion of the ion results in shifted frequencies. This shift has been discussed extensively in [78] and is assumed to be predictable to 5% precision. It can be calculated as

$$\frac{\Delta\nu_c}{\nu_c} \approx -0.994\frac{m_{\text{ion}}}{4\pi\epsilon_0 r^3 B_0^2} \tag{4.8}$$

with the radius of the trap r and the correction factor stemming from the trap geometry [56][a]. As the sign can be a bit confusing, depending on which derivation one follows, let's clarify: the measured cyclotron frequency will be measured too small, leading to a Γ that is too large (positive shift). This means, that the corrected Γ has to be smaller. It has been corrected for all measured resonances, with the residual systematic uncertainty being in the low 1×10^{-12} regime.

Temperature Measurements

The temperature of the ions has been evaluated by performing a Maximum-Likelihood fit to the observed axial frequency offset in the AT for each cycle of the respective measurement. These shifts encode the cyclotron energy according to Eq. (2.21), after being

---

[a] Using $\epsilon_r = 1964(98)\,\frac{\mu\text{V}}{\text{m}^2}$ for our trap and comparing the results from Eq. (14) and (17) in [78]

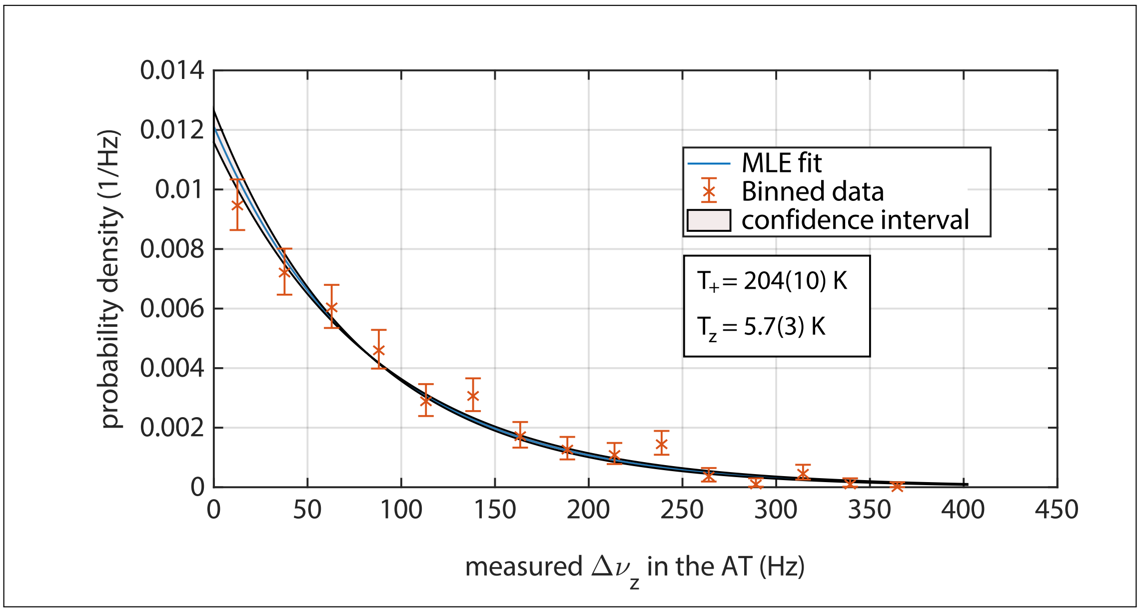

Figure 4.9: Maximum-Likelihood fit for a Boltzmann distribution of the measured axial frequencies, to extract the lowest possible frequency shift and cyclotron temperature during the PT measurement. The distribution occurs due to the ion having a different cyclotron temperature each cycle in the strong magnetic bottle (B_2) of the AT.

coupled to the axial mode in the PT. This allows to determine the temperature via [41]

$$p(\Delta\nu_z^{AT}) = \Theta(\nu_z^{AT} - \nu_{z,0})\alpha e^{-\alpha\left(\nu_z^{AT}-\nu_{z,0}\right)} \quad \text{with} \tag{4.9a}$$

$$\alpha = \frac{4\pi^2 B_0^{AT} m_{ion} \nu_{z,0}}{B_2^{AT} k_B T_+}, \tag{4.9b}$$

where $\nu_{z,0}$ corresponds to the frequency which would be observed for a ground-state cyclotron energy, producing no shift. The Heaviside function Θ restricts $\nu_{z,0}$ to values smaller than the actual observed ones, effectively excluding negative energies or making sure that $\nu_{z,0}$ cannot be larger than any actually measured value. Now, both the frequency for the coldest possible ion as well as the cyclotron temperature can be extracted, which is related to the axial temperature by

$$T_{z,\mathrm{PT}} = \frac{\nu_{z,\mathrm{PT}}}{\nu_{+,\mathrm{PT}}} \frac{B_{0,\mathrm{AT}}}{B_{0,\mathrm{PT}}} T_{+,\mathrm{AT}}. \tag{4.10}$$

One exemplary evaluation, here for the g factor of the last $^{20}\mathrm{Ne}^{9+}$ measurement, is shown in Fig. 4.9, while the carbon measurement showed on average $T_{z,\mathrm{PT}} = 7.1(4)$ K and $^{22}\mathrm{Ne}^{9+}$ was evaluated to an average of $T_{z,\mathrm{PT}} = 5.0(3)$ K. Neither temperature results in necessary systematic corrections.

Resonance Lineshape with B_2

All resonances have been evaluated using a symmetric resonance lineshape, of either Gaussian, Lorentzian or Voigt type. However, the continuous thermalisation of the ion in its axial mode during the irradiation of the microwave, combined with a residual B_2, leads to a convolution of the lineshape with a Boltzmann distribution. This arises from the fact, that the cyclotron frequency is determined individually each run, while the Larmor frequency can only be extracted from the full set of measurements. As this is not a symmetric distribution, the centre value of the resonance can be shifted. This shift has been evaluated by Verdú [79] and Köhler [41] extensively. In the case of a Lorentzian distribution, this can be written as

$$p_{sf}(\Gamma^*) = \frac{1}{2}\int_0^\infty \frac{\gamma^2}{\gamma^2 + (\Gamma_0 + \alpha_{B_2}(E_z - \overline{E_z}) - \Gamma^*)^2}\frac{1}{k_B T_z} e^{-\frac{E_z}{k_B T_{z,AT}}}\, dE_z, \tag{4.11}$$

with $\alpha_{B_2} = \frac{B_2}{B_0\omega_z^2 m_{\text{ion}}}\Gamma_0$. The shifted centre value of this modified distribution (compared to the $B_2 = 0$ case) can be used to infer the error made by using a symmetric distribution to a relative 1.5×10^{-16} with measured temperatures of $5.7(3)$ K (see Fig. 4.9) and can be neglected here. This is due to the combination of a low axial temperature, and the small $B_2 = 0.0643(32)\,\frac{\text{T}}{\text{m}^2}$ (symmetric trap) [18], and is even lower in the asymmetric trap.

Currently, effects due to a B_2 contribution in combination with the irradiated microwave power are again under further investigation. Specifically, as the resolution (or width) of the resonances become ever smaller due to an increased cyclotron frequency resolution, more stable magnetic fields and reduced axial temperatures, the width is already close to the Lorentzian line-width, given by the microwave power or Rabi frequency. While a Boltzmann distribution convoluted with a drastically broader Gaussian distribution does not produce significant shifts, the asymmetry of the Boltzmann distribution becomes more important for narrower resonances. These effects are currently considered numerically and preliminary results predict the effects to be tiny still for the specific parameters of microwave power, B_2 and ion masses used within this thesis.

However, these considerations might become more important for lighter ions due to the increased axial amplitudes or when working with significantly larger B_2 contributions or temperatures. Experimentally, neither for the carbon measurement compared to the experiment performed in the Mainz setup [69], where B_2 was larger by about one order of magnitude, nor for the $^{20}\text{Ne}^{9+}$ measurement, performed in the symmetric (Resonance 1 & 2) and asymmetric trap (Resonance 3) where the B_2 was reduced by an order of magnitude, could a dependency on B_2 be observed. Therefore, while the B_2 contribution does not affect the results of the g-factor measurements here, it should not be generally discarded.

Dip Lineshape

The extraction of the axial frequency by performing a fit with a fixed lineshape requires full understanding of the system and in principle also of the transfer function of all electronics used to extract the signal. Possible frequency shifts have been more extensively evaluated in combination with the frequency dependency of the resonator in the case of carbon. Similarly, such an evaluation is repeated here, yielding an uncertainty of 1.5 mHz for the axial frequency determination for the neon ions, slightly less compared to the carbon case. This is due to the measurement being performed in the *low Q* mode, where the resonator Q-factor is reduced via a Q-switch [49] from roughly 40 000 to only about 8000, reducing the dip width as well. Furthermore, as the axial frequency only enters via the invariance theorem (see Eq. (2.6)) and the reduced cyclotron frequency has been determined via the PnA method, the effect on the free cyclotron frequency is only 2×10^{-12} and not relevant on the current level of precision.

DC Voltage of Cryogenic Switch

During the measurement campaign of the last resonance, an axial frequency shift just after applying an excitation was observed. As the effect vanishes quickly, it went by unnoticed in the long time-averaged spectra that are normally observed. The effect became visible only in a direct comparison of amplitudes recorded directly after the PnA sequence for short times.

The shift has been investigated after observing a change of the axial frequency directly after applying an excitation. The origin of this effect could ultimately be traced to the cryogenic switches, which are used to change the coupling strength of the external excitation lines to the electrodes. The layout of these cryogenic switches (see Fig. 4.10 [49]) is such, that an applied drive is always capacitively coupled to the excitation electrodes. The switch is then operated by changing the behaviour of the capacitive voltage divider by achieving a strong suppression (*closed* or *off*) or allowing for a stronger coupling (*open* or *on*). Unfortunately, the switch rectifies part of the signal due to the non-linear characteristics of the JFET, which generates a DC burst. This voltage will momentarily couple to the electrode. This in turn will shift the axial frequency at the start and end of the coupling pulses of a PnA sequence. The behaviour can be qualitatively simulated, when approximating the time constant of the system. This depends on several 100 MΩ

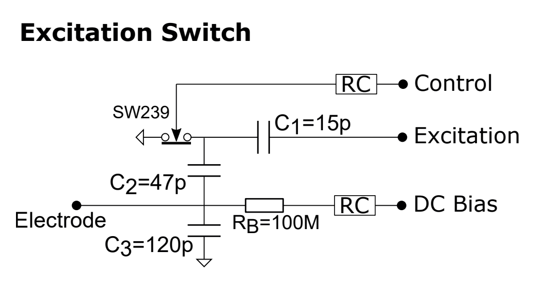

Figure 4.10: The design of the cryogenic excitation switches. Figure taken from [49].

to 200 MΩ[a] resistors, connected between the split electrode used for excitation and to the connected voltage supply. With a capacity of the complete system in the range of about 200 pF, a time constant of several 10 ms to a few 100 ms can be expected. During this time, the axial frequency chirps back to its nominal frequency, while the voltage equalizes back to the applied DC voltage.

This behaviour can best be visualized, when observing the time-domain signal, shown in Fig. 4.11. This shows the axial frequency dependence in the case where both switches are *on*, while a 10 MHz pulse is applied to the Q_{xz} electrode for 0.5 s with an amplitude of $V_{pp} = 6\,\mathrm{V}$. While this is a significantly stronger pulse compared to what normally is applied (about a factor of 10 stronger, actually), the frequency is detuned from any of the ion's modes and or their combinations. This ensures, that any observed effect is only related to the drive but not in any direct interaction with the ion. To be able to observe the ion's behaviour, it is first detuned from the centre of the resonator and axially excited to observe the axial frequency as a peak amplitude, now visible as the horizontal yellow line. The first vertical yellow line corresponds to the Q_{xz} drive being applied, causing a spectrally broad signal in the beginning. The ion is detuned to lower frequencies, but cannot be easily identified while the drive is still applied. The second line corresponds to the drive finishing and being switched off, causing another broad excitation as obvious from the increased signal in all frequencies. Directly after, the ion can then be observed to chirp back to its original frequency over a time period of about 500 ms, until the resolution is too low to still observe a frequency difference. The amplitude at the end is lower due to the slow thermalisation of the ion with the resonator during this sequence. The effect is strongly suppressed when the switch is off, which however also results in a strongly reduced strength of the drive reaching the ion. To compensate, a significantly stronger drive and an increased pulse duration are used instead, calibrated to achieve a comparable signal strength for the phase readout. Unfortunately, this has

---

[a] This is only approximate due to the strong change in resistance when cooled from room temperature (100 MΩ) to 4 K, where they are closer to 200 MΩ in resistance.

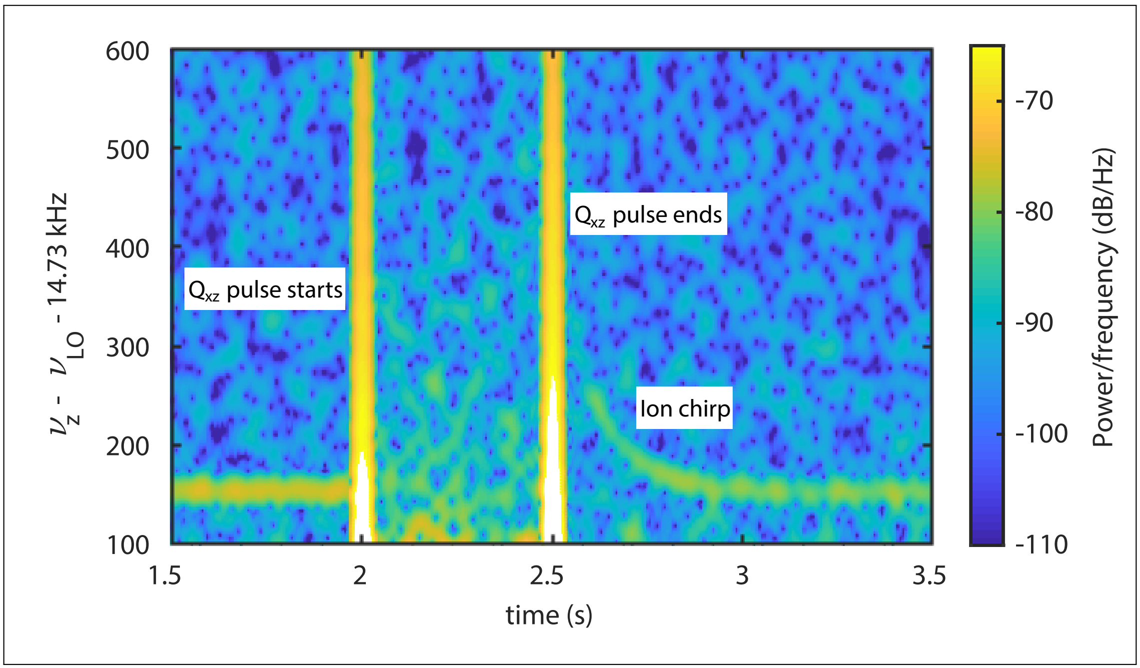

Figure 4.11: Behaviour of the axial frequency during and after a Q_{xz} pulse. Despite the excitation being far detuned from all ion modes, the ion can be observed to shift and chirp back to its original axial frequency at the end of the pulse. For details see text.

only been done for the second PnA pulse of the last recorded resonance, leading to the requirement of intensive comparisons of the measured phase depending on the state of the switch. The other resonances have been recorded with both switches on, however the phase has only been recorded 150 ms after the Q_{xz} pulse, after which the voltage offset had diminished to not be noticeable anymore when using lower drive amplitudes. Possible effects related to

- the waiting time after the second PnA pulse
- the differences between switch off vs switch on
- effects on the shortest evolution time, to exclude effects of the first PnA pulse

have been investigated.

To exclude effects due to different waiting times before the SR1 is triggered at the end of the PnA cycle, two separate phase differences are recorded and compared. This is done by measuring for two evolution times, $\tau_{1,0} = 0.2$ s and $\tau_{1,1} = 8.2$ s. For the first phase difference, the FFT sampling begins 1 ms after the end of the second pulse for both evolution times. The second phase difference is recorded for identical evolution times, however the signal is now recorded starting 150 ms after the end of the second pulse.

The comparison of these two phase differences is found to be identical within 1σ of the statistical resolution[a] of about 1°, which corresponds to a relative resolution of the cyclotron frequency of 1.4×10^{-11}, averaged over 100 cycles. The result is shown in Fig. 4.12, inset (A). Therefore, dependencies on the waiting time after the second PnA pulse can be excluded.

Similarly, such measurements have been performed for all possible combinations of switch on versus switch off. However, since none of the times of the sequence have to be changed, the phases recorded for individual settings of the switches can be directly compared instead of having to compare pairs of phase differences as before.

Insets B, C and D show the recorded differences for 240 cycles of each of the corresponding measurement settings. The four possible settings (resulting in three graphs of their respective differences) are all compatible with zero within 1σ, for simplicity all graphs show the direct comparison with respect to the off-off setting, corresponding to the D_x switch off and the Q_{xz} switch off, respectively. If any related effect is assumed to be completely covered within the used measurement time of $\tau = 4.2\,\mathrm{s}$, one can postulate that the absolute difference observed here is the same if measuring for the full evolution time of $\tau = 8.2\,\mathrm{s}$ as used in the actual measurements. This results in a lower standard deviation due to the reduced magnetic field jitter as the time is shorter, while the full resolution of the examined effect when scaling it to the full measurement time is achieved. The thus derived upper limit for a potential systematic shift is 2.6×10^{-11} and is included for the measurements of both neon isotopes as a systematic uncertainty. For future measurements, further care has been taken by J. Morgner to optimize the PnA routine. To this end, a *pulse shaping* routine has been implemented, to allow smoother applications of the drive, especially when using excitation pulses starting with anything but a zero phase. This new scheme has been found to yield consistent results compared to the routine applied here and will be discussed in his thesis more closely.

---

[a] The standard deviation of all differences, divided by the square-root of the amount of data points, the difference is consistent with zero.

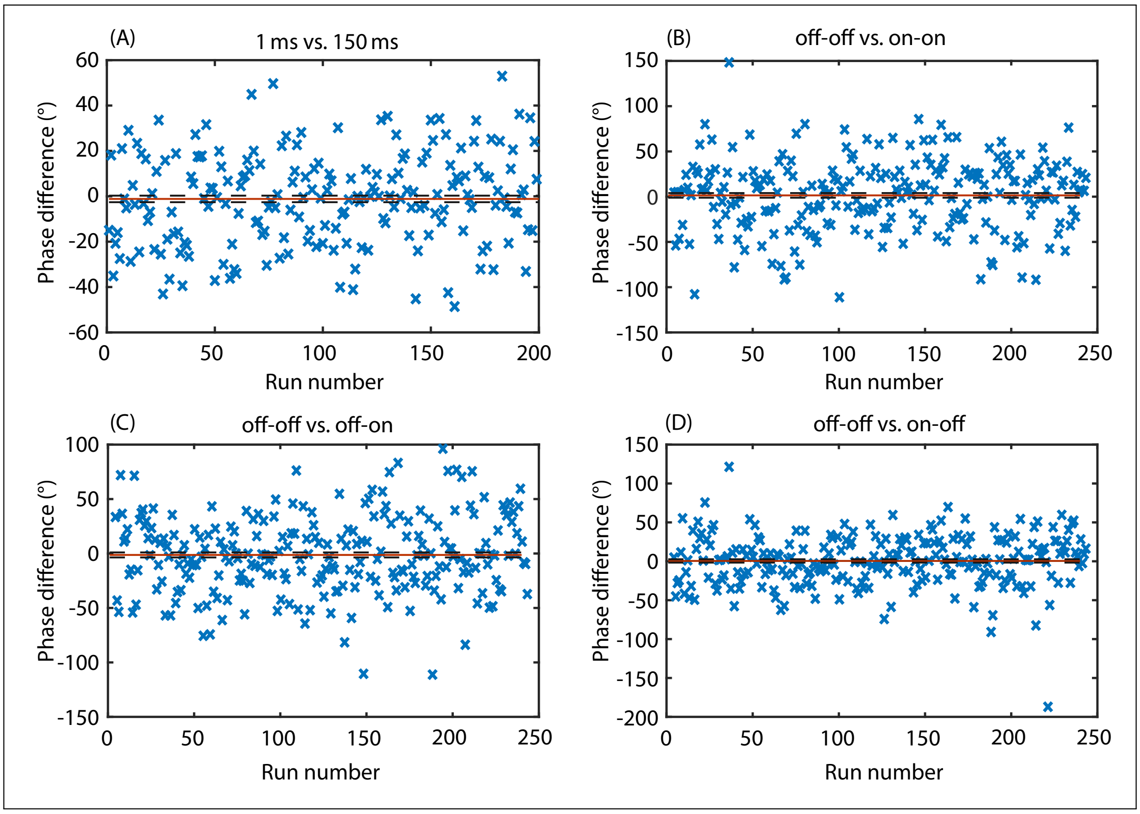

Figure 4.12: Tests for potential systematic effects based on the dependency of different switch and PnA settings. Inset (A) compares the measurement of the phase directly after the second pulse versus a delay time of 150 ms. Insets (B) to (D) directly compare the phase difference for all different combinations of switch states. Systematic effects can be excluded here on a level of about 2×10^{-11}.

5 Coupled Ions: The Coupled Motion

5.1 The General Idea

The idea of using coupled ions in a Penning trap is not new and ion crystals are commonly used for laser spectroscopic measurements [80, 81]. This technique, or more specifically, the adaptation of the method developed in the context of this thesis, is strongly based upon the work performed at MIT by S. Rainville [82, 83] and J. Thompson [84]. They have shown that two ions, coupled as a magnetron ion crystal, can be used to perform extremely precise mass comparisons based on the groundwork laid by E. Cornell in the early 90s [85]. The main motivation there was to suppress the inherent magnetic field fluctuations, stemming from both external sources as well as the magnet itself, which were severely limiting their possible measurement time and ultimately also the final precision. While these restrictions are not quite as severe for our setup and do not limit our possible measurement time to only certain hours during the night, the magnetic field fluctuations still restrict the possibility of *how* the Larmor frequency can be obtained. Furthermore, the masses of the measured ions are additionally required to be of sufficient precision to enable the comparison of absolute g factors, as they are direct input parameters.

Despite the advances of phase sensitive techniques [55], the measurement time (or phase evolution time) required to determine the cyclotron frequency precisely enough[b] renders it impossible to coherently measure the Larmor frequency in the same time frame. This is due to inherent (and external) magnetic field fluctuations, which induce a loss of coherence with respect to an externally applied microwave drive. This culminates in the need of a statistical evaluation, where the frequency ratio can only be extracted from a fit to the complete distribution, mostly given by these fluctuations[c].

Ultimately, this limits the precision that can be achieved, depending on how far one is willing to *split the line* – or how precise one wants to determine the centre of a distribution. Related to this is the time one requires to achieve the statistical precision to

---

[b] It takes about 10 s of evolution time to achieve relative precisions of low 10^{-10}, see Eq. (2.28).

[c] This is at least the case if the measurement parameters are chosen to not let other effects, such as power broadening, determine the line shape.

measure a distribution of some 1×10^{-9} FWHM to low 1×10^{-11} for the centre value. Here, we want to get around both of these restrictions, while, as an added benefit, removing the need of precise masses for the ions and the electron. Also the need of an extremely precise magnetic field measurement is strongly relaxed, typically by a factor of order $\Delta\nu_L/\nu_L$, with $\Delta\nu_L = (\nu_{L,2} - \nu_{L,1}) \ll \nu_L{}^a$. Finally, having the ions in the same potential results in them experiencing the same fluctuations of the electric potential due to the applied voltage. While not yet of concern during typical measurements, this benefit will become useful when one is also interested in precise cyclotron frequencies.

The method developed, implemented and successfully applied during the course of this thesis is meant to measure the difference of g factors as opposed to masses which was the case in the *Ion Balance* [83]. As already successfully shown at MIT, the magnetic field fluctuations can be strongly suppressed in the ratio of the cyclotron frequencies when looking at the two ions in close proximity where coherence could be shown for several 100 s despite a noisy magnetic field environment. This works as long as both ions experience identical fluctuations, which poses some restrictions for both, possible ion candidates as well as a maximum spatial separation where this assumption is still valid.

As a final note, one should remember that the Larmor frequencies are several orders of magnitude larger than cyclotron frequencies. Therefore, the coherence for the spin states might be subject to effects that are not related to the time-scale of the cyclotron motions of the ions. When starting to develop this method is has thus been unclear if a similar cancellation could also be achieved for the Larmor frequencies of such coupled ions and which level of coherence of the quantum states could be obtained.

5.2 An Introduction to Coupled Ions

The complete measurement scheme rests on the principle of coupling the ions as a magnetron ion crystal, with the purpose of getting the ions spatially as close as possible without designing specialized traps at micrometer scales. Even if small distances of some 10 µm can be achieved, the typical B_1 gradients are of order of $\frac{\mathrm{mT}}{\mathrm{m}}$. Therefore, even such distances would result in relative frequency shifts of order 1×10^{-8}. Thus it has to be ensured, that the ions will be placed in the identical position, or more specifically, the identical average magnetic field. This can be achieved in a magnetron crystal, where it will be possible to describe the system of coupled ions mostly by the dynamics of their respective magnetron modes while axial and modified cyclotron frequency will experi-

---

[a] This definition will make sense later on. $^{20}\mathrm{Ne}^{9+}$ will receive index 2, while $^{22}\mathrm{Ne}^{9+}$ is index 1, such that the difference frequency remains positive.

ence shifts, but can otherwise be treated as independent modes.
In this chapter I will focus on the dynamics and physics of such a coupling, deriving the related shifts and consequences for the motions of the ions. First, an understanding on how to characterize the motion and which properties have to be measured (or are accessible) to verify the state of such a coupled ion crystal will be established. Building upon this, methods to manipulate the coupled system will be derived and potential systematic effects for a Larmor frequency difference measurement will be considered. The main difference compared to the mass measurements of the *Ion Balance* [82] that has to be kept in mind while reading this, is that there is no interest in any of the motional frequencies, or specifically, the cyclotron frequency. To extract the g-factor difference, it suffices to measure the difference of Larmor frequencies, where the absolute magnetic field does only enter in a strongly relaxed manner as the required precision is suppressed by the ratio of the frequency difference to the absolute Larmor frequency. For the example of the chosen neon isotopes, this translates to more than 8 orders of magnitude suppression with respect to the absolute magnetic field. Furthermore, one should note that this scheme was initially developed to compare almost identical masses, whereas here a system of ions where the mass is roughly 10% different will be used. However, the relative difference in Larmor frequencies is in this specific case only about 7×10^{-9}.

5.3 Rabi Frequencies and Coupling

To follow this study, it is helpful to understand the general concept that will be applied throughout this chapter. The modes will always be assumed to be independent first and then examined for how strongly they influence each other. Here, an analogy to the sideband coupling or the general Rabi process is very helpful. To this end, one ion can be considered to drive the other one with the frequency of its own mode, which makes it an effective RF drive exerted on the other ion. If this *drive* frequency is far detuned from the mode it might interact with, this is the weak coupling regime where the frequency is slightly shifted, but no effective coupling takes place. This is analogous to applying a far detuned drive for a Rabi oscillation, where the effective (or generalized) Rabi frequency can be defined as $\tilde{\Omega}_R = \sqrt{\Omega_R^2 + \Delta^2}$, with the actual Rabi frequency Ω_R and the detuning Δ. While this frequency becomes very large, the exchange rate or amplitude of the modulation becomes tiny, scaling as ${}^{\Omega_R^2}/_{\tilde{\Omega}_R}$. No matter how fast the modulation becomes, if the coupling is weak there is no effective exchange between the modes – they remain uncoupled. Only in the regime where the coupling becomes strong, due to the detuning being small compared to the Rabi frequency, the modes are considered to be coupled. In terms of the ions, that means one can study the strength of the interaction, mediated by the Coulomb force compared to the frequency difference of the respective ion modes. Therefore, there is a tendency to consider the observed frequency shifts as Rabi frequencies, independent of the modes actually coupling. This is somewhat equivalent to the argument, that if they *were* coupled, the modes would decompose into two new normal modes, with a frequency difference of this Rabi frequency between them.

5.3.1 Definitions

First, a few concepts have to be introduced and definitions made, which will occur from here on to simplify the description of the motions. These loosely follow the conventions used in [84, 85]. Further, the identical charge q for both ions is assumed, saving the indices here.

The average mass m_0 is given as

$$m_0 = \frac{1}{2}(m_1 + m_2), \tag{5.1}$$

which can be used to express the imbalance of the masses with the parameter η as

$$m_1 = m_0(1+\eta) \tag{5.2}$$
$$m_2 = m_0(1-\eta). \tag{5.3}$$

For this measurement case, m_1 to chosen be the mass of $^{22}\mathrm{Ne}^{9+}$ and m_2 that of $^{20}\mathrm{Ne}^{9+}$. Further, the frequencies of a fictitious ion of the mean mass m_0 can be defined analogous to the normal frequencies in a Penning trap as

$$\omega_{c,0} = \frac{qB}{m_0} \tag{5.4}$$
$$\omega_{z,0} = \sqrt{\frac{q}{m_0}\frac{V_r C_2}{d_{\mathrm{char}}^2}} \tag{5.5}$$
$$\omega_{\pm,0} = \frac{1}{2}\left(\omega_{c,0} \pm \sqrt{\omega_{c,0}^2 - 2\omega_{z,0}^2}\right), \tag{5.6}$$

which will mostly be used to generalize and simplify the equations.

Finally, it will prove to be useful to think of the interaction strength of the coupled ions in terms the Coulomb force expressed as an interaction frequency as

$$\Omega_E = \sqrt{\frac{1}{4\pi\epsilon_0}\frac{q^2}{m_0 d_{\mathrm{sep}}^3}}, \tag{5.7}$$

with the distance between the ions d_{sep} and assuming the charge of the ions q to be identical.

5.3.2 Coupling of the Modes

As already mentioned above, the interaction of the individual modes can be qualitatively described when comparing the interaction strength, given as an effective Rabi frequency, to the frequency difference of the modes. The Rabi frequencies of the individual modes will be derived in the following pages, but it simplifies the understanding of the general idea when already comparing these frequencies to the interaction frequency before further developing this model.

For the neon isotopes $^{20}\text{Ne}^{9+}$ and $^{22}\text{Ne}^{9+}$, on a separation distance of $d_{\text{sep}} = 411\,\mu\text{m}$, which will be the distance mostly used later on, these Rabi frequencies of each mode are given as

$$\Omega_+ = \frac{\Omega_E^2}{\omega_c} = 7.5\,\text{Hz} \cdot 2\pi \tag{5.8a}$$

$$\Omega_z = \frac{\Omega_E^2}{\omega_z} = 301\,\text{Hz} \cdot 2\pi \tag{5.8b}$$

$$\Omega_- = \frac{2\Omega_E^2}{\omega_c} = 15\,\text{Hz} \cdot 2\pi. \tag{5.8c}$$

These can now be compared to the difference of the individual frequencies of the two ions. Here, the voltages are assumed to be adjusted such that $^{22}\text{Ne}^{9+}$ is tuned into resonance with the axial resonator at $\nu_z \approx 651\,\text{kHz}$. The differences in frequencies $\nu_{20\text{Ne}} - \nu_{22\text{Ne}}$ are then

$$\delta\nu_+ \approx 2.5\,\text{MHz} \gg \frac{\Omega_+}{2\pi} \tag{5.9a}$$

$$\delta\nu_z \approx 31.8\,\text{kHz} \gg \frac{\Omega_z}{2\pi} \tag{5.9b}$$

$$\delta\nu_- \approx -330\,\text{mHz} \ll \frac{\Omega_-}{2\pi} \tag{5.9c}$$

$$\delta\nu_L \approx 758\,\text{Hz}. \tag{5.9d}$$

At this point one can see, that the differences of axial and modified cyclotron frequencies are several orders of magnitude larger than the Rabi frequencies of the respective modes. Therefore, they basically remain independent of each other. However, the magnetron frequencies of the ions are almost identical as they only depend on the applied voltage to first order, their difference amounts to only $\Delta\nu_- \approx -330\,\text{mHz}$ and is significantly smaller than the magnetron Rabi frequency Ω_-. Therefore, while both axial and modified cyclotron motion will be perturbed by the presence of the respective other ion, they are not coupled to each other. For the magnetron mode however, the ions will be locked in phase relative to each other on opposite sides of the trap due to their strong interaction, resulting in a strongly coupled system in this mode only.

5.4 The Axial Frequency Shift

The first order axial frequency shift for both ions can be directly inferred when one considers the additional repelling Coulomb force the ions exert onto each other (see Appendix 8.3.1). Here, a large separation distance compared to small axial and cyclotron modes is assumed. This is valid as the magnetron separation distance will typically be of several 100 µm, while both axial and cyclotron mode will be at their thermal radii of $\hat{z} \approx 16\,\mu\text{m}$ and $\hat{r}_+ \approx 2\,\mu\text{m}$, respectively. The frequency shift $\Delta\omega_{z,i}$ for the individual ions i compared to the unperturbed system is given by

$$\begin{aligned}
\Delta\omega_{z,i} &= -\frac{1}{4\pi\epsilon_0}\frac{q^2}{2m_i d_{\text{sep}}^3\omega_{z,i}} && \text{(5.10a)}\\
&= -\frac{\Omega_E^2}{2\omega_{z,i}} && \text{(5.10b)}\\
&= -\frac{\Omega_{z,i}}{2}. && \text{(5.10c)}
\end{aligned}$$

This is instructive, showing that the axial frequency will always be shifted to lower value and that the shift scales with $\propto d_{\text{sep}}^{-3}$. The second order contribution one has to consider stems from the dynamic interaction of the ions. The ions experience the Coulomb force modulated by the axial motion of the other ion respectively, which results in an effective excitation below resonance for the higher frequency ion, and above resonance for the lower frequency ion [84]. This breaks the symmetry in the sign of this shift and one can write the individual axial frequency shifts as

$$\boxed{\begin{aligned}
\Delta\omega_{z,1} &= -\frac{\Omega_{z,1}}{2} - \frac{\Omega_z^2}{8\pi\delta\nu z}\\
\Delta\omega_{z,2} &= -\frac{\Omega_{z,2}}{2} + \frac{\Omega_z^2}{8\pi\delta\nu z}.
\end{aligned}}
\qquad \begin{aligned}&\text{(5.11a)}\\&\text{(5.11b)}\end{aligned}$$

This additional contribution is a correction of less than 0.5% to the total frequency shift and can in principle be neglected. However, these shifts yield the first crucial measurement parameter, as by comparing the shifted frequency versus that of a single cold ion, the separation distance between the ions can be immediately inferred. Therefore, the frequency of a single cold ion has to be measured for a given voltage prior to coupling the ions.

5.5 The Magnetron Motion

Due to the coupling, the magnetron mode is of largest interest here. As it is also the most complex, the dynamics will be treated more carefully. The complete system will be treated classically, as all quantum numbers are of $n_i > 100\,000$ for the respective modes. First, it will be shown that the coupled magnetron motion can be well described with the new normal modes, the separation mode, described by the parameter d_{sep} as well as a common mode motion with radius r_{com}.

5.5.1 Conservation of Energy and Angular Momentum

Here, the focus will be on the conclusions that can be drawn from conserved quantities. It is of most interest, how well the coupled system can be approximated by assuming the motion to be correctly parameterized by the constants d_{sep} and r_{com} .
As shown by Cornell et al. [85], conservation of the total canonical angular momentum as well as the conservation of energy can still be assumed in the case of two coupled ions in the trap. Here, I will follow this derivation, however it will be adapted to the present case. For now, both cyclotron and axial amplitudes are assumed to be zero, leaving only the magnetron radii, described by the vectors $\boldsymbol{\rho}_1$ and $\boldsymbol{\rho}_2$ from the trap centre to the position of the ions. One can then define the vectors

$$\boldsymbol{d}_{\mathrm{sep}} = \boldsymbol{\rho}_1 - \boldsymbol{\rho}_2 \quad \text{and} \tag{5.12a}$$

$$\boldsymbol{r}_{\mathrm{com}} = \frac{\boldsymbol{\rho}_1 + \boldsymbol{\rho}_2}{2}. \tag{5.12b}$$

Note, that the interest typically rests upon the norm of these vectors, where r_{com} is the radius of the centre of mass motion of the coupled system with respect to the trap centre, while d_{sep} is the complete separation distance between the two ions. The total canonical angular momentum[a] for two such ions can then be written as

$$L_z = \frac{qB}{2}(\boldsymbol{\rho}_1^2 + \boldsymbol{\rho}_2^2) + m_1\boldsymbol{\rho}_1 \times \dot{\boldsymbol{\rho}}_1 + m_2\boldsymbol{\rho}_2 \times \dot{\boldsymbol{\rho}}_2 \tag{5.13}$$

with the vectors $\boldsymbol{\rho}_1$ and $\boldsymbol{\rho}_2$ pointing from the trap centre to the respective ion. The total energy for the magnetron motion (using Eq. (2.7c)), including the additional potential energy of the Coulomb interaction of the two ions, is

$$E = -\frac{1}{4}m_1\omega_{z,1}^2\boldsymbol{\rho}_1^2 - \frac{1}{4}m_2\omega_{z,2}^2\boldsymbol{\rho}_2^2 + \frac{1}{2}m_1\dot{\boldsymbol{\rho}}_1{}^2 + \frac{1}{2}m_2\dot{\boldsymbol{\rho}}_2{}^2 + \frac{1}{4\pi\epsilon_0}\frac{q^2}{d_{\text{sep}}}\,. \tag{5.14}$$

While it is more elegant to write the parts of the equation related to the trapping potential in terms of axial frequency ω_z and mass, these are actually independent of the mass. Separating the terms for the individual ions and using the unperturbed magnetron velocities instead [85], one obtains

$$L_z = \boldsymbol{\rho}_1^2\left(\frac{qB}{2} - m_1\omega_{-,1}\right) + \boldsymbol{\rho}_2^2\left(\frac{qB}{2} - m_2\omega_{-,2}\right) + \epsilon_L \tag{5.15}$$

and

$$\begin{aligned} E = {} & \boldsymbol{\rho}_1^2\left(-\frac{m_1\omega_{z,1}^2}{4} + \frac{m_1\omega_{-,1}^2}{2}\right) + \boldsymbol{\rho}_2^2\left(-\frac{m_2\omega_{z,2}^2}{4} + \frac{m_2\omega_{-,2}^2}{2}\right) \\ & + \frac{1}{4\pi\epsilon_0}\frac{q^2}{d_{\text{sep}}} + \epsilon_E\,, \end{aligned} \tag{5.16}$$

with the corrections for the substitution error ϵ_E and ϵ_L. These errors can be shown to be of order $\frac{\Omega_E^2}{\omega_{c,0}^2}$ and $\frac{\omega_{2,0}^2}{\omega_{c,0}^2}$ [85] and can therefore be neglected. Furthermore, the magnetron frequencies are assumed to be identical, treating them as $\omega_{-,0}$. Then, the definition of m_1, m_2 and the mass imbalance η is applied which yields

$$E = (\boldsymbol{\rho}_1^2 + \boldsymbol{\rho}_2^2)\left[-\frac{m_0\omega_{z,0}^2}{4} + \frac{m_0\omega_{-,0}^2}{2}\right] + (\boldsymbol{\rho}_1^2 - \boldsymbol{\rho}_2^2)\left[\frac{\eta m_0\omega_{-,0}^2}{2}\right] + \frac{1}{4\pi\epsilon_0}\frac{q^2}{d_{\text{sep}}}. \tag{5.17}$$

The canonical angular momentum is treated similarly resulting in

$$L_z = (\boldsymbol{\rho}_1^2 + \boldsymbol{\rho}_2^2)\left[\frac{qB}{2} - m_0\omega_{-,0}\right] + (\boldsymbol{\rho}_1^2 - \boldsymbol{\rho}_2^2)\left(-\eta m_0\omega_{-,0}\right). \tag{5.18}$$

---

[a] This uses the Lagrangian generalized momentum, adding the dependency on the magnetic field, instead of only the kinetic momentum, see Appendix A.1 in [43]

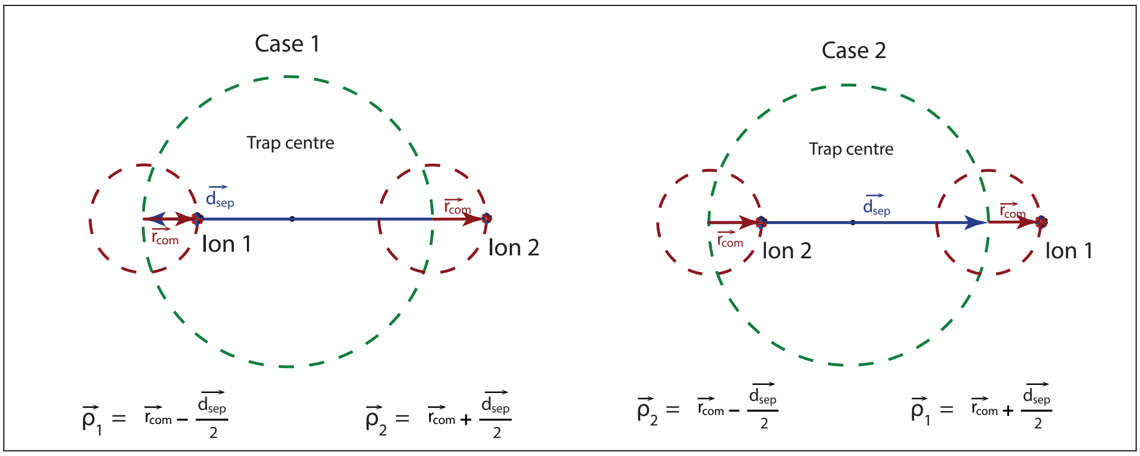

Figure 5.1: Here, the change in position of the two ions is shown to illustrate the maximum possible change of the quantity $\boldsymbol{\rho}_1^2 - \boldsymbol{\rho}_2^2$.

The critical argument is now to allow the individual radii $\boldsymbol{\rho}_1$ and $\boldsymbol{\rho}_2$ to evolve with time, but noting that the changes in $\boldsymbol{\rho}_1^2 + \boldsymbol{\rho}_2^2$ and $\boldsymbol{\rho}_1^2 - \boldsymbol{\rho}_2^2$ must be related due to the required conservation of both, energy and angular momentum. From Eq. (5.18) it can therefore be derived that

$$\delta(\boldsymbol{\rho}_1^2 + \boldsymbol{\rho}_2^2) = \delta(\boldsymbol{\rho}_1^2 - \boldsymbol{\rho}_2^2)\frac{2\eta\omega_{-,0}}{\omega_{c,0} - 2\omega_{-,0}}. \tag{5.19}$$

Similarly, the conservation of energy leads to

$$\delta\left(\frac{q^2}{4\pi\epsilon_0 m_0 d_{\mathrm{sep}}}\right) = \delta(\boldsymbol{\rho}_1^2 + \boldsymbol{\rho}_2^2)\left[\frac{\omega_{z,0}^2}{4} - \frac{\omega_{-,0}^2}{2}\right] - \delta(\boldsymbol{\rho}_1^2 - \boldsymbol{\rho}_2^2)\left(\frac{\eta\omega_{-,0}^2}{2}\right), \tag{5.20}$$

after dividing by mass m_0. When now inserting Eq. (5.19), this yields

$$\delta\left(\frac{q^2}{4\pi\epsilon_0 m_0 d_{\mathrm{sep}}}\right) = \delta(\boldsymbol{\rho}_1^2 - \boldsymbol{\rho}_2^2)\left[\frac{2\eta\omega_{-,0}}{\omega_{c,0} - 2\omega_{-,0}}\left(\frac{\omega_{z,0}^2}{4} - \frac{\omega_{-,0}^2}{2}\right) - \frac{\eta\omega_{-,0}^2}{2}\right]. \tag{5.21}$$

When applying the approximations of $\omega_{c,0} \gg \omega_{-,0}$ as well as $\omega_{z,0}^2 \approx 2\omega_{-,0}\omega_{c,0}$, this results in

$$\delta\left(\frac{q^2}{4\pi\epsilon_0 m_0 d_{\mathrm{sep}}}\right) = \delta(\boldsymbol{\rho}_1^2 - \boldsymbol{\rho}_2^2)\frac{\eta\omega_{-,0}^2}{2}. \tag{5.22}$$

The maximum length for each of these vectors is reached, when $\boldsymbol{\rho}_i = {}^{\boldsymbol{d}_{\mathrm{sep}}}/_2 \pm \boldsymbol{r}_{\mathrm{com}}$, added linearly. The maximum possible change of $\boldsymbol{\rho}_1^2 - \boldsymbol{\rho}_2^2$ is therefore related to the common mode radius and limited to $\delta(\boldsymbol{\rho}_1^2 - \boldsymbol{\rho}_2^2)_{\mathrm{max}} = 4d_{\mathrm{sep}}r_{\mathrm{com}}$ when the ions change positions. This is illustrated in Fig. 5.1.

As will be shown later on (see section 6.2.4), the common mode radii can be verified to be $r_{\mathrm{com}} \leq 100\,\mu\mathrm{m}$, or to simplify, $r_{\mathrm{com}} \lesssim d_{\mathrm{sep}}/4$, after preparing the ions. When additionally using the ion interaction frequency from Eq. (5.7), as well as the relation $\delta\frac{1}{d_{\text{sep}}} = -\frac{1}{d_{\text{sep}}^2}\delta d_{\text{sep}}$ the relative change for the separation distance is limited to

$$\left|\frac{\delta d_{\text{sep}}}{d_{\text{sep}}}\right| \leq \frac{\eta\omega_{-,0}^2}{2\Omega_E^2}, \tag{5.23}$$

which becomes zero when there is no common mode or for equal masses. The additional factor of 2 (compared to [84, 85]) stems from the stronger restriction for the magnitude of common mode radius. For this measurement case, where the ions are prepared with $d_{\text{sep}} \approx 400\,\mu\text{m}$, this yields a maximum possible change of $\left|\frac{\delta d_{\text{sep}}}{d_{\text{sep}}}\right| = 0.008$.
This restriction allows us to assume the separation distance to be a constant of the motion, which makes the treatment as a static system possible and allowing for a much simpler derivation of the further dynamics of the system. Furthermore, due to the conservation laws, a constant separation distance directly implicates that the common mode has to remain constant as well.

5.5.2 Cyclotron Frequency Shift

The measurement of the Larmor frequency difference will to a large extend be independent of the actual cyclotron frequencies of the ions. Therefore, it suffices to only examine these shifts to first order. To this end, the interaction is first treated as a monopole shift, assuming a stationary guiding centre and the separation d_{sep}. The system has already been treated similarly to determine the resulting force experienced by the other ion to derive the axial frequency shift (see appendix 8.3.1). As the standard EOM of a single trapped particle is still valid, albeit with a now shifted axial frequency, this can be written in terms of modified axial frequency $\omega_{z,0}^2$. Further, the radial mode vector $\boldsymbol{\rho}$, given as

$$\boldsymbol{\rho} = \begin{pmatrix} x \\ y \end{pmatrix} \tag{5.24}$$

is now expressed using the function $u(t) = x(t) + iy(t)$. This yields the expression for the modified motion with the inclusion of Coulomb repulsion as

$$\begin{aligned} \ddot{u}_{\text{c},0} &= -i\omega_{\text{c},0}\dot{u}_{\text{c}} + \frac{1}{2}\left(\omega_{z,0} - \frac{\Omega_E^2}{2\omega_{z,i}}\right)^2 && (5.25) \\ &= -i\omega_{\text{c},0}\dot{u}_{\text{c}} + \frac{1}{2}\tilde{\omega}_{z,0}^2. && (5.26) \end{aligned}$$

Interestingly, it can be shown that combining the thus shifted frequencies in the invariance theorem (Eq. (2.6)) the shift completely cancels for the first order contributions.

Furthermore, one can show that tuning the ion back to its original axial frequency by changing the applied trap voltage, this also changes the modified cyclotron frequency mostly back to the original value. To express the actual shift of the modified cyclotron frequency in the coupled system when the trap voltage is not adjusted to account for the axial frequency shift, this can be written as

$$\boxed{\begin{aligned} \Delta\omega_+ &= \frac{\Omega_E^2}{2\omega_{c,0}^2} && (5.27a) \\ &= \frac{\Omega_c}{2}, && (5.27b) \end{aligned}}$$

where Ω_c can be interpreted as the Rabi frequency[a] of the modified cyclotron mode and amounts to about $\Delta\nu_+ \approx 3.5\,\text{Hz}$.

The next order, or first mass dependent shift is only a small correction, yielding [84]

$$\Delta\omega_+ = \frac{\Omega_c}{2}\left(1 + \frac{\omega_{z,0}^2}{\omega_{c,0}^2}\right), \tag{5.28}$$

which amounts to about 2 mHz in the case discussed here. If one wants to investigate ratios or differences of the cyclotron frequencies, the shift is even further suppressed since both frequencies are shifted almost identically, therefore still allowing for a precise comparison.

5.5.3 Equations of Motion

The EOMs for the radial direction can be considered similarly as those of a single ion by adding the additional Coulomb repulsion. They can then be written as

$$m_1\ddot{\boldsymbol{\rho}}_1 = q_1 B_0 \dot{\boldsymbol{\rho}}_1 \times \hat{z} + \frac{1}{2} m_1 \omega_{z,1}^2 \boldsymbol{\rho}_1 + \frac{q^2(\boldsymbol{\rho}_1 - \boldsymbol{\rho}_2)}{4\pi\epsilon_0 d_{\text{sep}}^3} \quad \text{and} \tag{5.29a}$$

$$m_2\ddot{\boldsymbol{\rho}}_2 = q_2 B_0 \dot{\boldsymbol{\rho}}_2 \times \hat{z} + \frac{1}{2} m_2 \omega_{z,2}^2 \boldsymbol{\rho}_2 - \frac{q^2(\boldsymbol{\rho}_1 - \boldsymbol{\rho}_2)}{4\pi\epsilon_0 d_{\text{sep}}^3}. \tag{5.29b}$$

Using the definitions of d_{sep} and r_{com} and assuming the masses to be equal ($m_0 = m_1 = m_2$) for now (which also means all frequencies would be identical), the difference of Eq.

---

[a] This is an analogy if the modes were coupled: if the cyclotron frequencies difference would be smaller than this Rabi frequency, one would also observe a frequency splitting there. However, as this frequency is much smaller than the difference between the cyclotron frequencies, one only observes a constant frequency shift.

(5.29a) and (5.29b) yields

$$\ddot{\boldsymbol{d}}_{\text{sep}} = \omega_{c,0}\dot{\boldsymbol{d}}_{\text{sep}} \times \hat{z} + \left[\frac{1}{2}\omega_{z,0}^2 + 2\Omega_E^2\right]\boldsymbol{d}_{\text{sep}}, \tag{5.30}$$

while the sum gives the equation for the common mode as

$$\ddot{\boldsymbol{r}}_{\text{com}} = \omega_{c,0}\dot{\boldsymbol{r}}_{\text{com}} \times \hat{z} + \frac{1}{2}\omega_{z,0}^2\boldsymbol{r}_{\text{com}}. \tag{5.31}$$

Even though only the specific case of equal masses is considered here, the decomposition of the coupled magnetron motion into a separation and common mode motion can be nicely observed here and will only be slightly adjusted for the case of different masses. Interestingly, the common mode frequency is identical to the frequency of a single unperturbed particle with mass m_0, while the separation mode is slightly faster, scaling with the interaction strength between the ions. This holds true as long as the interaction can be described by neglecting axial and cyclotron amplitudes, with the effective distance between the ions mostly given by d_{sep}. The coupled system with these new modes is illustrated in Fig. 5.2.
The frequency difference between these modes will lead to a modulation of the effective magnetron radius, or the actual distance to the trap centre, of each ion. This will become important when the magnitude of each mode via a detuning of the trap is measured, similarly to the TR scan described in section 4.2.5. Here, the axial frequency will be made dependent on the magnetron radius by introducing a C_4 contribution. As the effective magnetron radius is now modulated, this in turn leads to a frequency modulation of the axial signal with this frequency difference between separation and common mode, with the modulation index depending on the ratio of separation to common mode radius. If such a modulation can be observed, a rough estimate for the size of the common mode as well as the absolute value of the separation distance can be deduced. While this is not of similar resolution as the observed axial shift introduced in Eq. (5.10c), it provides an additional parameter to confirm our understanding of the coupled system.

Finally, the difference between the frequencies of these new normal modes $\Omega_- = \omega_{-,s} - \omega_{-,c}$ can be deduced, when considering the faster separation mode to be the required speed-up of the common mode to compensate for the additional electric field of the second ion [84]. As the Lorentz force is already cancelled by the common mode motion, one of the ions can be considered moving on a circle, where the radius is half the separation distance $\rho_{\text{sep}}/2$, and the frequency is Ω_-. The equation of motion (EOM),

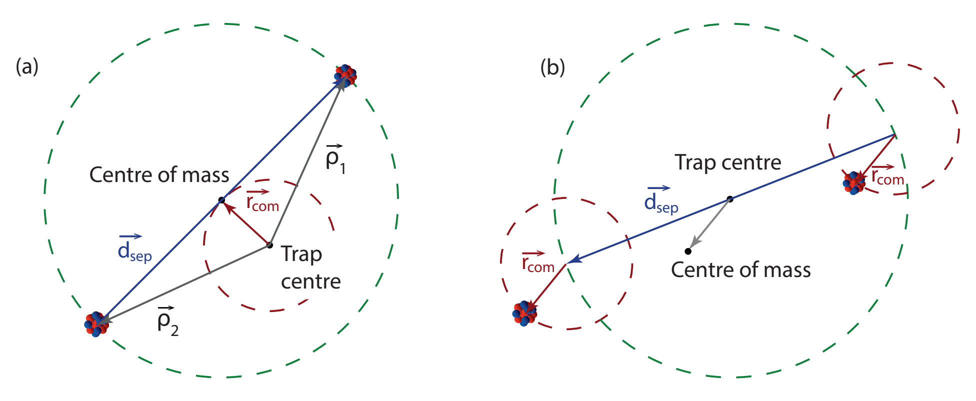

Figure 5.2: The coupled magnetron motion of the two ions. Both figures show the same model, however (a) shows the motion as the separation mode of the ions and their centre of mass motion as the common mode. (b) shows the vectors to the position of the individual ions, where they both perform a coherent separation and common motion. This leads to an effective centre of mass motion around the trap centre with the common mode. As the frequencies differ slightly by Ω_-(see text), the effective magnetron radius of each ion is modulated with this difference frequency when a common mode radius is present.

adapted from Eq. (5.30) can then be written as

$$-\Omega_-^2 \frac{\boldsymbol{d}_{\text{sep}}}{2} = -\Omega_- \omega_{c,0} \frac{\boldsymbol{d}_{\text{sep}}}{2} + \Omega_E^2 \boldsymbol{d}_{\text{sep}}. \tag{5.32}$$

In this frame, rotational frequency is slow and the contribution of the centrifugal force on the left hand side can be neglected. This then yields

$$\boxed{\Omega_- = \frac{2\Omega_E^2}{\omega_{c,0}}}. \tag{5.33}$$

This difference can also be derived by studying the separation motion as given in Eq. (5.30). With the definition of the shifted axial frequency $\tilde{\omega}_z^2 = \omega_z^2 + 4\Omega_E^2$, the frequency of the separation mode $\omega_{-,s}$ can be directly given analogous to the magnetron frequency of a single ion (see Eq. (2.5)) as

$$\omega_{-,s} = \frac{\omega_{c,0}}{2} - \frac{1}{2}\sqrt{\left(\omega_{c,0}^2 - 2\omega_{z,0} - 8\Omega_E^2\right)}. \tag{5.34}$$

Using the approximations of $\omega_{c,0} \gg \omega_{z,0}$ and $\omega_{c,0}^2 \gg \Omega_E^2$, this can be written as

$$\omega_{-,s} = \frac{\omega_{c,0}}{2} - \frac{1}{2}\sqrt{\left(\omega_{c,0}^2 - 2\omega_{z,0}\right)}\left(1 + \frac{4\Omega_E^2}{\omega_{c,0}^2}\right) \tag{5.35a}$$

$$= \omega_{-,c} + \frac{2\Omega_E^2}{\omega_{c,0}} \tag{5.35b}$$

$$\Rightarrow \Omega_- = \frac{2\Omega_E^2}{\omega_{c,0}}, \tag{5.35c}$$

yielding the same result with the common mode frequency given by the centre of mass motion for the mean mass. The separation mode frequency is again found to be larger than the common mode frequency by the beat frequency Ω_-.

For the neon ions, with a typical separation distance of $d_{\text{sep}} \approx 400\,\mu\text{m}$, the frequency difference amounts to $\Omega_- \approx 2\pi \cdot 15\,\text{Hz}$. This leads to multiple *swapping cycles*, changing which of the ions is closer to the trap centre or further away, for our typical measurement times of several 100 ms up to 2.2 s. The swapping is helpful to ensure that both ions experience identical magnetic fields on average. Even if a common mode is present, magnetic field differences due to a radial gradient of the field will be averaged over as the ions change their position relative to the trap centre several times even during the shortest measurement times. Additionally, both phase and magnitude of the common mode will be different for of each measurement cycle[a], leading to an averaging over multiple measurement cycles.

5.5.4 Ions of Different Mass

When looking at a system with ions of different masses, these equations do not decompose as nicely into fully independent modes as shown before. Instead, equation (5.3) can be used to achieve an expression in terms of their mass difference η after dividing the sum and difference of Eq. (5.29a) and Eq. (5.29b) by the mean mass m_0 as

$$\ddot{\boldsymbol{d}}_{\text{sep}} = \omega_{c,0}\dot{\boldsymbol{d}}_{\text{sep}} \times \hat{z} + \left[\frac{1}{2}\omega_{z,0}^2 + 2\Omega_E^2\right]\boldsymbol{d}_{\text{sep}} - 2\eta\ddot{\boldsymbol{r}}_{\text{com}} \tag{5.36a}$$

$$\ddot{\boldsymbol{r}}_{\text{com}} = \omega_{c,0}\dot{\boldsymbol{r}}_{\text{com}} \times \hat{z} + \frac{1}{2}\omega_{z,0}^2\boldsymbol{r}_{\text{com}} - \frac{\eta}{2}\ddot{\boldsymbol{d}}_{\text{sep}}. \tag{5.36b}$$

---

[a] The ions are at the same relative position to each other, but we do not have control over their absolute magnetron phases and the common mode is cooled but cannot be ensured to be zero or identical each cycle.

The additional terms $2\eta\ddot{\boldsymbol{r}}_{\text{com}}$ and $\frac{\eta}{2}\ddot{\boldsymbol{d}}_{\text{sep}}$ are of order $\eta\omega_{m,0}^2$ and therefore small[a] compared to the other terms. Furthermore, since the frequencies of separation and common mode are different, the interaction between them is non-resonant, only inducing a small driven oscillation. Thus, the respective influence of the modes can be treated as a small perturbation to the normal mode system, where only the first order effect has to be considered. Effectively, only the direct action on each motion of zeroth order of the other is considered to derive the first order solution.

To put it simply, the influence of the separation motion due to the common mode motion is considered, as well as vice versa. However, the back-action of the modified separation motion back onto the common mode is neglected, as well as the other way around.

When again using the substitution $u(t) = x(t) + iy(t)$ for the representation of the radial vectors $\boldsymbol{d}_{\text{sep}}$ and $\boldsymbol{r}_{\text{com}}$ in the x-y-plane and $\ddot{u}_{\text{com}} = -\omega_{-,c}^2 u_{\text{com}}$, as well as $\ddot{u}_{\text{sep}} = -\omega_{-,s}^2 u_{\text{sep}}$ this can be written as

$$\ddot{u}_{\text{sep}}^{(1)} = -i\omega_{c,0}\dot{u}_{\text{sep}}^{(1)} + \left[\frac{1}{2}\omega_{z,0}^2 + 2\Omega_E^2\right] u_{\text{sep}}^{(1)} + 2\eta\omega_{-,c}^2 u_{\text{com}}^{(0)} \tag{5.37a}$$

$$\ddot{u}_{\text{com}}^{(1)} = -i\omega_{c,0}\dot{u}_{\text{com}}^{(1)} + \frac{1}{2}\omega_{z,0}^2 u_{\text{com}}^{(1)} + \frac{\eta\omega_{-,s}^2}{2} u_{\text{sep}}^{(0)}, \tag{5.37b}$$

with the common mode frequency $\omega_{-,c}$ and the separation mode frequency $\omega_{-,s}$. This assumes the solution without an interaction of the modes to be $u_{\text{sep}}^{(0)}$ and $u_{\text{com}}^{(0)}$, respectively. The terms denoted with the superscript (1) correspond to the first order solution with the modes non-resonantly action upon each other. The actual EOM can then be written as the linear combination of these solutions.

To derive the individual modes, under assumption that only the first order effects have to be considered, $u_{\text{sep}}^{(0)} = \tilde{d}_{\text{sep}} e^{-i\omega_{-,s}t}$ and $u_{\text{sep}}^{(1)} = \tilde{a}_{\text{sep}}^* e^{-i\omega_{-,c}t}$ are used, where $\tilde{a}_{\text{sep}}^*$ is the amplitude dependent on $\tilde{r}_{\text{com}}$.

Similarly, for the common mode the equations $u_{\text{com}}^{(0)} = \tilde{r}_{\text{com}} e^{-i\omega_{-,c}t}$ and $u_{\text{com}}^{(1)} = \tilde{a}_{\text{com}}^* e^{-i\omega_{-,s}t}$ can be defined. The tilde notation indicates the vector to be complex, which simplifies the equation by eliminating the need of additional phases in the exponents. For the

---

[a] smaller by about 5 orders of magnitude, actually

separation mode this yields

$$
\begin{aligned}
-\omega_{-,c}^2\tilde{a}_{\mathrm{sep}}^* &= -i\omega_{c,0}\left(-i\omega_{-,c}\right)\tilde{a}_{\mathrm{sep}}^* + \frac{1}{2}\omega_{z,0}^2\left(1+\frac{4\Omega_E^2}{\omega_{z,0}^2}\right)\tilde{a}_{\mathrm{sep}}^* + 2\eta\omega_{-,c}^2\tilde{r}_{\mathrm{com}} && (5.38\mathrm{a})\\
\left[-\omega_{-,c}^2 + \omega_{c,0}\omega_{-,c} - \frac{1}{2}\omega_{z,0}^2 - 2\Omega_E^2\right]\tilde{a}_{\mathrm{sep}}^* &= 2\eta\omega_{-,c}^2\tilde{r}_{\mathrm{com}} && (5.38\mathrm{b})\\
\left[-\omega_{-,c}^2 + \left(\omega_{+,0}+\omega_{-,c}\right)\omega_{-,c} - \frac{1}{2}\omega_{z,0}^2 - 2\Omega_E^2\right]\tilde{a}_{\mathrm{sep}}^* &= 2\eta\omega_{-,c}^2\tilde{r}_{\mathrm{com}} && (5.38\mathrm{c})\\
\left[-2\Omega_E^2\right]\tilde{a}_{\mathrm{sep}}^* &= 2\eta\omega_{-,c}^2\tilde{r}_{\mathrm{com}} && (5.38\mathrm{d})\\
\Rightarrow \tilde{a}_{\mathrm{sep}}^* &= -\frac{\eta\omega_{-,c}^2}{\Omega_E^2}\tilde{r}_{\mathrm{com}} && (5.38\mathrm{e})
\end{aligned}
$$

after dividing by $e^{-i\omega_{-,c}t}$ and using $\omega_c = \omega_+ + \omega_{-,c}$ as well as $\omega_+\omega_{-,c} = {}^1\!/_2\,\omega_{z,0}^2$. Similarly, the amplitude $\tilde{a}_{\mathrm{com}}^*$ can be derived for the common mode as

$$
\tilde{a}_{\mathrm{com}}^* = +\frac{\eta\omega_{-,s}^2}{4\Omega_E^2}\tilde{d}_{\mathrm{sep}}\,, \tag{5.39}
$$

when neglecting the two terms of Ω_-^2 and $\Omega_-\omega_{-,s}$ compared to the much larger $\Omega_-\omega_{+,0}$. Finally, one applies that $\Omega_-\omega_+ \approx 2\Omega_E^2$ as one finds from Eq. (5.33). From here, the actual EOMs can be written as

$$
\begin{aligned}
u_s(t) &= e^{-i\omega_{-,s}t}\left[\tilde{d}_{\mathrm{sep}} - 2\delta_{\mathrm{mag}}\tilde{r}_{\mathrm{com}}e^{i\Omega_- t}\right] && (5.40\mathrm{a})\\
u_c(t) &= e^{-i\omega_{-,c}t}\left[\tilde{r}_{\mathrm{com}} + \frac{1}{2}\delta_{\mathrm{mag}}\tilde{d}_{\mathrm{sep}}e^{-i\Omega_- t}\right], && (5.40\mathrm{b})
\end{aligned}
$$

where

$$
\boxed{\delta_{\mathrm{mag}} = \frac{\eta\omega_{-,0}^2}{2\Omega_E^2}} \tag{5.41}
$$

has been chosen and will be put into more context shortly. The EOM for each individual ion can now be rewritten in terms of the common and separation mode, following their definition of Eq. (5.12b) as

$$
\begin{aligned}
u_1(t) &= u_c(t) + \frac{1}{2}u_s(t)\\
&= \tilde{r}_{\mathrm{com}}\left(1-\delta_{\mathrm{mag}}\right)e^{-i\omega_{-,c}t} + \frac{1}{2}\tilde{d}_{\mathrm{sep}}\left(1+\delta_{\mathrm{mag}}\right)e^{-i\omega_{-,s}t}
\end{aligned} \tag{5.42}
$$

and

$$\begin{aligned} u_2(t) &= u_c(t) - \frac{1}{2}u_s(t) \\ &= \tilde{r}_{\mathrm{com}}\left(1+\delta_{\mathrm{mag}}\right)e^{-i\omega_{-,c}t} - \frac{1}{2}\tilde{d}_{\mathrm{sep}}\left(1-\delta_{\mathrm{mag}}\right)e^{-i\omega_{-,s}t}. \end{aligned} \tag{5.43}$$

This is especially instructive when considering the special case $\tilde{r}_{\mathrm{com}} = 0$, where the motion is fully defined by the separation mode[a]. Then, the heavier ion will be on a slightly larger, the lighter ion on a smaller orbit due to their difference in centrifugal force. This imbalance is given by the parameter δ_{mag}. In the case of the neon isotopes $^{20}\mathrm{Ne}^{9+}$ and $^{22}\mathrm{Ne}^{9+}$ for a nominal separation distance of $\tilde{d}_{\mathrm{sep}} = 411\,\mu\mathrm{m}$ where $\delta_{\mathrm{mag}} = 8.6 \times 10^{-3}$, the asymmetry of the modes is $\boldsymbol{\rho_1} - \boldsymbol{\rho_2} \approx 3.5\,\mu\mathrm{m}$. The validity of this approach has been verified by Thompson [84] by performing a more rigorous analytical approach as well as numerical simulations, that have been verified . The result will prove to be crucial as this imbalance of radii yields the dominant (and the only relevant) systematic shift and uncertainty for the difference measurement of two Larmor frequencies, which will be shown momentarily.

5.6 Axial Equilibrium Position

While it has been shown that the ions are only coupled in their magnetron mode, it is essential to examine the common equilibrium position of the axial motion. With our $B_1 = 2.648(24)\,\frac{\mathrm{mT}}{\mathrm{m}}$ even a tiny asymmetry would result in large relative frequency shifts. To this end, the potential energy of the system can be studied to determine the global minimum with respect to the axial equilibrium positions of the ions, under the assumption of a constant separation distance. The combined axial potential energy of the ions can be written as

$$W_{\mathrm{pot}} = \frac{V_r C_2}{2d_{\mathrm{char}}^2} q\left(z_1^2 + z_2^2\right) + \frac{q^2}{4\pi\epsilon_0}\frac{1}{\sqrt{d_{\mathrm{sep}}^2 + \Delta z^2}}, \tag{5.44}$$

where $\Delta z = z_1 - z_2$ is the difference between the axial position of the ions. These terms are simply the potential energy due to the position of the ions, as well as the Coulomb potential energy from their respective repulsion. Using $z_1^2 + z_2^2 = (\Delta z)^2 + 2z_1 z_2$ and the

---

[a] This is the ideal case we strive for.

definition of ω_z, the individual minima of the potential energy are given as

$$\frac{\partial W_{\text{pot}}}{\partial z_1} = \frac{V_r C_2 q}{d_{\text{char}}^2} z_1 - \frac{q^2}{4\pi\epsilon_0} \frac{\Delta z}{\left(d_{\text{sep}}^2 + \Delta z^2\right)^{3/2}} \overset{!}{=} 0 \quad \text{and} \tag{5.45a}$$

$$\frac{\partial W_{\text{pot}}}{\partial z_2} = \frac{V_r C_2 q}{d_{\text{char}}^2} z_2 + \frac{q^2}{4\pi\epsilon_0} \frac{\Delta z}{\left(d_{\text{sep}}^2 + \Delta z^2\right)^{3/2}} \overset{!}{=} 0. \tag{5.45b}$$

For the total minimum of the potential energy $\frac{\partial W_{\text{pot}}}{\partial z_1} = \frac{\partial W_{\text{pot}}}{\partial z_2} = 0$ has to be valid. Therefore, it follows that

$$\frac{\partial W_{\text{pot}}}{\partial z_1} + \frac{\partial W_{\text{pot}}}{\partial z_2} = \frac{V_r C_2 q}{d_{\text{char}}^2} (z_1 + z_2) \overset{!}{=} 0 \tag{5.46a}$$

$$\Rightarrow z_1 = -z_2 \qquad \text{and} \tag{5.46b}$$

$$\frac{\partial W_{\text{pot}}}{\partial z_1} - \frac{\partial W_{\text{pot}}}{\partial z_2} = \frac{V_r C_2 q}{d_{\text{char}}^2} (z_1 - z_2) - \frac{2q^2}{4\pi\epsilon_0} \frac{\Delta z}{\left(d_{\text{sep}}^2 + \Delta z^2\right)^{3/2}} \overset{!}{=} 0 \tag{5.46c}$$

$$\Rightarrow \Delta z = 0 \quad \text{or} \tag{5.46d}$$

$$(\Delta z)^2 = \left(\frac{2q^2}{4\pi\epsilon_0 m\omega_z^2}\right)^{\frac{2}{3}} - d_{\text{sep}}^2 \tag{5.46e}$$

where the definition of the axial frequency is applied. This result can then be further simplified by using the definitions of Ω_E (5.7) and the axial Rabi frequency Ω_z (5.8c), yielding

$$\Delta z = \pm d_{\text{sep}} \sqrt{\left(\frac{2\Omega_E^2}{\omega_z^2}\right)^{\frac{2}{3}} - 1} \tag{5.47a}$$

$$= \pm d_{\text{sep}} \sqrt{\left(\frac{2\Omega_z}{\omega_z}\right)^{\frac{2}{3}} - 1}. \tag{5.47b}$$

As the axial Rabi frequency Ω_z is significantly smaller than the axial frequency ω_z[a] for all used parameters, any solution for differences in Δz remains imaginary and the only physical solution is when $\Delta z = 0$. Combined with the other condition, $z_1 = -z_2$, this restricts the axial motion to be symmetric about a z position in the same horizontal plane. Furthermore, this is only fulfilled for both individual positional shifts $z = 0$.

Additionally, the critical separation distance can be estimated below which also other minima are allowed. This is reached when $\left(\frac{2\Omega_z}{\omega_z}\right)^{\frac{2}{3}} \geq 0$, which can be expressed in terms

---

[a] By more than three orders of magnitude.

of d_{sep} as

$$d_{\text{sep,crit}} \leq \sqrt[3]{\frac{q^2}{2\pi\epsilon_0 m\omega_z^2}} \tag{5.48a}$$

$$\leq 40\,\mu\text{m} \tag{5.48b}$$

This marks the critical distance below which a transition from a magnetron crystal to an axial crystal occurs when it becomes energetically favourable. However, this estimation is based upon neglected axial amplitudes. While this is fine for large separation distances, this approximation is no longer valid when approaching the critical distance and the dependency of $\Omega_E^2(\hat{z})$ has to be considered. The result is still instructive to describe the general behaviour and, more importantly, to show that the ions move about the same axial equilibrium position when $\hat{z} \ll d_{\text{sep}}$.

5.7 Systematic Effects due to Magnetron Imbalance

The purpose of coupling two ions is to measure the difference of Larmor frequencies directly. Compared to measuring masses or their ratios, which are extracted by determining the motional frequencies of the ion and therefore inherently depend on all sorts of disturbances to the motion, the Larmor frequency depends only on the magnetic field. All interactions between the ions are thus only relevant if they induce a breaking of the symmetry, thus changing the effective magnetic field each ion experiences. There are two dominating shifts to consider here. The first is a radial B_2 gradient combined with the magnetron imbalance δ_{mag}. The second is the effect of a C_3, resulting in a magnetron radius dependent axial equilibrium position shift (see (2.19)), which combined with an axial B_1 gradient, may change the effective magnetic field. Before diving into the rigorous calculation, the rough size of these effects are estimated first.

The B_2 contribution, as defined in Eq. (2.20) has been measured to be $B_2 = 64.3(32)\,\frac{\text{mT}}{\text{m}^2}$ [18] in the centre of the PT. This would, with the aforementioned parameters of the motion (and specifically no common mode) result in a relative shift of

$$\begin{aligned}\frac{\Delta\nu_{L,2} - \Delta\nu_{L,1}}{\tilde{\nu}_L} &= \frac{B_2}{2B_0}\left(\rho_2^2 - \rho_1^2\right) \\ &= -1\times 10^{-11},\end{aligned} \tag{5.49}$$

where $\rho_1 = (1+\delta_{\text{mag}})\frac{d_{\text{sep}}}{2}$ and $\rho_2 = (1-\delta_{\text{mag}})\frac{d_{\text{sep}}}{2}$, and $\tilde{\nu}_L$ is the mean Larmor frequency. Similarly, one has to consider the C_3 positional shift, though it is significantly more complicated to measure or predict the absolute size of this contribution. Nominally, only symmetric voltages are applied and any C_3 would only be given by imperfections of the trap assembly, asymmetric voltage offsets or patch potentials. However, to tackle the already sizeable shift due to B_2, I have opted to try to improve upon this by shifting the electrostatic equilibrium position[a] to achieve a more favourable B_2. This is possible as the main source of the B_2 in the PT still stems from the ferromagnetic ring of the AT. In the (successful!) attempt to reduce this effect, a compensation ring was introduced [49], meant to counteract the B_2 in the centre of the PT. The size and position was calculated in COMSOL and, with the measured B_2 being small, seems to be working rather well. The B_3 contribution to the magnetic field, resulting from this assembly, generates a local $B_2 \approx 0$ about 1 mm shifted from the nominal centre of the PT towards the CT (see section 6.3.1). To exploit this, an asymmetric tuning ratio[b] has been used to shift the ion position into the position of the zero crossing of B_2. This comes however at the cost of the odd contributions to the electrostatic potential becoming sizeable, which necessitates the investigation of the B_1C_3 shift (see Eq. (2.23)) as well as the differential axial shift due to C_3 (see Eq. (2.15)).

Generally, the simulation of the electrostatic potential is found to be correct to better than an absolute $\pm 1 \times 10^{-3}$, as observed from the comparison of the prediction and the measured optimal tuning ratio. Assuming similar behaviour for the potential simulation in the shifted position, approximate values for C_3 can be calculated. Additionally, shifts of the axial frequency after excitations of both, magnetron and cyclotron radii are measured. This will become even more crucial when discussing the systematic effects in depth soon, which will allow to set constraints on the combinations of electrostatic and magnetic inhomogeneities. It is however hard to assign absolute values to the magnetic inhomogeneities. This is mainly due to the identical scaling of many effects with excitation radii which, in principle, would allow for a cancellation of shifts despite large imperfections. For a $C_3 \approx 2(2) \times 10^{-3}$, derived from the simulation of the electric field and a $B_1 = 2.648(24)\,\frac{\mathrm{mT}}{\mathrm{m}}$ [18], this would translate into shifts of the Larmor frequencies by means of differences in the respective axial position shift Δz_0 as

$$\begin{aligned}\frac{\Delta\nu_{L,2} - \Delta\nu_{L,1}}{\tilde{\nu}_L} &= \Delta(z_{0,2} - z_{0,1})B_1 = \frac{3}{4}\frac{C_3}{C_2 d_{\mathrm{char}}}\left(\rho_2^2 - \rho_1^2\right)B_1 \\ &\approx -3 \times 10^{-13}.\end{aligned} \tag{5.50}$$

---

[a] Note, this effects both ions in an identical fashion

[b] This is a fancy way of stating that asymmetric voltages are used to shift the electrostatic centre of the trap while trying to keep the potential harmonic

The B_2 at the shifted position (about 1 mm towards the CT) has been significantly reduced compared to the centre of the PT, however as the related shifts that are measured with single ions are ranging into the 10 mHz regime, only upper limits can be given. The thus observed shifts, combined with the limits of the simulation placed on C_3 were able to set an upper limit of $B_2 \leq 8\,\frac{\mathrm{mT}}{\mathrm{m}^2}$ (see section 6.3.1), which already reduces the maximum relative shift of the Larmor frequency into the 10^{-13} regime.

5.7.1 Combined Systematic Analysis

There is, however, a more thorough treatment of all these correlated effects possible. When considering the combined shifts of the individual Larmor frequencies and their impact on the measured difference frequency, it can be shown this difference becomes independent of the individual contributions. More importantly, when the trap would be tuned such that the axial frequency is invariant with respect to the excitation of both, cyclotron and magnetron radii, the measured Larmor frequency difference too becomes invariant to effects of C_3, C_4, B_1 and B_2 (see Appendix B).

As a change of the B_2 contribution can only be achieved by altering the tuning ratio and thus the electrostatic minimum, each such change requires the optimization of the new tuning ratio. Therefore, the process of tuning tiny residual shifts quickly becomes tiresome and iterative work. Furthermore, the B_1 contribution cannot be tuned at all with the current setup. It is thus not possible to fully eliminate all frequency shifts. In the combined systematic analysis these shifts are instead treated as residual effect, incorporating all, the small measured frequency shifts, their uncertainties and the higher order contributions.

It is then further shown in Appendix A, that the relative shift of the difference frequency is directly related to the sum of the relative axial shifts measured for magnetron and cyclotron excitations.

For the Larmor frequency difference $\Delta(\Delta\nu_{\mathrm{L,tot}}) = \Delta\nu_{L,2} - \Delta\nu_{L,1}$ the relative systematic shift can then be expressed as

$$\begin{aligned} \frac{\Delta(\Delta\nu_{L,tot})}{\nu_L} &= -\frac{\nu_z^2}{\nu_+^2}\frac{\epsilon_{\mathrm{mag}}}{r_+^2}\left(\rho_2^2 - \rho_1^2\right) \\ &= 6 \times 10^{-13}, \end{aligned} \tag{5.51}$$

where ϵ_{mag} is the sum of these relative axial frequency shifts observed for subsequently measured excitations of magnetron and cyclotron to the identical radii $r_+ = r_-$. The index *mag* indicates, that the shift solely depends on the magnetic contributions.

5.7.2 Different Axial Amplitudes

The $\Delta\nu_L$ measurement is performed by first thermalizing the axial mode of the $^{20}\mathrm{Ne}^{9+}$ ion, then changing the ring voltage to a higher value to bring $^{22}\mathrm{Ne}^{9+}$ into resonance with the tank circuit. This voltage increase will slightly decrease the axial amplitude of the $^{20}\mathrm{Ne}^{9+}$ ion. This order is chosen as the axial amplitude of lower mass ions is nominally larger compared to heavier ions when they are of identical temperature.

This can be important, as in the presence of a B_2, the average magnetic field experienced by the ion is dependent on the axial amplitude[a]. The residual axial amplitude difference results in a shift that has been evaluated to about 3×10^{-14} and can therefore be neglected at the current level of precision.

---

[a] Contrary to odd order magnetic field inhomogeneities, which will average out.

6 Coupled Ions: Tools and Methods

After having introduced the mathematical framework to understand the coupled ions motion, here I will introduce the general idea of the Δg measurement. After going through the measurement routine, similar as has been done for the single ion g factors, the necessary tools and methods to implement such a routine will be explained. I will further provide technical details and general ideas, which will likely find applications in other scenarios as well. Along this chapter, I will also discuss and motivate the specific choices of parameters made for this measurement to give the reader a better understanding of the challenges one faces when trying to implement a similar measurement scheme. Finally, this chapter will be concluded by going through the characterization measurements of the system, such as a Rabi frequency determination, tuning ratio and magnetic field inhomogeneity scans and a measurement on the stability of the separation distance in the coupled state.

6.1 The Measurement Routine

The measurement idea revolves around two main principles. First, it is assumed that the spins of two ions in close proximity, here achieved by coupling them on a common magnetron orbit, behave coherently to a large extend. Secondly, that the coherent, or common behaviour of the spins can be used to determine their Larmor frequency difference. However, while the actual measurement is to be performed in the coupled state, the readout of the individual spin states of the ions is only possible when the ions are separated. Therefore, the measurement sequence can be characterized by four main consecutive steps. First, the spinstates of the individual ions have to be determined. Subsequently, the ions will be mixed and prepared on a common orbit, which should be as similar as possible for each cycle of the measurement. Thirdly, the actual measurement sequence based on simultaneous Ramsey-type excitation scheme of both spin states can commence. Finally, the ions have to be separated again to facilitate the determination of the individual spinstates once more, concluding a measurement cycle. In the following, such a fully automatized[a] sequence will be described in more detail.

The measurement sequence begins with both ions at their thermal radii and stored in separate traps, one in the AT and one in the PT. Here, the ion starting in the AT will be referred to as the *lower* ion, which makes the ion in the PT the *upper* ion, according to their positions in the trap stack. As there is no distinction between the ions after the mixing process, the order can be chosen arbitrarily. More importantly, as the order does not matter, it can be kept the same throughout the measurement procedure, which significantly simplified the adaptation of the control system of the trap, which initially did not account for two measurement ions.

The measurement begins with the determination of the spin state of the ion in the AT by irradiating the microwave to induce a spin transition. The difference in the magnetic fields between AT and PT, stemming from the ferromagnetic ring in the AT, with $B_{0,\mathrm{AT}} \approx 3.86\,\mathrm{T}$ versus $B_{0,\mathrm{PT}} \approx 4.02\,\mathrm{T}$ is crucial. It ensures, that the applied microwave can only affect the ion in the AT while not addressing the ion in the PT. With a difference of Larmor frequencies of about 4 GHz due to the magnetic field difference and a Rabi frequency of only about 2.5 kHz, this can safely be assumed here.

After the spin state of the lower ion has been determined, it is transported to one of the lowest electrodes below the AT (T_2), while the second ion is now brought into the AT. The magnetic field in T_2 is very similar to the one in the PT, or even a bit larger due to the B_2 contribution. When irradiating the microwave frequency for the upper ion now in the AT, the spin state of the lower ion (T_2) is again not affected.

After determining the spin state, the upper ion is transported back into the PT and excited to $r_- \approx 600\,\mu\mathrm{m}$ to prepare for the mixing process. This process is initiated by bringing the lower ion into an electrode close to the PT (LE1). The upper ion is now moved further down again, until the ions are only separated by a single grounded electrode[b].

Now, this electrode is set to a voltage of −98 V, which is the most negative voltage available for StaReP [71]. Here, the electronic filters with a combined time constant of 6.8 ms [49] restrict the maximum speed of voltage changes to an adiabatic range, such that the ions cannot gain significant axial energy from this process. This is achieved, when the change of the axial frequencies (or voltages) is occurring on much slower time-scales than the axial motion itself. While this is a useful implementation to make typical transport processes safe, it poses some limitations for the mixing of the ions. The change of

---

[a] While this achievement is now boiled down to a simple footnote, I still want to highlight that getting the complete sequence to run without having to manually interfere has been one of the major efforts of this work. The necessary control and understanding of the behaviour of coupled ions to allow such an automatic process can only be hinted at here.

[b] For this, LC2 was used as the field penetration is much larger than for the smaller ring electrode and thus simplifies the application of symmetric potentials.

the voltage by the largest available amount achieves the transit through the state where the potential exhibits a $C_2 \approx 0$ as fast as possible. This is critical because at that point an uncontrolled increase of the ions magnetron modes is possible, as without a C_2, both, magnetron and axial frequency become very small. Therefore, any patch potential, a charge on a non-conducting part of the assembly, could cause the ions to enlarge their radius until they hit the electrode and are lost. Furthermore, any change of the potential cannot be adiabatic anymore when the frequencies are small, making a fast transition of this range the best solution. With the thus optimized mixing routine, no excessive change of the magnetron modes has been observed, as the combination of initial separation distance and common mode radius[a] has been roughly similar every cycle. However, an increase of the axial energy is typically observed. In order to dissipate the excess energy, the ions are alternatingly brought into resonance by changing the ring voltage several times until the axial modes are thermalized.

At this point, the ions are situated in a common potential well and are coupled on a common magnetron orbit, described by a combination of common mode radius r_{com} and separation distance d_{sep} (see section 5.5.1), with the individual parameters varying to some degree. The magnetron excitation prior to the mixing of the ions has proven to be crucial to prevent them from starting with a too small separation distance, which can result in a strongly coupled system, where it becomes impossible to detect the ions due to large frequency shifts combined with a strongly degraded signal. This will be discussed shortly (see section 6.2.1). However, with the routine thus optimized, this problem did not occur for the over 500 subsequent attempts. With both ions axially thermalized, the separation distance can now be determined from the observed axial frequency shift as given by Eq. (5.10c), when compared to the frequency of a single cold ion at identical voltages.

Now, the ions are ready to be transferred into their intended measurement state with a separation distance of typically around $d_{\mathrm{sep}} \approx 400\,\mu\mathrm{m}$ and ideally zero common mode radius. The preparation of such a state is achieved by a combination of a direct cooling of the separation mode in combination with a transfer of the undesired common mode radius to the separation mode. The latter process is described in more detail in section 6.2.3. The combination of these techniques facilitates a gradual reduction of the separation distance to within $\pm 15\,\mu\mathrm{m}$ of the intended distance[b], while also guaranteeing $r_{\mathrm{com}} \leq$

---

[a] Only the separation distance can initially be observed and is varying within 350 to 500 µm, no information about the common mode can be inferred yet. An excessive change of the radii during mixing would have led to the initial separation distance becoming to small to even detect the ions for some of the cycles. This has not been observed.

[b] This can be further optimized, however resulting in a significantly increased cycle time as the process of carefully cooling and again determining the radius has to performed iteratively. By choosing a weaker cooling, the resulting distribution will be smaller but takes much longer to achieve.

100 µm. The complete process of preparation will be explained in more detail in section 6.2.

Finally, both ions are cooled in their respective cyclotron modes via a double-dip, which can also be used to monitor the approximate magnetic field. With the ions thus prepared, the irradiation of the microwave can commence, following a Ramsey-type scheme. This process is illustrated in Fig. 6.1 (C) and consists of a $\pi/2$ pulse, the evolution time τ_{evol} followed by a second $\pi/2$ pulse. Note, that the $\pi/2$ pulse is defined here to achieve a 50 % spin flip probability. This definition can equivalently be described as a rotation of the Bloch vector to the equatorial plane or the projection of the spin vector onto the $z-$axis becoming zero.

Subsequently, the individual spin states have to be determined again. While it was possible to intermittently detect the ions in the coupled state in the AT, the resolution and reproducibility was far too low to allow for any automatic measurement routine to even deterministically detect them, much less to consistently quantify the axial frequency change to determine their spin states. Therefore, the ions have to be separated again at the end of each cycle.

To this end, one ion[a] is resonantly pulsed to a cyclotron radius of about $r_+ \approx 800\,\mu\mathrm{m}$. Subsequently, both ions are cooled in their respective magnetron modes. This results in a configuration, where one ion is at thermal amplitudes in all modes, while the second ion is on a large cyclotron radius. The additional cyclotron magnetic moment of the ion on a large radius causes an additional axial force when combined with a magnetic gradient. To utilize such a force for the means of a separation, a modified version of the transport process into the AT is applied. The additional force experienced by only one of the ions upon entering the magnetic bottle, combined with precisely tuned potentials is used to deterministically separate the ions again. The separation will be covered in more detail in section 6.2.6. After cooling the thus separated ions, they are back in the initial configuration and the cycle is repeated. The complete measurement cycle is schematically illustrated in Fig. 6.1, the evaluation of the signal as shown in (E) is explained in the following chapter.

6.2 Working with Coupled Ions

In this section, the above introduced ideas of working with coupled ions will be discussed in more depth, while at the same time providing practical and technical details how the corresponding methods have been implemented for the work with $^{20}\mathrm{Ne}^{9+}$ and $^{22}\mathrm{Ne}^{9+}$. The section is structured such as to describe the situation beginning after the ions have

---

[a] The one you wish to become/stay the *upper* one.

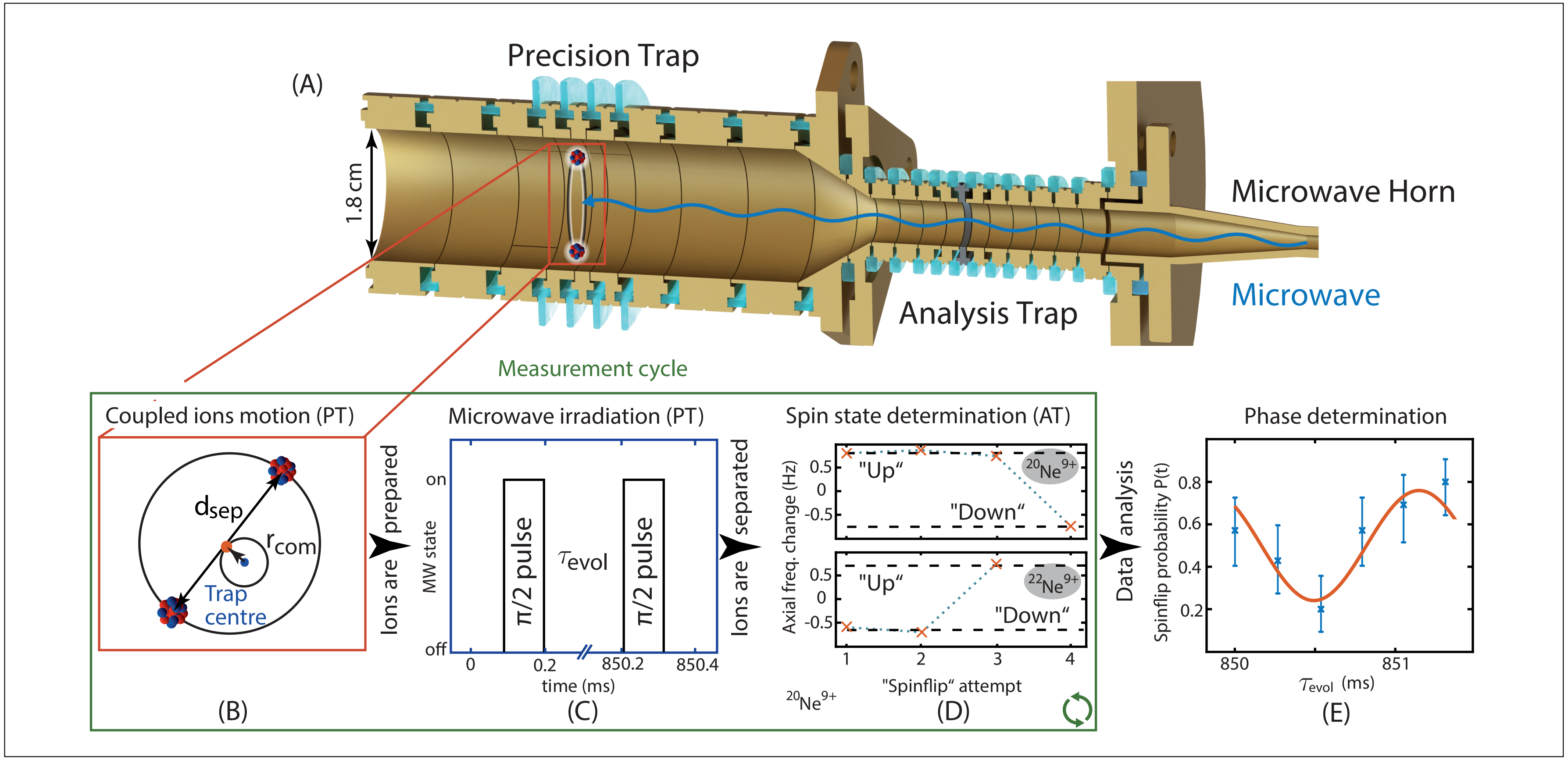

Figure 6.1: Illustration of the complete measurement process. The trap tower with the coupled ions sitting in the PT and a microwave irradiation is shown (A). Once the initial configuration has been determined (B), the ions are brought into the desired measurement configuration and the microwave pulse sequence commences (C). After the ions are separated again, the individual spin states are determined once more (D). This cycle is repeated, until the common behaviour of the spins can be evaluated to extract the Larmor frequency difference (E). Figure adapted from T. Sailer et al., submitted 2021 [37].

been mixed and will then follow the important steps of the measurement sequence until the ions are separated again.

After the ions have been mixed, they first have to be prepared into the state intended for the measurement. It has already been mentioned that both ions are repeatedly (and alternatingly) brought into axial resonance, to ensure that they are both thermalized in their axial mode. This is necessary, as it has been observed that the ions can gain significant axial energy during the mixing process, possibly due to a ”collision” (or the ions coming close to each other) or due to the change of the potential. As long as significant axial energy is present in either ion, an exchange of axial energy between the coupled ions has been observed. However, even in a state with large axial amplitudes they are already strongly coupled in the magnetron mode, as the magnetron Rabi frequency Ω_- (see Eq. (5.8c)) remains significantly larger than the difference of the magnetron frequencies even at separation distances up to about 1 mm.

This results in a rather uncontrolled behaviour, where the ions are changing in frequency depending on their respective axial amplitudes. As the energy is seemingly exchanged at random between the ions, the frequencies do not remain stable due to their interaction and the constant coupling with the resonator and the further resulting change of the effective distance. The result is a chaotic system, in which it might be possible to cool one ion and observe a dip, only to then bring the second ion into resonance and have the signal chirp away while the ion cools in its axial mode. By intermittently cooling both their axial modes until they are fully thermalized, this can be brought back under control. Only then, the frequencies become stable and a deterministic approach to achieve the desired state is possible.

6.2.1 Determining and Controlling the Initial Mixed State

After the mixing of the ions, once stable frequencies can be observed, the initial state of the coupled magnetron motion has to be determined. This state consists of a distribution of common mode radius and separation distance, which is varying to some extend every cycle. Foremost, the interest lies in the separation distance between the ions, which can be directly inferred from the observed respective axial frequency shifts with respect to the nominal frequency that would be observed at the same voltage for a single, cold ion (see Eq. (5.10c)).

The suitable range of separation distances is mostly governed by practical limits. Too small separation distances lead to a deterioration of the signal quality and make it significantly harder or impossible to detect and work with the ions, while too large distances increase the systematic uncertainty. The lower limit is illustrated in Fig. 6.2. Here, the signal shape of an axial dip (blue) and cyclotron double-dip (red) for a single, uncoupled ion (left plot) is compared to the same ion in a coupled state with a separation distance of $d_{\mathrm{sep}} = 410\,\mu\mathrm{m}$ (centre plot) and a separation distance of $d_{\mathrm{sep}} = 360\,\mu\mathrm{m}$ (right plot). The ring voltage has been adjusted for each measurement such that the ion is in resonance with the tank circuit, the sampling time is identical for each spectrum.

The degradation of the signal is clearly visible. It is caused by the permanently changing axial amplitude of the observed ion[a] in combination with an amplitude dependant frequency shift. In the first approximation it was shown that the axial frequency shift is mostly determined by the separation distance (see section 5.10c or Appendix Eq. (8.7)). However, for decreasing separation distances the effective distance starts to become more and more dependent on the axial amplitude as well. Therefore, the thermalisation of the observed ion modulates the frequency shift by a small amount, leading to a frequency jitter. With a less stable axial frequency, the dip appears to be *smeared out*.

Practically, this limits the separation distance to a minimum of $d_{\mathrm{sep}} = 340\,\mu\mathrm{m}$ for $^{20}\mathrm{Ne}^{9+}$ and $^{22}\mathrm{Ne}^{9+}$, where the automatic fitting routines become unstable and frequency uncertainties excessive, thus making it the smallest separation distance for which a measurement could still be performed. Furthermore, the time to prepare the ions to smaller separation distances starts to increase, as the cooling has to be performed in ever smaller steps to avoid the distance becoming too small. A further reduction of the separation distance would require significant modifications to the automatized methods that have been applied for this measurement. After these discussions, the initial excitation of the upper ion to $r_- \approx 600\,\mu\mathrm{m}$ before mixing can also be understood. While the exact distribution of the angular momentum into common and separation mode is different every cycle, the large initial radius results in the ions not coupling on very small initial separation distances, where they would not be visible anymore. The additional magnetron excitation chosen here has proven to be large enough, as, with the exception of a few single runs, the initial separation distance has always been larger than the intended $d_{\mathrm{sep}} = 410\,\mu\mathrm{m}$.

For the upper limit of separation distances, one finds that both, the imbalance of the radii $\delta_{\mathrm{mag}} \propto d_{\mathrm{sep}}^3$ as well as the absolute difference in radii becomes larger, leading to an increased systematic uncertainty. One should therefore measure at the smallest possible separation distance to minimize systematic effects, while larger separation distances can serve as a consistency check.

---

[a] The observation is only possible due to the coupling of the ion to the resonator. Even in thermal equilibrium, the instantaneous axial amplitude then follows a Boltzmann distribution. As the second ion is far detuned from the resonator, its axial amplitude is constant.

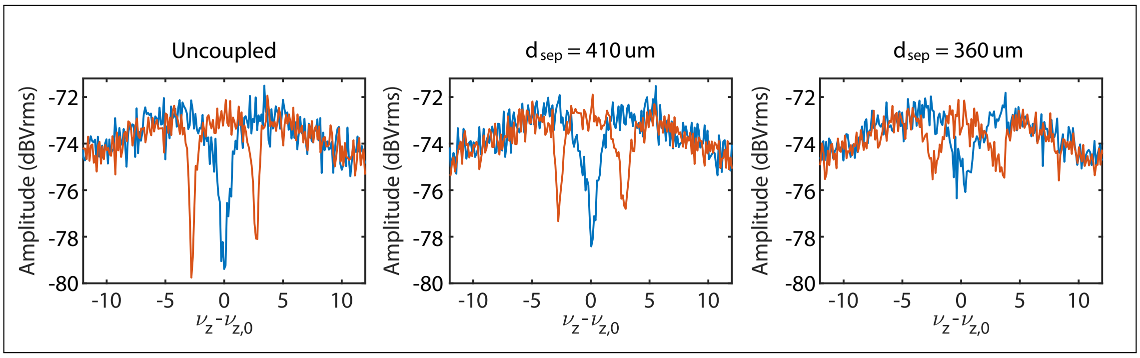

Figure 6.2: Comparison of the dip (blue) and double-dip (red) signal for a single ion (left) versus the same ion but in a coupled state for two different d_{sep} values. While the signal is already visibly worse for $d_{sep} = 410\,\mu\mathrm{m}$, the shape quickly deteriorates for distances below that, making the $d_{sep} = 360\,\mu\mathrm{m}$ already difficult to process automatically.

6.2.2 Preparation of the Separation Distance

Once d_{sep} has been verified to be larger or close[a] to what is aimed for, the preparation of the mixed state can begin. For very large initial separations (more than 510 µm), the separation mode is immediately cooled by performing weak sweeps around the magnetron sideband coupling frequency $\nu_{\mathrm{RF}} = \nu_z + \nu_{-,c}$. A sweep with an amplitude of 30 mV is once applied from −20 Hz to +20 Hz for a duration of 10 s around the coupling frequency. As the separation mode and common mode difference frequency is $\frac{\Omega_-}{2\pi} \leq 10\,\mathrm{Hz}$ for such large separations, such a drive will affect both modes and cool them, but will not allow an accidental cooling to too small separation distances, as the coupling stops once the axial frequency becomes smaller due to the reduced separation distance. The second drive is then applied again with the same amplitude, but now sweeping in the opposite direction in the range of +50 Hz to −5 Hz with respect to the coupling frequency of axial and common mode.

The drive therefore begins above the coupling frequency of the separation mode[b] and an energy transfer to the axial mode begins when coming closer to the coupling frequency. As a smaller separation distance results in a lower axial frequency, this sweep effectively follows the resulting chirp of the ion **if** the ion is allowed to cool sufficiently fast. This requires the coupling to be weak since an additional axial amplitude increases the effective distance between the ions and results in the axial frequency becoming larger again. Ultimately, this requires the drive to be weak with respect to the cooling time of the ion

---

[a] It is fine to be slightly below the intended separation distance as I will discuss tools to enlarge it soon.

[b] The coupling frequency for magnetron is $\nu_z + \nu_-$, the common mode frequency is basically identical to the normal magnetron frequency and the separation mode frequency is at most 25 Hz larger than the common mode even at the smallest used separation distances.

and restricts the possible range of the sweep to a small frequency range around the resonance frequency of the tank circuit, where the shortest cooling times are achieved. If the axial amplitude is not damped sufficiently fast, the coupling drive can stay resonant, thus reducing the separation distance too far. If the sweep is correctly calibrated however, it offers a rough control of the final separation distance as the coupling drive can simply be stopped, when the axial frequency has shifted to the corresponding frequency. To this end, the ion is brought back into resonance by adjusting the ring voltage and the sweep can be repeated. Once the thus accumulated axial frequency shift corresponds to the desired separation distance, the process can be stopped.

If the cooling has been too strong or the separation distance was already too small initially, a state can be reached where the ions are not detectable anymore as the dip signal is too far deteriorated in addition to the axial frequency being shifted far away from resonance[a]. In these cases, the ions cannot be detected without any additional excitations. Here, a few strong excitations have been repeatedly successful to remedy the situation. To this end, a strong and fast sweep[b] over a range starting **below** the lower magnetron sideband $\nu_z - \nu_-$, which causes an exponential increase of both, axial and magnetron amplitudes, to a few hundred Hz above the axial frequency typically serves to allow a detection of the ions again. At the end of the sweep, the excited ion should roughly be observable at the stop frequency of the sweep with significant axial amplitude. During the subsequent cooling of the axial mode due to the interaction with the resonator, the frequency will slowly chirp to lower values once more as the coupling with the second ion becomes stronger again. If the separation distance has been successfully increased, it will however stop at an axial frequency within reasonable limits, where some of the more deterministic methods explained in the following sections can be used. If the process was not successful, it can simply be repeated as no ion loss has occurred when using this sweep. This method has mainly been applied during the initial work with the coupled ions and was not required after the following methods had been well tuned.

6.2.3 Common to Separation Mode Transfer

A method of transferring energy, or rather angular momentum, between common and separation mode has been discovered by Rainville and Thompson for the application in the Two-Ion Balance [82, 84]. This important tool is described in great detail, in these

---

[a] The problem is not necessarily the large shift, but more importantly that it is unknown. While the axial frequency is shifted only about 150 Hz at $d_{\text{sep}} = 410\,\mu\text{m}$, at $d_{\text{sep}} = 200\,\mu\text{m}$ the shift is already about 1.2 kHz. In combination with a strongly deteriorated signal, the ions are almost impossible to find without exciting them.

[b] Typically started 10 kHz below the nominal axial frequency ν_z, with a 2 V amplitude to ν_z+ 500 Hz, with a sweep time of 100 ms, cryogenic excitation switch *on* (see section 4.2.5 for the switches).

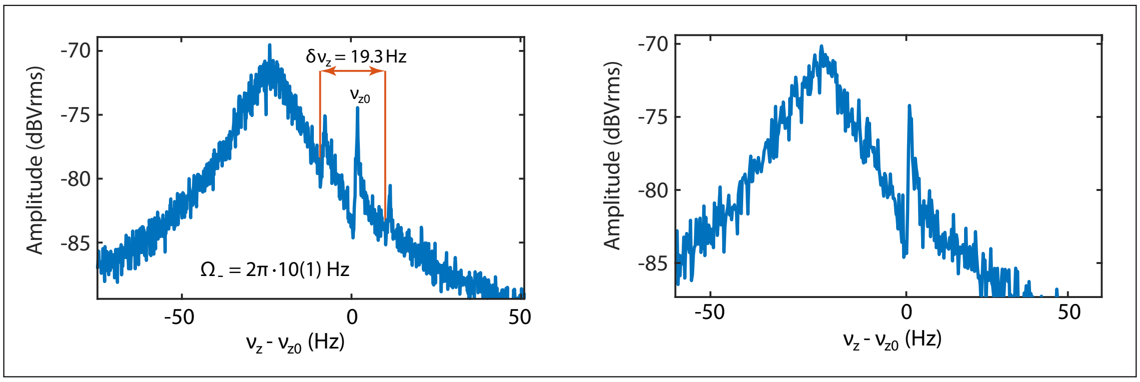

Figure 6.3: Comparison of the coupled ion axial signal for two different common mode radii, while a large C_4 anharmonicity is applied. The axial frequency (centre dispersive dip on the left, single dip on the right) is shifted in both cases from the centre of the resonator due to the effective magnetron radius and the applied C_4. On the left hand side, the coupled ions have been excited to a common mode radius, leading to a frequency modulation with Ω_-. For the right hand side spectrum, the common mode has been cooled.

works and allows to deterministically decrease the common mode, while enlarging the separation distance. In the following, this method will be qualitatively described and it will be explained how it has been applied to the Δg measurement of $^{20}\mathrm{Ne}^{9+}$ and $^{22}\mathrm{Ne}^{9+}$. The technique is based on the modulation of the effective magnetron radius[a] due to the interplay of common and separation mode with the beat frequency Ω_- (see Eq. (5.33)). When applying a C_4 detuning, the axial frequency becomes dependent on the effective magnetron radius and its modulation is translated into a modulation of the axial frequency. The strength of the modulation depends on the ratio of common to separation mode, with a 100% modulation when $r_{\mathrm{com}} = \frac{d_{\mathrm{sep}}}{2}$. An example for such a modulation is shown in Fig. 6.3. In both cases shown here, the ions are first prepared with a separation distance of $d_{\mathrm{sep}} = 470(15)\,\mu\mathrm{m}$, which leads to a calculated magnetron beating frequency of $\Omega_m = 2\pi \cdot 10(1)\,\mathrm{Hz}$ (see Eq. (5.8c)). The uncertainty stems from the uncertainty of the exact separation distance. The right hand figure in 6.3 shows the state with a cold common mode. In the left hand figure, the axial spectrum after an excitation of the common mode to $r_{\mathrm{com}} \approx 140\,\mu\mathrm{m}$ is shown. The sidebands are spaced as expected due to the frequency modulation with the beating frequency of the two modes.

This beating can be exploited by applying a continuous excitation below the nominal axial frequency, combined with a C_4 applied such, that the ion is shifted to higher axial frequencies on larger magnetron radii. The result is an axial amplitude modulation, as the ion is always excited when coming close in frequency to the drive and allowed to cool again afterwards. Effectively, an axial amplitude modulation that is dependent on

---

[a] The actual magnetron radius measured from trap centre to the ion

the phase between separation and common mode motion has now been achieved, similar to the coupling of modes that is achieved via the application of a sideband drive. The persistent axial excitation can be seen as a change of the instantaneous magnetron frequency when the ion comes into resonance with the drive. This creates a phase advance or lag between the ions, depending on the chosen parameters. Due to the modulation of this additional phase with the beat frequency Ω_-, an effective transfer of either common mode to separation mode or vice versa can thus be accomplished.

However, as the modulation strength is not only dependent on the detuning but also on the radius of common mode itself, the coupling has to go to zero when no or close to none common mode is left. It has been shown that an effective transfer of the angular momentum between the modes can be achieved and further, that the angular momentum is conserved during the coupling [82].

This method can now be applied to get rid of the undesired common mode as well as increase the separation distance at the same time. This is especially important, as the separation distance cannot be excited directly, at least not using a dipolar excitation. Such an excitation acts linearly on the magnetron radius of both ions, effectively only changing the common mode radius as the ions are in phase and displaced by an identical amount.

However, an excitation of the common mode, followed by such a transfer of the angular momentum to enlarge the separation distance is now possible. It should be noted that cooling the separation mode directly is possible, since the symmetry of the motion is broken when coupling the magnetron mode of only one ion to its axial mode with the conventional sideband coupling, using a quadrupole field as described in section 2.5.

The common to separation mode transfer is experimentally applied by first adding a C_4 contribution to the potential, such that the axial frequency is shifted towards larger frequencies. Now, the ring voltage is adjusted such that axial frequency is again below the resonance frequency of the tank circuit by at least $2\frac{\Omega_-}{2\pi} \approx 30\,\mathrm{Hz}$. Now, a weak[a] axial drive is applied just below the lower current axial sideband[b] frequency $\nu_z - \frac{\Omega_-}{2\pi}$, such that it is not yet affecting the ion. The drive is now slowly swept to higher frequencies over 90 s, stopping after a range of $2\frac{\Omega_-}{2\pi}$. If done correctly, the axial frequency will have increased by about the sweep range due to the increase of separation distance if there was sufficient common mode present. When now determining the common mode radius, it should have decreased. While intermittently cooling the separation distance to always stay in a similar range, this process is repeated until the axial frequency and

---

[a] I really mean that! Here, an amplitude of 25 mV, attenuated by 20 dB, applied with the cryogenic switch in the *off* (high impedance) state has been used. Remember, that this drive is amplified by the axial resonator.

[b] The sideband due to Ω_-!

thus the separation distance no longer increases. Finally, it can be confirmed that when detuning the trap, neither sidebands are observed nor can the common mode radius be resolved[a] when compared to the now much larger separation distance, $d_{\text{sep}} \gg r_{\text{com}}$. Both indicate that the common mode has been sufficiently cooled. This indication, and the implications that can be drawn from so far observed parameters of modulation strength, sideband spacing, C_4 shift of the axial frequency and the determined separation distance will now be further discussed when trying to determine common mode quantitatively.

6.2.4 Measurement of the Common Mode Radius

The determination of the common mode radius is more difficult than the separation distance, as there is no directly related observable in the coupled system. Whereas both, the beating frequency and the axial frequency shift yield a good resolution for the separation distance, the common mode can only be inferred indirectly. It was shown in the previous section, that a large common mode results in a frequency modulation and observable sidebands when detuning the trap. As long as that is the case, it is clear that the common mode must be too large still as it is intended to be significantly smaller than the separation distance, preferably completely at zero. While the strength of the modulation is an indication for the relative sizes of common and separation mode, determining their ratio from the observed dispersive[b] and deteriorated dip signals does not serve to achieve a useful precision.

For a more deterministic characterization, the common mode is first transferred to the separation mode with the method described above, until the separation mode can no longer be observed to increase. At this point, there should be no discernible sidebands in the spectrum when detuning anymore. Once this is achieved, a C_4 contribution is applied. For small common mode radii, the magnetron radius determined via the observed axial frequency shift should be equal to $\frac{d_{\text{sep}}}{2}$, which is not affected by a potential residual modulation.

However, there is a problem in this approach which is not present when working with single ions. For a single ion, one can simply apply the C_4 contribution and measure the axial frequency for a cold ion, then excite the ion and compare the axial frequencies for identical trap settings. This is not possible for the coupled state and one has to rely on an initial calibration performed with a single cold ion, such that it is not shifted when applying C_4. Now, it can only be assumed that also the frequency of the coupled ion

---

[a] The effective magnetron radius is $r_{\text{eff}} \approx \sqrt{\frac{d_{\text{sep}}{}^2}{4} + r_{\text{com}}^2}$, therefore small common mode radii are hard to resolve.

[b] The shape of the dip when it is not centred on the resonator, but on the flank. There, a combination of dip and peak are visible, see for example [86].

would not be shifted due to the detuning, despite the now slightly different voltages[a] and the coupled state of the system.

Furthermore, as the common mode and separation distance add quadratically, the much smaller common mode becomes hard to resolve. It is then easy to see, that a quantitative determination of small common mode radii quickly becomes complicated, when the common mode is only a fraction of the separation distance.

However, instead of trying to measure the actual size of the common mode, it is possible to determine the minimal radius that can still be reliably resolved. To this end, the common mode is first cooled until it cannot be detected anymore, leaving it at $r_{\mathrm{com,cold}}$. This means, that neither sidebands nor a significant contribution to the detuned frequency shift are discernible.

The common mode is then excited again to pre-determined radii $r_{\mathrm{com,exc}}$, using a pulse calibration performed with a single ion. The final radius will be slightly different every time, depending on how large the initial common mode has been and on the random phase difference ϕ_D between applied excitation and magnetron mode. This will yield the common mode as $r_{\mathrm{com}} = \boldsymbol{r}_{\mathrm{com,cold}} + \boldsymbol{r}_{\mathrm{com,exc}}$, or as the measured axial frequency shift due to C_4 scales with the radius squared (see Eq. (2.10)), $r^2_{\mathrm{com}} = r^2_{\mathrm{com,cold}} + r^2_{\mathrm{com,exc}} + 2r_{\mathrm{com,cold}}r_{\mathrm{com,exc}}\cos(\phi_D)$. For many attempts, the combined term will average to zero and the combination is given by the quadratic sum. Therefore, on average the final radius is mostly given by the excited radius, as long as the excitation is much larger than the initial radius, $r_{\mathrm{com,exc}} \gg r_{\mathrm{com,cold}}$. Here, it was possible to verify, that common mode excitations $r_{\mathrm{com,exc}} \geq 100\,\mu\mathrm{m}$ can be detected with 100% fidelity. Consequentially, when one fails to detect a common mode, this can be given as an upper limit, resulting in a limit for common mode radius of $r_{\mathrm{com}} \leq 100\,\mu\mathrm{m}$ for the complete measurement. This limit could likely be further decreased, as for an initial radius of this order, the excitation of similar magnitude would be expected to yield a different result every time, depending on the random phase between excitation and initial radius. As the result has been consistent for several attempts, the cold radius is most likely significantly below this limit for most of the measurement cycles. However, as the radius is only confirmed to not be detectable anymore each cycle, this serves well as an conservative estimation.

Finally, it has to be noted, that the determination of the radii via the detuning of the trap is not consistent with the determination of the separation distance via the observed axial frequency shift. The data for all measurements is shown in Fig. 6.4, where the blue crosses correspond to half of the determined separation distance. The red points correspond to the determined full magnetron radius measured via the shift when applying a C_4 contribution. The mean value for $\frac{d_{\mathrm{sep}}}{2}$ (yellow) is found to be larger than the

---

[a] Adjust by about 30 mV out of 50 V

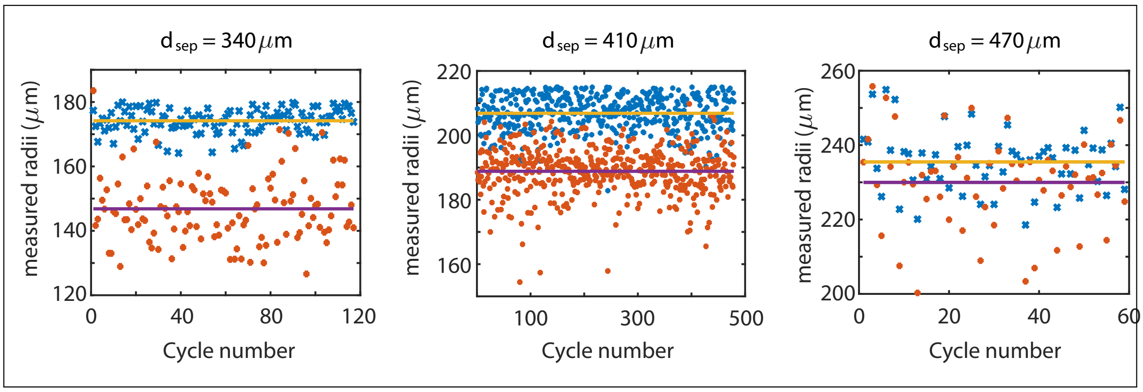

Figure 6.4: Comparison of the $d_{\text{sep}}/2$ half radius and the full measurement of the magnetron radius. Note, that the mean for the measurements via detuning (red dots, purple mean) is always significantly smaller than the value for half the separation distance (blue crosses, yellow mean).

mean value of the complete (or effective) magnetron radius (purple), determined from the additional axial frequency shift. This is not physically possible, as even in the case of zero common mode, the radius of each ion is of at least half the separation distance. Any additional common mode will quadratically add to that[a]. This can be confirmed when the common mode is large enough to actually measure it, but does not seem to work in the case of very small common mode radii. As the discrepancy is largest for the smallest separation distance, and almost vanishes for the largest distance, there seems to be a relation scaling with the ion interaction, that could not be resolved. The most probable reasons are either a residual shift of the axial frequency when applying the C_4 contribution due to a slight unintended change of C_2 despite the tuning with a single cold ion or an additional effect on the coupled ion motion due to the large C_4. However, with the knowledge of the maximum possible common mode radius $r_{\text{com}} \geq 100\,\mu\text{m}$ and no known systematic contribution directly related to the presence of a common mode radius within this given range, this is of no concern for the measurement presented here.

6.2.5 Measurement of the Magnetic Field

To verify the measured magnetic field independently from the cyclotron double-dip obtained in the coupled ion state, an additional double-dip measurement is performed with a single ion directly after the separation of the ions. This measurement is used to then determine the magnetic field and the required microwave frequency for the following cycle. This approach is chosen, as a PnA measurement with the ions in the coupled state has not been yielding stable results. This is mainly due to the much smaller separation

---

[a] When applying a C_4, the observed shift is the time average, scaling $\propto r_-^2$

distance and larger charge states compared to what has been used in the two-ion balance [83, 84], where a similar phase sensitive detection was applied. Consequently, the axial frequency chirps when the axial amplitude becomes excited to allow for a phase determination, combined with the slightly varying separation distance each run did not allow for the necessary phase stability required for a PnA measurement. It would likely be possible to account for the additional frequency shift when measuring further detuned from the resonator to prevent a cooling of the axial amplitude, in combination with tuning to minimize the required axial amplitude and the corresponding frequency chirp. However, as the magnetic field is only predicted for the subsequent run, the double-dip is precise enough as the uncertainty due to drift of the magnetic field between two runs is of similar magnitude than the precision of the double-dip. Thus, the potential precision of a PnA measurement would not yield any improvement at this point. Furthermore, a determination of the magnetic field with the coupled system did not seem wise when implementing the measurement routine due to the degraded signal of the double-dip. This might have had unforeseen effects on the determined cyclotron frequency due to the double-dip fitting model. A systematic shift, causing the irradiated microwave frequency to be always offset from the mean in the same direction, could have larger effects on the measurement than a normal distributed additional jitter.

As the magnetic field is measured once per cycle and used to predict the magnetic field for the next microwave irradiation, this results in an increased jitter for the detuning of the microwave excitation frequency. The measured relative standard deviation of the magnetic field for consecutive runs has been evaluated to 3×10^{-9} and is of the level of the double-dip resolution itself. This is equivalent to an additional jitter of about ±350 Hz in terms of the applied microwave drive. Such fluctuations have been included in the simulations for the initial phase (see section 7.1.1) and do not contribute any additional uncertainty. Furthermore, as the modulation amplitude of the signal will be shown to not be reduced, this does also not pose a restriction for the statistical resolution for this measurement. If a decreased modulation was to be observed, more data points would be required to still resolve the phase with similar resolution.

If required, the precision of the magnetic field determination could be improved upon by using an additional third ion to measure the magnetic field via PnA once the ions have been fully prepared for their measurement. Here, the ions would be prepared to their intended state for the measurement, then transported to another electrode momentarily. A third single ion would then be placed in the PT to determine the magnetic field by performing a PnA sequence. Subsequently, the third ion could be stored in the CT again, while the coupled ions are transported back into the PT for the measurement. The measurement of the magnetic field for each cycle of the measurement is included in the

Appendix B.

6.2.6 Separating the Ions

To separate the ions after the measurement sequence, a scheme depending on the strong B_2 coefficient of the magnetic field in the AT is used. It was already mentioned, that a B_2 contribution to the magnetic field gives rise to an axial force on the ion depending on the magnetic moment. This principle has been used to determine the spin state and the temperature of ions already.

At the end of each measurement cycle one ion is excited to a modified cyclotron radius[a] of about $r_+ \approx 800\,\mu\text{m}$. As the separation distance is much smaller, with $d_{\text{sep}} \approx 400\,\mu\text{m}$, it is thus ensured that the ions are still separated from each other. However, during the excitation, they come close to each other for the brief time when the cyclotron radius matches the separation distance. Therefore, the excitation pulse is preferably kept as short as possible. This is limited as one also wants to avoid a spectrally broad pulse when using very short excitation times. For this measurement, a pulse length of 28 ms was chosen, which has proven to work reliably.

If the pulse is successful, the axial shift of both ions is found to be drastically reduced due to the much larger effective separation between them. In a simplified picture, the ions are now closest when they are on the same side of the trap, where the distance between them is $r_+ - d_{\text{sep}} \approx 400\,\mu\text{m}$ as illustrated in Fig. 6.5. On opposite sides, they are separated by $r_+ + d_{\text{sep}} \approx 1200\,\mu\text{m}$, leaving them on average much further apart than before, with the observed axial frequency shift matching the prediction when using a time averaged distance as an approximation for the effective separation distance.

Therefore, the ions are now left close to their nominal (cold, single) axial frequency. After adjusting the trap voltage, the magnetron modes of both ions can immediately be cooled by performing sweeps in a small range to account for the expected frequency chirp when bringing both magnetron modes into thermal equilibrium. This should leave the ions in a state with one ion being on thermal radii in all three modes, while the other ion is on an excited modified cyclotron radius and its other two modes are at thermalized as well. This state is verified by observing the axial frequency shift, which is now governed by the effective separation of $r_{+,1} = 800\,\mu\text{m}$.[b] Finally, a C_4 detuning is again used to verify the cyclotron radius of the excited ion. The process of changing the radii from the coupled state until they are ready to be separated is schematically shown in Fig. 6.5.

Having the state thus prepared, both ions are transported together towards the AT. The

---

[a] This one will end up in the PT, the cold one in the AT

[b] This is not exactly the same as a separation distance for symmetric magnetron modes, however the effect on the axial frequency is very similar.

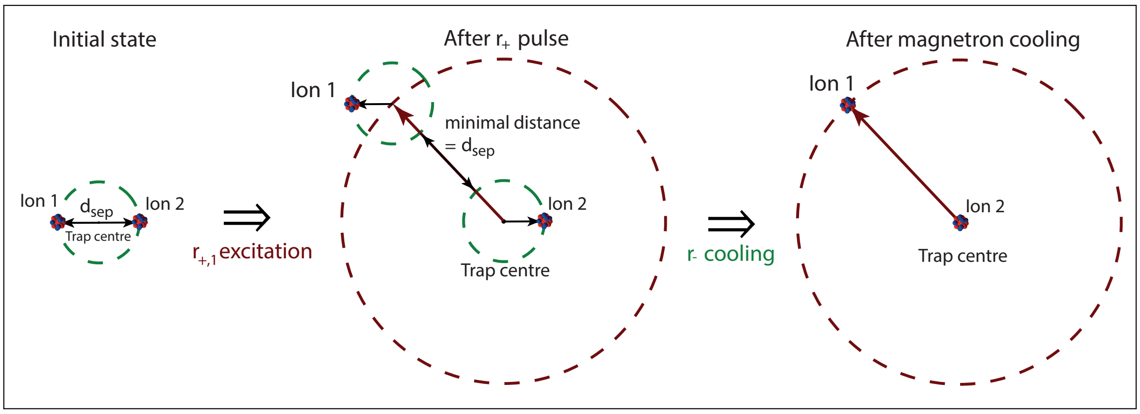

Figure 6.5: The illustration shows the step-by-step transition from the common magnetron orbit until one ion is in the centre of the PT, the other at a large modified cyclotron radius $r_{+,1} \approx 2d_{\text{sep}}$. The effective separation distance is now governed by the cyclotron excitation. After the separation transport starting with such a state, ion 1 will be in the PT, ion 2 in the AT.

process of the separation occurs upon entering the magnetic inhomogeneity towards the AT due to the precisely tuned transport potentials. In Fig. 6.6, the process is illustrated by showing the effective potentials, given as the combination of electrostatic and magnetic potential.

With the ions thus separated, the hot ion is brought back to the PT, where it is cooled and used to determine the magnetic field. It is then stored even further up in the CT, to allow for the cooling of the other ion in the PT. This is necessary, as it can potentially gain axial energy or have an enlarged magnetron radius due to the separation process involving a change of potential wells and a transition through a flat potential. Now being left with two cold separate ions, the individual spin states can be determined again.

The method of separation described here has been tested within the range of $650\,\mu\text{m} \leq r_+ \leq 1100\,\mu\text{m}$. For very small radii, their distinction due to the additional force is not large enough to achieve a separation, while larger radii might leave the ion unconfined during the transport due to the slope of the increasing B_2 contribution to the magnetic field when coming closer to the AT. Both cases could result in a loss of the ion according to the simulation of the potentials, however such small radii have never been attempted to be used for a separation. The limits derived from a simulation of the separation process show the lower critical radius at $r_+ \approx 300\,\mu\text{m}$, the upper limit at $r_+ \approx 1600\,\mu\text{m}$. The complete process has proven to be extremely reliable and has worked flawlessly for over 500 individual runs, starting from the excitation until the final state of separated cold ions. The full process of mixing and separation does not affect either of the spin states of the ions, as has been observed for several repetitions.

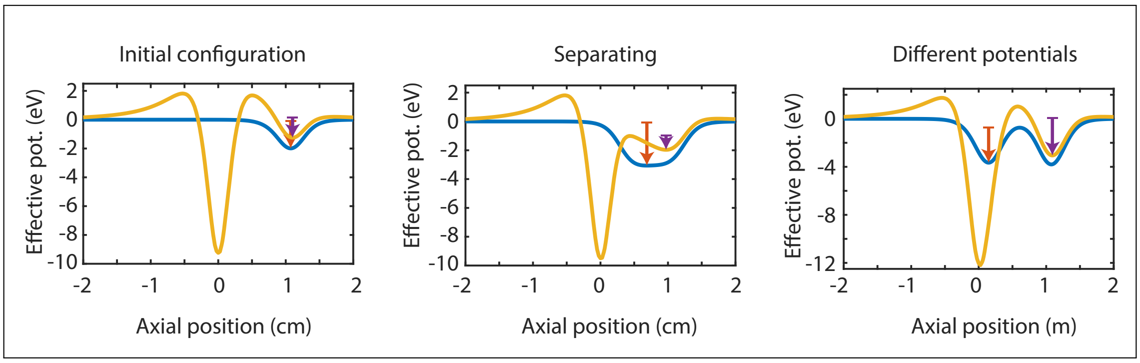

Figure 6.6: Steps of the ion separation. The yellow line shows the effective potential for the ion on a large cyclotron orbit (purple), the blue line is the potential for a cold ion (orange). The height of the arrows represents the minimal potential depth the ion is bound in. In the left figure, the ions are still in the same potential well, but already slightly axially separated. The middle shows the transition of the cold ion through a flat potential into a different potential well. In the right figure, the ions are separated with the cold one ending in the AT, the hot one in an electrode further up. The zero position on the x-axis corresponds to the centre of the AT ring electrode.

6.3 Calibration and Characterization Measurements

6.3.1 Asymmetric Trap

While the magnet is shimmed to be very homogeneous in the centre of the PT, the effect of the ferro-magnetic ring in the AT disturbs the ideal field. A compensation ring [49] has been implemented to correct for the disturbance and keep the B_2 contribution in the PT small. This works quite well, leaving $B_2 = 64.3(32)\,\frac{\mathrm{mT}}{\mathrm{m}^2}$, but also results in a B_3 contribution to the magnetic field. Effectively, the B_3 leads to a change of B_2 along the z-axis. Ideally, the zero point of B_2 would be in the centre of the trap but depends on the exact placement of the compensation ring. As B_2 is not zero in the PT, this ring is currently not in the perfect position and the zero crossing can instead be found by moving the ion along the z-axis of the trap by asymmetrically altering the electrostatic potential. To this end, several shifted positions have been evaluated, where each asymmetric position has been optimized with a new tuning ratio to then determine the B_2 coefficient. After determining such points, a linear interpolation has then been used to minimize B_2. Finally, a position has been iteratively determined where the ion is shifted towards the CT by $\Delta z \approx 1.045\,\mathrm{mm}^a$. At this point, the measurement resolution of B_2, combined with the uncertainty of the electrostatic anharmonicities did not allow for further optimization, being mostly limited by a C_3 contribution to the electrostatic potential, which can be-

---

[a] This is the absolute shift according to the simulation of the electrostatic potential. The precision is of no concern, as one is only interested in the measured B_2 at a certain position.

come sizeable due to asymmetrically applied voltages. Such a C_3, in combination with a B_1 contribution leads to an axial frequency shift (see Eq. (2.23)) which scales with r_+^2, as also the B_2 related frequency shift does, therefore limiting the precision for an absolute value. The B_2 contribution has been evaluated to $B_2 \leq 8\,\frac{\mathrm{mT}}{\mathrm{m}^2}$, as can be derived from the data presented in Fig. 6.7, combined with simulations of the potential to set limits on $C_3 \approx 2(2) \times 10^{-3}$.

6.3.2 Tuning Ratio and Magnetic Inhomogeneities

To fully characterize the asymmetric trap where the measurement will be performed, a ”full” TR scan is conducted using the single $^{2}\mathrm{Ne}^{9+}0$ ion. After applying magnetron mode excitations and tuning the electric potential such that no axial frequency shifts are observed anymore as described in section 4.2.5, the ion is subsequently excited to an identical radius in its cyclotron mode. The comparison of the observed axial frequency shifts due to the cyclotron excitation now correspond to the magnetic inhomogeneities and a well predictable relativistic shift. From this, limits on the magnetic inhomogeneities can be placed which are crucial for the determination of the correct Larmor frequency difference. The result of such a measurement is shown in Fig. 6.7, recorded after a full optimization of the electric potential, which nevertheless accounts for tiny frequency shifts for excited magnetron radii. The difference of shifts observed for magnetron and cyclotron excitations becomes independent of purely electrostatic anharmonicities and ultimately allows to derive the expected shift on a measured Larmor frequency difference (see section 8.3.1).

The observed axial frequency shifts for cyclotron excitations have to be corrected for the expected shift due to the relativistic mass increase. The difference of the relative shift observed for a cyclotron excitation compared to that of magnetron excitations to identical radii can then be used to determine the systematic shift uncertainty as discussed in sections 5.7.1 and the Appendix B. The determined systematic shift averages to a $6(5) \times 10^{-13}$ correction for the separation distance of 411 µm, using the combination of the relative shifts observed for the three largest radii shown in Fig. 6.7. The smallest measured radius here has not been used for the evaluation, as the observed shifts are of similar size as their uncertainty, limiting the resolution. The average of the latter three measurements is used to evaluate the systematic uncertainties, as the model assumes the observed frequency shift to scale $\propto r_+^2$. Therefore, the correction factor $\frac{\epsilon_{\mathrm{mag}}}{r_+^2}$, with the relative frequency shift $\epsilon_{\mathrm{mag}} = \frac{\Delta\nu_z}{\nu_z}$ should remain constant. The uncertainty of this correction is conservatively given as 5×10^{-13}, which equals about three standard deviations of the derived mean correction.

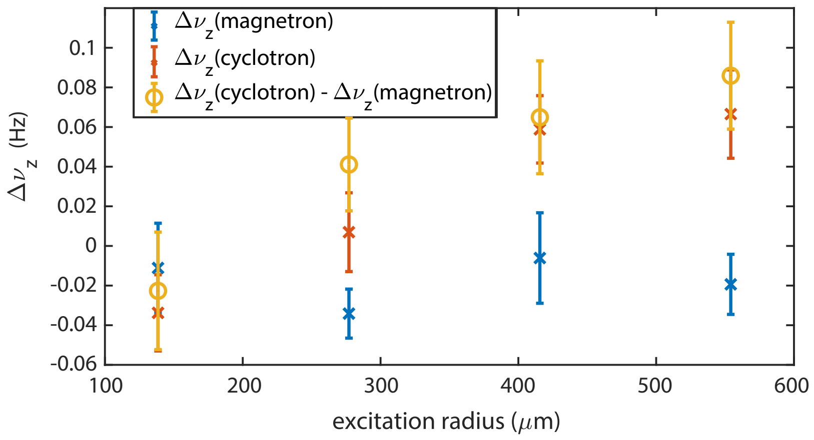

Figure 6.7: Measurement of the full tuning ratio. First, the electrostatic potential is optimized for magnetron excitations (blue), then the axial frequency dependence on identical cyclotron excitation radii is observed (red). The difference of the measured shifts (yellow) due to magnetron and cyclotron excitations allows to draw conclusions about the magnetic field inhomogeneities.

Similarly, the combined shifts can be fitted with the expected quadratic dependency. The resulting systematic shifts one can extract from such a fit range from 4.4×10^{-13} to 8.2×10^{-13}, depending on the exclusion of the first measurement point, an allowed offset or the inclusion of a higher order (r_+^4) dependency in the fit. The largest effect (the one yielding 8.2×10^{-13}) is found, when an additional $\propto r_-^4$ scaling is allowed, then however leading to larger uncertainties of the correction, as two parameters are fit to only four datapoints. The thus extracted range is consistent with the applied correction of $6(5) \times 10^{-13}$. For future measurements, the inclusion of a tunable B_1 and B_2 coil is planned, which, in combination with such a measurement, will allow to achieve significantly smaller systematic shifts and uncertainties.

6.3.3 Determination of the Rabi Frequency

The intended Ramsey-Scheme to determine the Larmor frequency difference requires a calibration of the irradiated microwave pulse length to achieve a $\pi/2$ pulse[a] for the spin states of both ions simultaneously. Such a pulse can be achieved, when aiming at the mean Larmor frequency of the two ions and accounting for the additional detuning, given that the Rabi frequency is larger than half the Larmor frequency difference[b]. If this is not the case, either a pulse shaping, the use of separate microwave generators or

---

[a] Defined as a rotation of the spin vectors to the equatorial plane, corresponding to a 50 % probability for a spinflip to occur.

[b] Otherwise a single pulse cannot reach a 50% transition probability for both simultaneously.

a modulation of the irradiated microwave frequency can be considered instead.

To determine the required pulse length, the Rabi frequency of the system has to be measured. It will also be shown later on, that the visibility of the measured signal directly depends on how well the $\pi/2$ pulse pulse is calibrated, requiring the Rabi frequency to be known as precisely as possibly. Any loss of visibility would have to be compensated by more statistics, resulting in a prolonged measurement time.

As the Rabi frequency depends on the microwave power at the position of the ion, it cannot be predicted precise enough from external power measurements as the transfer efficiency as well as the mode structure in the PT cannot be determined with sufficient precision[a] for this purpose. Furthermore, while the used microwave setup (see section 3.4) enables a measurement of the relative temporal stability of the irradiated microwave power, the used microwave diode [64] is not suitable for precise measurements of absolute power.

Instead, the Rabi frequency for the state of coupled ions has to be determined with an additional measurement prior to the Δg measurement. To this end, a single ion, here $^{22}\mathrm{Ne}^{9+}$, is used. It is placed in the asymmetric trap and excited to a magnetron radius of $r_- \approx 200\,\mu\mathrm{m}$. Therefore, the ion now moves approximately about the same trajectory as in the coupled state with $d_\mathrm{sep} \approx 400\,\mu\mathrm{m}$. This ensures, that in the potential case of a standing wave of the microwave inside the trap cavity, the ion experiences the same microwave power as the coupled ions later on, keeping the Rabi frequency identical for both cases.

When irradiating the microwave ω_RF close to the Larmor frequency ω_L for the duration t with a detuning $\delta = \omega_L - \omega_\mathrm{RF}$, the probability of the ion to undergo a spin transition $P_\mathrm{SF}(t)$ follows a Rabi cycle as

$$P_\mathrm{SF}(t) = \frac{\Omega_R^2}{\tilde{\Omega}_R^2}\sin^2(\frac{\tilde{\Omega}_R}{2}t) \tag{6.1a}$$

$$\tilde{\Omega}_R^2 = \sqrt{(\Omega_R^2 + \delta^2)}. \tag{6.1b}$$

The dependency of the spinflip probability is measured for different microwave irradiation times (or pulse lengths). The result of such a measurement is shown in Fig. 6.8. Here, a Maximum-Likelihood fit is used to extract the Rabi frequency. In this fit, the average detuning is $\delta = 0$ as the microwave frequency is set to match the Larmor frequency. However, as a double-dip is used to determine the magnetic field with a relative precision of 3×10^{-9} as already discussed, the detuning will be different for every at-

---

[a] The microwave absorber, as shown in section 3.1, is meant to prevent a standing wave. How well this works in practice cannot be simulated and has not been investigated thus far.

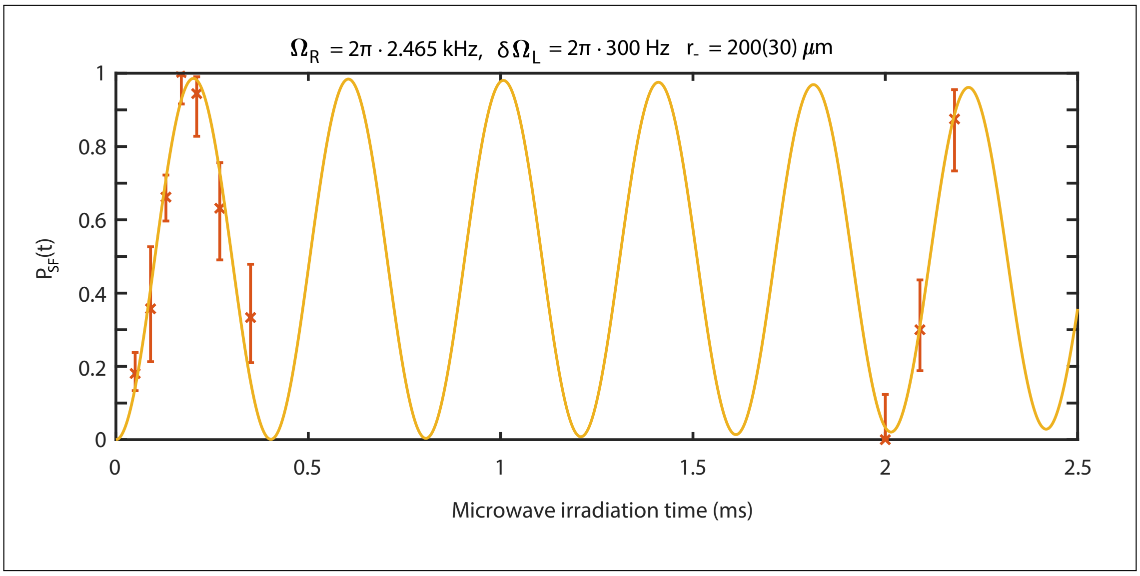

Figure 6.8: Determination of the Rabi frequency Ω_R. The microwave is continuously irradiated for the given time and the spinflip probability $P_{\mathrm{SF}}(t)$ is monitored. The measurement is performed on a magnetron radius $r_- = {}^{d_{\mathrm{sep}}}/_{2}$, to measure in similar conditions as for the coupled ions. The detuning $\delta\Omega_L$ is used to model both, a fixed detuning as well as the jitter of this detuning due to the limited precision of the magnetic field measurement.

tempt. This leads to a reduced amplitude on average, which is included in the fitting routine as the average over a normal distributed detuning, where $\delta\Omega_L$ is the standard deviation of this distribution[a]. The expected jitter matches the result of the fit with about $\delta\Omega_L \approx 3 \times 10^{-9} \cdot \nu_L \approx 330\,\mathrm{Hz}$.

As the Rabi frequency is measured with the microwave drive aimed at the Larmor frequency, the effective Rabi frequency for the case of the measurement where the detuning will be $\delta = {}^{\Delta\omega_L}/_{2}$ has to be calculated. With these considerations, the time for a ${}^{\pi}/_{2}$ pulse[b] has been determined to be $\tau_{\frac{\pi}{2}} = 101.1\,\mu\mathrm{s}$.

The variation of the separation distance during the actual measurement leads to additional changes of the effective microwave power. As a worst case estimate, assuming a standing wave in the trap cavity with a 100% amplitude modulation over a wavelength of $\frac{\lambda}{2} \approx 1.3\,\mathrm{mm}$ and assuming the ion to be located in the largest gradient, the possible change in field amplitude is then limited to about 1.5%. The corresponding maximum deviation for the ${}^{\pi}/_{2}$ pulse calibration is ±1.8 % on the achieved transition probability. It will be shown that such an additional deviation is significantly below the obtained am-

---

[a] The fitting routine first generates a normal distribution. The Likelihood function is then given as the average over the probability given in Eq. (6.1b) with the Rabi frequency Ω_R and δ as normal distributed detunings. $\delta\Omega_L$ is the standard deviation of this distribution and left as a free parameter.

[b] The pulse is defined in terms of the achieved spinflip probability of 50 %, tuned to account for the detuning.

plitude resolution during the measurement and can be neglected here.

6.3.4 Stability of the Separation Distance of Coupled Ions

It has been mathematically derived that the separation and common mode are approximate constants of the motion. While they are expected to be slightly modulated by their respective influence onto each other, they should otherwise remain constant. Additionally, the stability can be experimentally verified. To this end, the separation distance is monitored to constrain a potential change between the measured separation distance at the end of the preparation routine and the actual distance once the microwave is irradiated.

As the axial frequency strongly depends on the separation distance, even tiny changes of d_{sep} become visible immediately, which can be used to study the long term stability of the coupled motion[a]. To this end, the ions are prepared with a separation distance of $d_{\mathrm{sep}} = 405\,\mu\mathrm{m}$, which corresponds to an axial frequency shift $\Delta\nu_z \approx 150\,\mathrm{Hz}$ for $^{22}\mathrm{Ne}^{9+}$. Figure 6.9 shows the axial frequency of $^{22}\mathrm{Ne}^{9+}$ over the course of about 6 h, measured every 2 min. The short break after about 2.5 h in between corresponds to a pause in the measurement after the first 50 spectra, which was then resumed about one hour later.

There is no definite trend of the axial frequency visible, which would correspond to a change of the separation distance. The random variation is likely to be caused by a voltage drift due to temperature fluctuations in the laboratory. Taking the difference between minimum and maximum axial frequency of about 400 mHz as an upper limit estimation, the maxium change of the seperation distance corresponds to less than 0.5 µm over 6 h.

During the Δg measurement, the potential variation of the separation distance is thus limited to about 14 nm when extrapolating to the significantly shorter time between ion preparation and measurement. Such small variations are of no concern. All required methods and characterizations to work with the coupled ions have now been described and a closer look on the actual measurement can be taken.

---

[a] At $d_{\mathrm{sep}} \approx 400\,\mu\mathrm{m}$, a $1\,\mu\mathrm{m}$ change corresponds to an axial frequency shift of 1.2 Hz

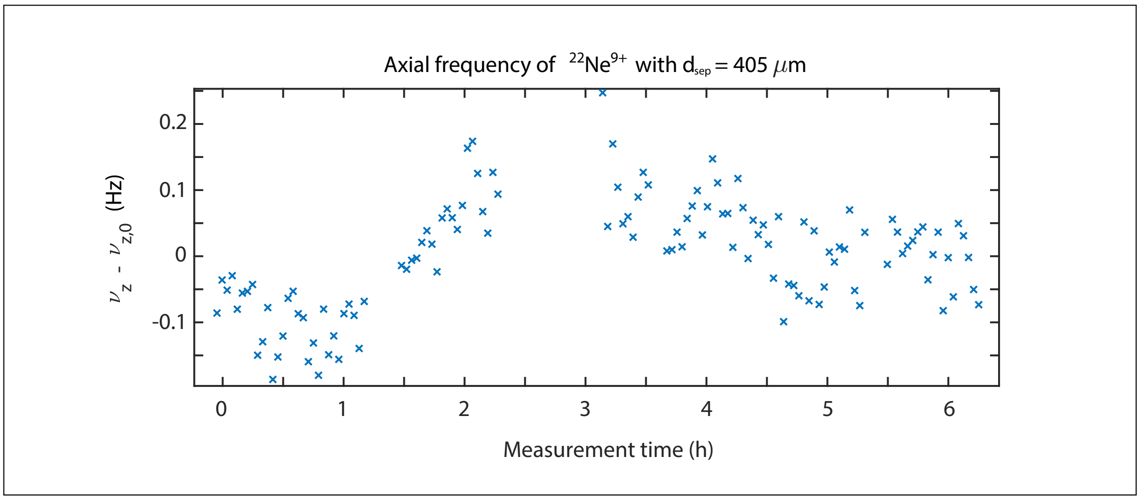

Figure 6.9: Measurement of the axial frequency of the coupled ions over several hours of measurement time. The frequency behaves similar to that of a single ion, depending on the voltage fluctuations due to temperature changes. No drift that would indicate a change of d_{sep} can be observed. The region with data missing corresponds to a pause in the measurement routine, resumed without change to the system after about 1 h. The error bars of the individual measurement points are omitted, as they are identical for each measurement and given by uncertainty assigned to the fit of the axial dip fit. Due to the coupled state, the signal is slightly deteriorated and the uncertainty is estimated to about ±30 mHz for each individual data point.

7 Coupled Ions: Measurement and Results

In this chapter, I will present the main achievement of this thesis – the application of the newly developed technique to measure the g-factor difference of the coupled $^{20}\mathrm{Ne}^{9+}$ and $^{22}\mathrm{Ne}^{9+}$ ions directly and coherently. So far, the coupled motion and related shifts, as well as the measurement routine and tools to manipulate the coupled ions have been introduced. However, while the Ramsey-type microwave irradiation has been mentioned, the critical idea of this measurement is yet to be discussed. While it has been postulated that the spins of the coupled ions will behave coherently due to their proximity and thus identical magnetic field, it has yet to be discussed how the obtained data has to be evaluated. The access to the individual spins has already been covered and is identical to those of the single g-factor measurements, except that the ions have to be separated and moved to different sections of the trap to allow the determination of each spin state. The main novelty to consider in the following pages will be the common behaviour of the spins and what this encodes. Thereafter, I will discuss the data evaluation and the experimental verification of the systematic shift in more detail. Finally, this chapter will be concluded by discussing the result of this measurement and its implications.

7.1 The Coherence of Spin States

While an understanding of the two-ion motion and how to manipulate them is required to completely follow this method, the essential part is the understanding of the measurement signal, or how the measured data has to be evaluated. All of the benefits one gains, rest upon the coherence of the two spin states of the ions which are addressed simultaneously with a Ramsey sequence, consisting of a $\pi/2$ pulse, as previously defined and calibrated to achieve a 50 % spinflip probability, the evolution time τ_{evol} followed by another $\pi/2$ pulse. Let us consider what is actually being achieved here and what that implicates.

The explanation of the complete process can be simplified when assuming, without loss of generality, that the ions are always prepared in the identical spin state for each cycle. While not actually being required, this would not pose a problem to implement. In the following, the *spin-down* state will be represented by downwards pointing arrows of length 1 on the Bloch sphere, $W = -1$. Upwards pointing arrows represent the *spin-up* state with $W = 1$. Generally, the projection of the spin vectors onto the W-axis (see Fig. 7.1) represent the probability to measure the respective ion in the corresponding spin state.

Let us assume that every cycle begins by initializing both spins in the *spin-down* state. Now, a first $\pi/2$ pulse is irradiated at the median Larmor frequency. With a Rabi frequency for the spin transitions of $\nu_R = 2465(16)$ Hz (see section 6.3.3), and a difference of only $\Delta\nu_L \approx 758$ Hz, it is obvious that, despite the comparably small (and symmetrical) detuning, a simultaneous $\pi/2$ pulse can be achieved by the same microwave drive for both ions when irradiated at their mean Larmor frequency and calibrated to be a $\pi/2$ pulse. However, it should be noted that a π pulse is not possible, as the probability will never reach 100 % for a single pulse. When considered in the frame co-rotating with the irradiated microwave drive, this step can be illustrated as shown in Fig. 7.1.

Both spins are rotating counter-clockwise into the equatorial plane around the magnetic field vector of the applied drive $\boldsymbol{B}_{\mathrm{RF}}$, neglecting the detuning for now. This detuning and its effect will be revisited in more detail shortly.

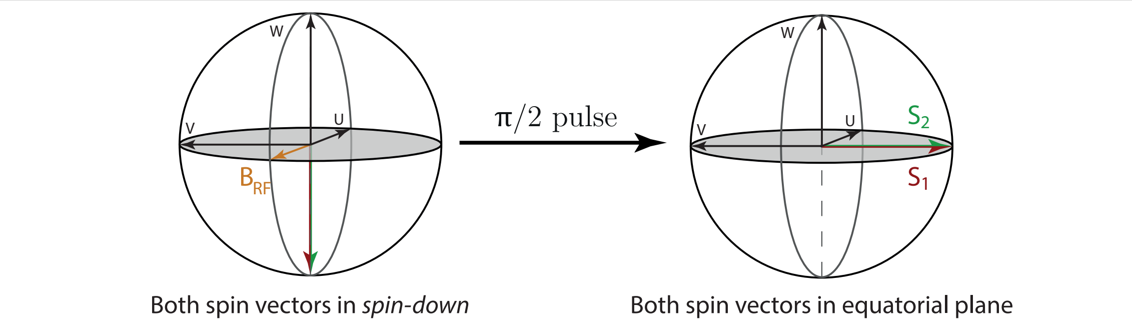

Figure 7.1: Both ions are initially prepared in the *spin-down* state (left), then the first microwave $\pi/2$ pulse is irradiated, bringing both spin vectors to the equatorial plane. The spin vectors rotate around the applied microwave drive B_{RF}, ignoring the small detuning of the drive frequency with respect to the individual Larmor frequencies for now.

One now has to consider what occurs during the evolution time. Ideally, when the magnetic field is considered to be perfectly stable, both spin vectors rotate in the equatorial plane with equal frequencies but of opposite sign $\pm\Delta\nu_L/2$ in the system co-rotating with the exact mean of the Larmor frequencies. From the initial definition of the ions indices, it follows that $\omega_{L,2} > \omega_{\mathrm{RF}} > \omega_{L,1}$, leading to a counter-clockwise rotation for the spin vector $\boldsymbol{s}_2$, clockwise for $\boldsymbol{s}_1$.

If the second $\pi/2$ pulse would be irradiated at the points where both vectors are in phase, one either observes a spin transition for both ions, if the vectors are back at the start or neither of the ions if the vectors point to the left. These cases relate to being in phase with the microwave drive or out of phase. If the ideal case assumption was valid, this would result in a 0% to 100% modulation for either ion, only depending on the phase relative to the drive.

However, due to magnetic field fluctuations, such a measurement is only possible for extremely short evolution times, as any tiny change of the magnetic field results in a loss of coherence of our system with respect to the external drive of roughly 112 GHz. This can be easily understood, as even for the shortest evolution time used in this work of $\tau_{\text{evol}} = 100\,\text{ms}$, a $\pm 4 \times 10^{-11}$ relative change of the magnetic field between the pulses already corresponds to a change of $\pm 180^\circ$ between a spin vector and the drive. On average over many such cycles, this would therefore simply yield a 50% spinflip probability. Furthermore, it can also be considered that the detuning between drive and Larmor frequency is different for each irradiation due to the limited magnetic field resolution. Therefore, the phase between drive and a single spin vector is random for the second pulse. Both effects lead to an average of 50% spinflip rate.

The first generalization that has to be included in these considerations is therefore the magnetic field fluctuation. If the co-rotating frame is defined with a fixed drive frequency initially, but changes now occur in the magnetic field, the spin vectors rotate with a slightly different frequency. Effectively, this can be understood as their relative detuning changing, and, depending on the sign of the magnetic field change, one of the spin vectors will rotate faster, the other slower, both losing coherence to the drive. This is the regime, where an average of 50% spin transition rate is measured for each of the ions independent of the evolution time.

While such fluctuations affect the drive with respect to the individual frequencies in full, the relation between the two vectors is only affected by their differential change. As the frequency difference is only $\Delta\nu_L \approx 758\,\text{Hz}$, such fluctuations are strongly suppressed by a factor of $\Delta\nu_L/\nu_L \approx 7 \times 10^{-9}$ when compared to the full Larmor frequency $\nu_L \approx 112\,\text{GHz}$. This means, that the phase of the ions with respect to each other is to a large extend independent of such fluctuations. Now, what does the simultaneous consideration of the ions implicate for the irradiation of the second $\pi/2$ pulse?

Let us again assume that the pulse is irradiated when both spin vectors are in phase with each other and that effects stemming from the detuning of the drive can still be neglected for this qualitative explanation. Both spin vectors are now affected identically by the external drive. However, their **common** behaviour is depending on the relative phase of the spin vectors with respect to the drive. Let us consider the crucial idea of this measurement scheme: What is the probability for both spins to behave the same; meaning that both **or** neither undergo a spin transition.

The minimum probability is reached, when neither spin is affected at all. This occurs, when both spin vectors are aligned parallel or anti-parallel with the drive, keeping both in the equatorial plane[a]. This means, that the probability for them to behave identically is 50%, as the probability for a spin transition to occur for either ion is left at 50%. (Fig. 7.2, (C) and (D)).

The maximum probability is reached, when the drive is oriented perpendicular with the spin vectors and both end up in the *spin-up* state (Fig. 7.2, (A)). Furthermore, one also observes common behaviour when their phase relative to the drive is 180° different, which results with both ions again in the *spin-down* state (Fig. 7.2, (B)). The probability to observe a common behaviour in both cases is then 100%.

However, as the phase of the drive has to be assumed to be completely random with respect to the spins, the discussed cases of Fig. 7.2, (A)-(D) have to be averaged and consequently a probability of 75% for a common behaviour is achieved when both spins are in phase with each other.

Similarly, the cases where the phase difference between the spin vectors is 180° at the time of the second pulse can be considered to average to a 25 % probability of common behaviour. Consequently, as the relative phase of the ions to each other is modulated by $\Delta\nu_L$, the examined correlation will vary between 25% and 75% over time, under the assumption that the individual coherence between ions and drive is lost, but the relative coherence between the ions is kept.

Let us now examine, how these considerations can be expressed mathematically. To this end, the case where both spins are initialized in the *spin-down* state is examined again. Once a $\pi/2$ pulse pulse has been calibrated (see section 6.3.3) to achieve a 50 % spinflip probability, an evolution time τ_{evol} larger than 0 must exist, after which a second, identical pulse is able to reach 100% spinflip probability. When the detuning $\delta_i = \omega_{L,i} - \omega_{\mathrm{RF}}$ of applied drive with respect to the Larmor frequencies of both ions is now considered, a 100% rate cannot be obtained for either ion with a single pulse, which is effectively what a zero evolution time would implicate. This can be understood when again considering the rotation of the spin vectors on the Bloch sphere. The actual axis of rotation is now defined by the effective magnetic field vector, given by the linear combination of applied drive magnetic field B_{RF} and the detuning δ_i for each spin vector. Due to the tilt, the rotation of the spin vector on the sphere does not pass through the upper pole,

---

[a] The torque on the spin vectors is given by the cross product of effective magnetic field and spin vector, when neglecting the detuning this results in a rotation around the applied drive.

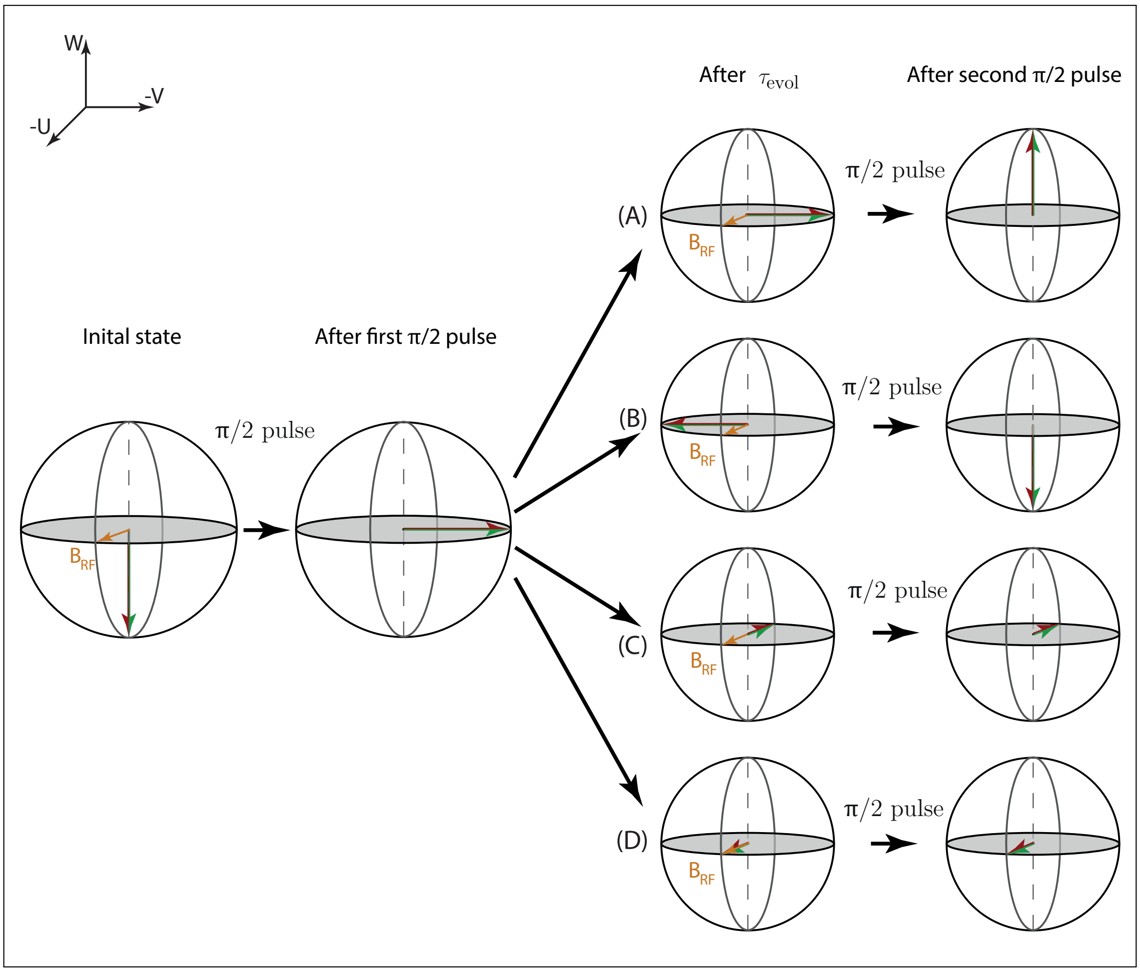

Figure 7.2: Illustration of selected cases before the second $\pi/2$ pulse. For the four discussed cases, where the spin vectors are in phase with respect to each other, possible orientations with respect to the drive are shown. The detuning of the applied drive is neglected in this simplified representation. The coincidental behaviour (both spins behaving the same way) is found to be between 50% and 100% and will average to 75%. Figure adapted from T. Sailer et al., submitted 2021 [37].

therefore not allowing to reach a 100% transition probability. Furthermore, an initial phase difference is accumulated, since the spin vectors pass through different points in the equatorial plane as illustrated in Fig. 7.3 for the state after a first $\pi/2$ pulse.

When now considering this additional phase due to the detuning, the maximum probability for a spin transition after the second pulse is not reached anymore when the spin vectors are exactly perpendicular to the drive, but rather when both have the inverse phase $\Phi_{0,i}$ with respect to the drive. Additionally, due to the symmetric detuning, these phases are of opposite sign for the two spin vectors, $\Phi_{0,2} = -\Phi_{0,1}$. This maximum and minimum probabilities will however still be reached periodically while the spins change their relative phase with $\Delta\nu_L$.

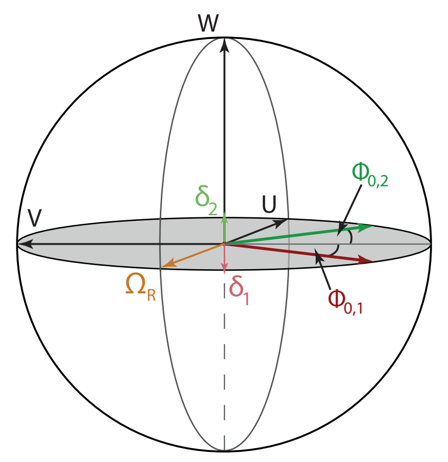

Figure 7.3: Illustration of the spin vectors on the Bloch sphere, with the definition of the vectors $\boldsymbol{s} = (U, V, W)$. An applied drive without detuning results in a counter clockwise rotation of the Bloch vector in the $W - V-$ plane with the Rabi frequency Ω_R. The axis of rotation with a detuning is now given by the linear combination Ω_R and respective detuning δ_i for each spin vector. Here, the spin vectors have originally been pointing down, the shown state is reached after applying a $\pi/2$ pulse with a symmetric detuning δ_i. This results in the additional phases $\Phi_{0,1}$ and $\Phi_{0,2}$ with respect to the V-axis, resulting in a phase difference between the spin vectors.

The probability to find both ions in the *spin-up* state after our measurement cycle with both ions initially in the *spin-down* state is then given as the product of the probabilities for the respective ions as

$$\begin{aligned} P(\uparrow,\uparrow) &= \cos\left(\frac{\omega_{L1} - \omega_{\mathrm{MW}}}{2}\tau_{\mathrm{evol}} + \Phi_{0,1}\right)^2 \cdot \cos\left(\frac{\omega_{L2} - \omega_{\mathrm{MW}}}{2}\tau_{\mathrm{evol}} + \Phi_{0,2}\right)^2 \\ &= \left[\frac{1}{2}\left(\cos\left(\frac{\Delta\omega_L}{2}\tau_{\mathrm{evol}} + \Delta\Phi_0\right) + \cos\left(\frac{\omega_{L1} + \omega_{L2} - 2\omega_{\mathrm{MW}}}{2}\tau_{\mathrm{evol}}\right)\right)\right]^2 , \end{aligned} \tag{7.1}$$

where the initial phase difference $\Delta\Phi_0 = \Phi_{0,2} - \Phi_{0,1}$ and $\Delta\omega_L = \omega_{L2} - \omega_{L1}$ is introduced[a] The phase difference between spin vector and drive follows $\omega_{L,i} - \omega_{\mathrm{MW}}$, where $\omega_{L,i}$ is the Larmor frequency of the individual ions and ω_{MW} is the frequency of the external microwave drive. Similarly, one can write the probability for both ions to remain in the *spin-down* state after completing the measurement cycle. This is given as

$$\begin{aligned} P(\downarrow,\downarrow) &= \sin\left(\frac{\omega_{L1} - \omega_{\mathrm{MW}}}{2}\tau_{\mathrm{evol}} + \Phi_{0,1}\right)^2 \cdot \sin\left(\frac{\omega_{L2} - \omega_{\mathrm{MW}}}{2}\tau_{\mathrm{evol}} + \Phi_{0,2}\right)^2 \\ &= \left[\frac{1}{2}\left(\cos\left(\frac{\Delta\omega_L}{2}\tau_{\mathrm{evol}} + \Delta\Phi_0\right) - \cos\left(\frac{\omega_{L1} + \omega_{L2} - 2\omega_{\mathrm{MW}}}{2}\tau_{\mathrm{evol}}\right)\right)\right]^2 . \end{aligned} \tag{7.2}$$

---

[a] This definition keeps the difference frequency positive, when following the index convention of $1 \hat{=}\ {}^{22}\mathrm{Ne}^{9+}$ and index $2 \hat{=}\ {}^{20}\mathrm{Ne}^{9+}$.

As one wants to examine the coincidental case, the sum of these probabilities where both ions are in the same spin state has to be considered. This is given as

$$\begin{aligned} P(t) = P(\downarrow,\downarrow) + P(\uparrow,\uparrow) &= \frac{1}{2}\cos\left(\frac{\Delta\omega_L}{2}\tau_{\mathrm{evol}} + \Delta\Phi_0\right)^2 \\ &\quad + \underbrace{\frac{1}{2}\cos\left(\frac{1}{2}(\omega_{L1} + \omega_{L2} - 2\omega_{\mathrm{MW}})\tau_{\mathrm{evol}}\right)^2}_{1/4} \\ &= \frac{1}{4}\cos(\Delta\omega_L\,\tau_{\mathrm{evol}} + 2\Delta\Phi_0) + \frac{1}{2}, \end{aligned} \tag{7.3}$$

where the term depending on the external microwave drive is assumed to be not coherent anymore. It thus averages to 50% over multiple measurement cycles.

Therefore, each individual ion is expected to exhibit an average spinflip probability of 50%, while the coincidental probability will undergo a modulation from 25% to 75% with the difference of the Larmor frequencies. For zero evolution time one finds the offset phase between the ions to be $2\Delta\Phi_0$, which is twice the acquired phase of each spin vector. This will be discussed in more detail shortly.

The dependency of the probability of coincidental behaviour on the evolution time is the central point of this method and enables the direct measurement of the Larmor frequency difference. Together with the parameters of electron mass m_e, the ion mass m_{ion} and the charges of the ions q_{ion} and electron e, the difference of their g factors Δg can be directly extracted as

$$\begin{aligned} \Delta g &= \frac{g}{\omega_L}\Delta\omega_L \\ &= \frac{2}{\omega_c}\frac{m_e}{m_{\mathrm{ion}}}\frac{q_{\mathrm{ion}}}{e}\Delta\omega_L. \end{aligned} \tag{7.4}$$

As can be seen from this relation, all input parameters to derive Δg are required to about the relative precision of measured frequency difference $\Delta\omega_L$ to not be limiting factors. To achieve a similar relative precision as the theoretical calculation (see Tab. 1.1) of $\frac{\Delta(\Delta g)}{\Delta g} \approx 8 \times 10^{-4}$, which is still a 5×10^{-12} precision relative to the absolute g factor, all parameters are then required to be known to a low 10^{-4} level. This is of no concern and offers the potential to experimentally surpass this precision by several orders of magnitude[a]. The strongly relaxed dependency on external parameters shown here is the second large benefit of this method compared to absolute measurements, other than the

---

[a] The cyclotron frequency can be determined with a precision of some 10^{-10} per cycle. The electron mass is known to about 3×10^{-11}, the atomic mass of ^{20}Ne to about 1×10^{-10}. Note, that only one of the ion masses is required to this precision.

already discussed suppression of magnetic field fluctuations.

7.1.1 Determination of Initial Phase Difference

The initial phase difference $2\Delta\Phi_0$, defined as the phase that would be determined for a zero evolution time using the formula from Eq. (7.3) for the coincidental probability, stems from the different detuning $\delta_i = \omega_{L,i} - \omega_{\mathrm{RF}}$[a] of the irradiated microwave frequency ω_{RF} with respect to the individual Larmor frequencies $\omega_{L,i}$ of the ions. As one can see from the optical Bloch equations, such a detuning will cause a difference of the phase of spin vector with respect to the drive which depends on the sign of the detuning. The equations to describe the evolution of the spin vector (or Bloch vector) $\boldsymbol{s} = (U, V, W)$ on the Bloch sphere as illustrated in Fig. 7.3, where $W = \pm 1$ represents the two states of the system, can be written as [87]

$$\frac{d\boldsymbol{s}}{dt} = \boldsymbol{\Omega} \times \boldsymbol{s}, \tag{7.5}$$

with the torque vector $\boldsymbol{\Omega} = (-\Omega_R, 0, \delta_i)$, where Ω_R is the Rabi frequency due to the applied drive. When starting in the *spin-down* state, $\boldsymbol{s} = (0, 0, -1)$, the time evolution of the Bloch vector can be derived (see Appendix A) to follow

$$U(t,\delta) = \frac{\delta_i \Omega_R}{\tilde{\Omega}_R^2}\left(1 - \cos(\tilde{\Omega}_R t)\right) \tag{7.6a}$$

$$V(t,\delta) = -\frac{\Omega_R}{\tilde{\Omega}_R}\sin(\tilde{\Omega}_R t) \tag{7.6b}$$

$$W(t,\delta) = -1 + \frac{\Omega_R^2}{\tilde{\Omega}_R^2}\left(1 - \cos(\tilde{\Omega}_R t)\right), \tag{7.6c}$$

with the the effective (or generalized) Rabi frequency $\tilde{\Omega}_R = \sqrt{\Omega_R^2 + \delta^2}$. When the applied microwave drive frequency is the mean Larmor frequency of the ions, one can see that the symmetry is broken due to the detuning in the time evolution of $U(t,\delta)$, as it depends on the sign of the detuning $\delta = \pm{}^{\Delta\omega_L}/_2$. The two other coordinates are symmetric in the detuning and not influenced by the sign.

Using the solution to the time evolution of the Bloch vector, the additional phases $\Phi_{0,i}$ accumulated during the first ${}^{\pi}/_{2}$ pulse as shown in Fig. 7.3, can be calculated using the

---

[a] Index 1 $\hat{=}$ ${}^{22}\mathrm{Ne}^{9+}$ and index 2 $\hat{=}$ ${}^{20}\mathrm{Ne}^{9+}$, and $\omega_{L,2} > \omega_{L,1}$, therefore the δ_1 is negative, δ_2 positive.

results of the Rabi frequency determination (see section 6.3.3)[a] as

$$\Phi_{0,1} = \arcsin\left(\frac{U}{V^2+U^2}\right)\frac{180^\circ}{\pi} \tag{7.7}$$

$$= -8.76(10)^\circ \quad \text{and} \tag{7.8}$$

$$\Phi_{0,2} = +8.76(10)^\circ, \tag{7.9}$$

with the error stemming from the uncertainty of the Rabi frequency. The individual phases $\Phi_{0,i}$ are identical to the ones given in Eq. (7.3). Therefore, the complete phase difference one expects for zero evolution time, or as the initial offset, is then $2\Delta\Phi_0 = 2\Phi_{0,2} - 2\Phi_{0,1} = 35.1(2)^\circ$.

Another consideration can be made using the Rabi formula for the spin transition probability. When irradiating a microwave drive, the probability $P(t)$ to observe a spin transition follows

$$P(t) = \frac{\Omega_R^2}{\tilde{\Omega}_R^2}\sin^2\left(\frac{\tilde{\Omega}_R}{2}t\right). \tag{7.10}$$

For the parameters used here, a transition probability of $P(2\tau_{\frac{\pi}{2}}) \approx 97.7\,\%$ can be calculated. This is valid for both ions, while $\tilde{P}(2\tau_{\frac{\pi}{2}}) = 1 - P(2\tau_{\frac{\pi}{2}})$ is the probability for no spinflip to occur for either ion. Note, that it is intentional to not refer to the probability as a π pulse or $P(\tau_\pi)$. Due to the definition of a $\pi/2$ pulse to achieve a 50 % probability despite the detuning, a single pulse of twice this length does not achieve 100 % spinflip probability. Finally, as a fixed detuning has been used in this case, the fitting function as derived in Eq. (7.3) has to be revisited. The averaging of the cosine to $\frac{1}{2}$ is now no longer valid, as one assumes to irradiate exactly the mean Larmor frequency and $\tau_{\text{evol}} = 0$. Instead, it is found to be $\cos\left(\frac{1}{2}(\omega_{L1} + \omega_{L2} - 2\omega_{\text{MW}})\tau_{\text{evol}}\right)^2 = 1$. Therefore, from Eq. (7.3) it directly follows that

$$P(\uparrow,\uparrow) + P(\downarrow,\downarrow) = \frac{1}{4}\cos(2\Delta\Phi_0) + \frac{3}{4}. \tag{7.11}$$

Furthermore, the same probability can be given by using Eq. (7.10) to calculate the probability to find both in the *spin-up* state, $P(2\tau_{\frac{\pi}{2}})^2$ and the inverse, where both are still in the *spin-down* state, $\tilde{P}(2\tau_{\frac{\pi}{2}})^2$. This can then be written as

$$P(\uparrow,\uparrow) + P(\downarrow,\downarrow) = P(2\tau_{\frac{\pi}{2}})^2 + \tilde{P}(2\tau_{\frac{\pi}{2}})^2. \tag{7.12}$$

---

[a] $\Omega_R = 2\pi \cdot 2465(15)\,\text{Hz}$, $\tau_{\frac{\pi}{2}} = 101.1\,\mu\text{s}$

Combining these equations, it can be determined that the phase one would determine when applying the initially derived fitting function as given in Eq. (7.3) is

$$2\Delta\Phi_0 = \arccos\left(4\left(P(2\tau_{\frac{\pi}{2}})^2 + \tilde{P}(2\tau_{\frac{\pi}{2}})^2 - \frac{3}{4}\right)\right)\frac{180^\circ}{\pi} \tag{7.13a}$$

$$= 35.1(2)^\circ, \tag{7.13b}$$

which is consistent with the calculations using the solutions to the optical Bloch equations with detuning. The uncertainty is again related to the uncertainty of the determined Rabi frequency.

Finally, one can consider magnetic field fluctuations and drifts during the evolution time, effectively changing the detuning and the behaviour of the spins during their evolution. To this end, the complete measurement procedure has been simulated numerically with the inclusion of such fluctuations, using the solution of the optical Bloch equations for arbitrary initial states, as derived in the Appendix A. There are two different effects that have to be considered for such a simulation. First, as only a double-dip measurement is used to determine the cyclotron frequency, and the magnetic field is only predicted for the subsequent cycle, this results in a relative uncertainty of about 3×10^{-9} for the momentary magnetic field at the time of the Ramsey measurement. This uncertainty is the standard deviation between subsequent measurements of the cyclotron frequency. The drive frequency is then adjusted accordingly to the measured magnetic field each cycle. This adjustment translates into a jitter of the detuning of about 330 Hz, which is comparable to the detuning of $\delta \approx 380$ Hz. Averaging over these different detunings for many cycles however still produces the identical result for the predicted initial phase within its uncertainty, as determined by the numerical result. Furthermore, only a small reduction of modulated probability amplitude $\tilde{A}$ can be observed, given as $\tilde{A} = 0.248(2)$. The second possible effect is a change of detuning between the two pulses due to a magnetic field drift in between. A limit on such fluctuations can be placed from subsequent PnA measurements, with a standard deviation between two subsequent shots of about 3×10^{-10}. As this is measured on longer time-scales however ($\approx$ 8 s), the effect during the evolution times of this measurement is likely much smaller. However, allowing such fluctuations to occur between the pulses does on average not produce an observable difference.

The additional phase accumulated during the two pulses, extracted from these numerical simulations can be given as

$$2\Delta\Phi_{0,\mathrm{sim}} = 35(2)^\circ, \tag{7.14}$$

where the uncertainty is the maximum observed deviation of several numerical iterations from the mean value with reasonable input parameters. These include different magnetic field fluctuations as well as the uncertainty of the Rabi frequency.
As all considerations have shown to yield consistent results, the initial phase is used for the evaluation of the frequency difference. However, to not over define the initial phase based upon this simulation and the idealized models, and avoid a potential error due to an unconsidered effect, the phase is only included with a conservative uncertainty estimation of twice the observed deviations of the numerical approach. This factor is meant to account for possible effects such as an asymmetric detuning due to a systematic shift in the magnetic field determination or drifts of the Rabi frequency during the measurement and could likely be reduced for future measurements. The phase is the used in the evaluation as

$$2\Delta\Phi_{0,\mathrm{eval}} = 35(5)^{\circ} \tag{7.15}$$

for the evaluation of the Larmor frequency difference.

7.2 Data Evaluation

The measurement has been performed for five different sets of evolution times, for which at least two have always been measured interleaved, with their order randomly mixed. Therefore, any unforeseen effect on the expected modulation would be observable in at least two separate data sets. Each set of evolution times consists of six discrete times, equally spaced to cover a full period of the expected Larmor frequency difference. Additionally, each of the six times within the set is seeded by a uniform random distribution of ±30 μs, which ensures an averaging of potential fast (unexpected) oscillations on timescales of the irradiated microwave frequency.
The effect on the visibility of the expected modulation of the probability of common behaviour when ignoring and simply averaging over this artificial jitter could be neglected, as it only amounts to a relative change of at most 0.2% of the expected probability modulation amplitude. However, by performing a Maximum-Likelihood fit to the observed modulation, each data point is taken into account corresponding to its exact evolution time already.
The probability to observe a coincidental behaviour depending on the evolution time τ_{evol} is thus evaluated by fitting

$$P(\tau_{\mathrm{evol}}) = \tilde{A} \cdot \cos(\omega_{\mathrm{guess}} \cdot \tau_{\mathrm{evol}} + \Phi_{\mathrm{fit}}) + 0.5, \tag{7.16}$$

where ω_{guess} is a fixed initial guess of the difference frequency. The parameter $\tilde{A}$ is the modulation amplitude and Φ_{fit} is the combined phase, consisting of the initial phase difference and the extracted phase required to match the input frequency guess to the data. While one is ultimately interested in the difference frequency, keeping it fixed in this fit and only determining the phase instead, reduces the amount of free parameters and results in a more stable fit. After thus determining the phase for each evolution time, one is left with the task of unwrapping the total accumulated phase, each given as $\Phi(\tau_{\text{evol}})_{\text{total}} = 2\pi\omega_{\text{guess}} \cdot \tau_{\text{evol}} + \Phi_{\text{fit}}$. The smallest evolution time of $\tau_{\text{evol}} = 100\,\text{ms}$ is chosen such that an error modulo 2π during the unwrapping due to a wrong frequency guess is extremely unrealistic, given the theoretical prediction with an accuracy of 600 mHz for the difference frequency. Therefore, the frequency guess used for fitting would have to be wrong by about $8\,\sigma$ to allow for such an error and becomes even less likely when taking all additional evolution times into account.
The amplitude of the modulation is left as a free fitting parameter to facilitate the determination of the degree of coherence. Therefore, the extracted amplitude is a direct indication of how well the cancellation of the magnetic field fluctuations work at each evolution time. As the coherence of the spins can still be observed even for the longest measured evolution time, the amplitude could be kept fixed to 25 %. However, allowing it as a free parameter achieves a more stable fit. The determined phases have been observed to consistent in both, value and uncertainty for fits performed with either fixed or free amplitude.

7.2.1 Results & Discussion

The total accumulated phases $\Phi(\tau_{\text{evol}})_{\text{total}}$ have been determined as shown in the upper six insets of Fig. 7.4, using $\omega_{\text{guess}} = 2\pi \cdot 758.8\,\text{Hz}$. To determine the Larmor frequency difference, the unwrapped phases of the four main measurements (four insets in Fig. 7.4 not highlighted in grey) that all have been performed with a separation distance $d_{\text{sep}} = 411(11)\,\mu\text{m}$, as well as the initial phase are used. The result of a weighted linear least-square fit is corrected for the systematic shift of 6×10^{-13} (see section 5.7.1). The grey highlighted measurements in Fig. 7.4 have been performed at different separation distances and are not used for the determination of the frequency. The phases determined from these two measurements are corrected for their respective systematic shifts of 2×10^{-13} for $d_{\text{sep}} = 340\,\mu\text{m}$ and 1×10^{-12} for $d_{\text{sep}} = 470\,\mu\text{m}$ and are included in the lower part of Fig. 7.4, where the residual of each phase respect to the determined Larmor frequency difference is shown. The statistical confidence interval (red shaded area) is determined as a combination of the opposing 1σ intervals of initial phase and frequency. For the lower phase, the larger frequency is shown, and vice versa, which yields the largest possible frequency uncertainty. Both of the measurements performed at different separation distances are within 1σ of the combined statistical uncertainty. Here, especially the agreement of the phase determined for the evolution time of 2.2 s, measured at a separation distance of $d_{\text{sep}} = 340\ \mu\text{m}$ has to be highlighted. With a systematic correction of only 2×10^{-13} and a similar statistical resolution, the agreement of this phase yields the single most stringent performance test of this measurement. Combined with the agreement of the phase determined for the larger separation distance of $d_{\text{sep}} = 470\ \mu\text{m}$, both with the fit and the phase determined at a different radius, the systematic treatment is experimentally verified.

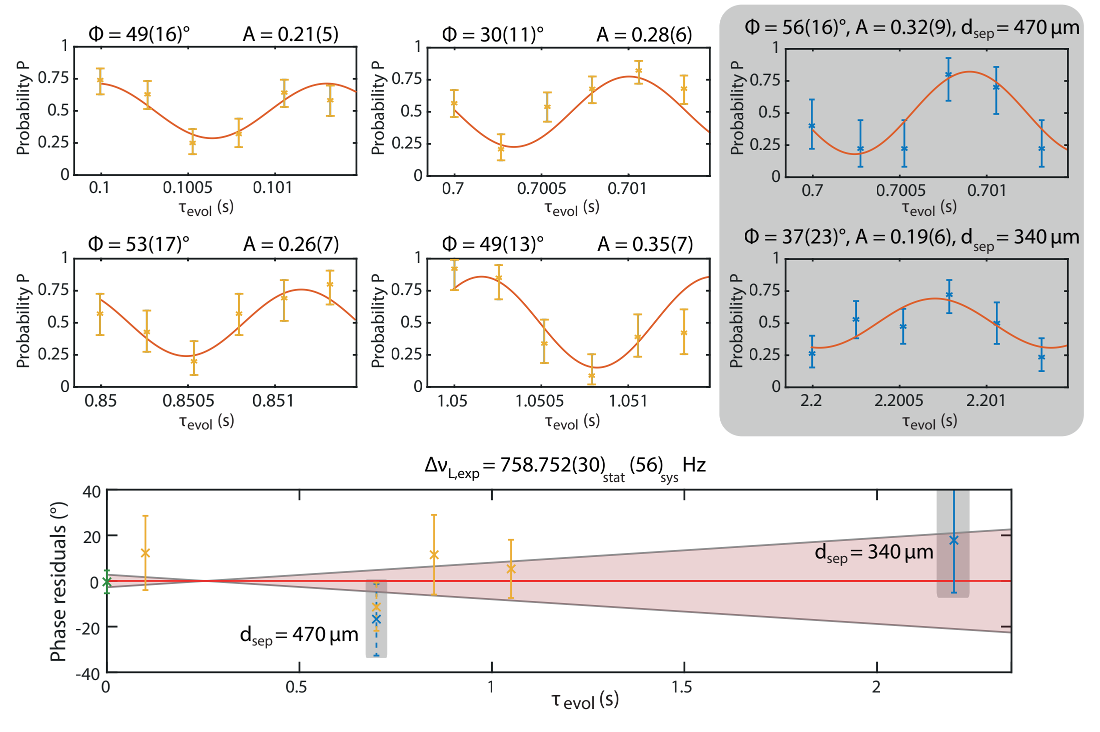

Figure 7.4: The top six insets show the individual measurements for different τ_{evol} and separation distances. The measurements highlighted in grey are for systematic analysis only and did not contribute to the statistical result. The bottom part shows the residuals, including the initial phase (green), with respect to the corrected final frequency. The confidence interval (red shaded area) shows the statistical uncertainty only. Figure taken from T. Sailer et al., submitted 2021 [37].

Furthermore, the initial phase can again be verified using the measured phases directly. To produce the most stringent result, all measured phases are used, including the ones performed with different separation distances after being corrected for their respective systematic shifts. The initial phase, now determined by performing a linear fit to all accumulated phases $\Phi(\tau_{\mathrm{evol}})_{\mathrm{total}}$ yields

$$2\Delta\Phi_{0,\mathrm{exp}} = 33(11)^{\circ}, \tag{7.17}$$

which is consistent with the numerical result derived before.
The extracted frequency difference is $\Delta\nu_L = 758.752(30)_{stat}(56)_{sys}$ Hz, which includes a 5×10^{-13} systematic uncertainty relative to the full Larmor frequency. The average magnetic field during the complete measurement campaign is taken to translate this into a difference of g factors. Generally, this is not quite correct, as each individual measurement would have to be corrected for the current magnetic field. However, with a relative difference between minimum and maximum of the magnetic field during this measurement of only 5×10^{-7} (see App. 8.3.1), the related change of the Larmor frequency difference is of only 380 µHz (or 3×10^{-15} in terms of relative precision) and can be completely neglected here.
Finally, using Eq. (7.4), the g-factor difference can be derived as

$$\boxed{\begin{aligned}\Delta g_{\mathrm{exp}} &= 13.475\,24(53)_{\mathrm{exp}}(99)_{\mathrm{sys}} \times 10^{-9}\\ \Delta g_{\mathrm{theo}} &= 13.474(11)_{\mathrm{FNS}} \times 10^{-9} \quad [36, 37],\end{aligned}}$$

which corresponds to about a two orders of magnitude improved precision compared to the current best isotope difference measurement for g factors [34] and yields the most precise difference of g factors measured to date. The final result of Δg is in excellent agreement with the theoretical value, which is limited in precision by the uncertainty of the charge radius difference due to the finite nuclear size (FNS) correction. Furthermore, the observed amplitudes are all within the 1σ range, except for $\tau_{evol} = 1.05$ s. As the amplitude here is slightly more than 1σ above the expected amplitude, full coherence can still be assumed. As even the amplitude for $\tau_{evol} = 2.2$ s is still within the expected range, a high degree of coherence of the spin vectors even for several seconds of evolution time has therefore been shown and achieved. The initially assumed coherence of the spin states has therefore been proven to be correct.

7.2.2 Nuclear Charge Radii and Differences

The uncertainty of the theoretical value of Δg is dominated by the uncertainty of the charge radius difference, with the next uncertainties stemming from nuclear polarization and deformation effects being two orders of magnitude smaller. Thus, when trusting the theoretical prediction, the charge radius difference $\delta\langle r^2\rangle^{1/2}$ of $^{20}\mathrm{Ne}^{9+}$ and $^{22}\mathrm{Ne}^{9+}$ can be improved by using the measured value of Δg as an input instead. This yields

$$\boxed{\begin{aligned}\delta\langle r^2\rangle^{1/2}_{\mathrm{exp}} &= 0.0533(4)\ \mathrm{fm}\ [37]\\ \delta\langle r^2\rangle^{1/2}_{\mathrm{lit}} &= 0.0530(34)\ \mathrm{fm}\ [33],\end{aligned}}$$

almost an order of magnitude improvement in precision for the difference of these charge radii.

The result of this measurement, applied to derive charge radius differences, can now be used as an additional input parameter for the benchmarking of theoretical calculations required for the determination of charge radii from optical spectroscopy. Here, the main uncertainty typically rests upon the determination of the field-shift factor (FSF) [88], which, despite its uncertainty already being improved via the calibration of independently measured radii, is still about an order of magnitude above the statistical uncertainty [31] for every system heavier than boron [89]. The FSF provides a translation from the spectroscopically measured frequency shift of transitions in different isotopes to a charge radius difference. This field shift is further convoluted with the mass shift, which also results in a change of the transition frequencies due to the different masses of the involved isotopes. To extract a radius difference, this approach therefore requires a calibration of the scaling of the observed frequency shift over multiple isotopes, typically performed by a King plot analysis [31].

Depending on the chosen charge distribution model, from two parameter Fermi distribution, to Barrett radii [90], Barrett-equivalent radii [91] or a simple homogeneous charged sphere model, the expressions for the radii can vastly differ. This model dependency is tackled in several different approaches. One example is translating the Barrett radii, measured for muonic systems, to an electronic RMS value using an empirical formula, modelled to fit available data over a large range of Z [92]. This is especially critical, as measurements performed on muonic atoms provide several, if not most, of the most precise radii currently available [33, 91].

For the FNS correction to the g factor, which ultimately allows this determination of the charge radius difference from a Δg measurement, a translation from the two parameter Fermi model to express the moments of a homogeneously charged sphere model [93] or the direct RMS values can be used. The comparison and agreement of this result with the literature value for the neon isotope charge radius difference, derived from measurements of muonic systems [33], is therefore an important test for the agreement of the different models applied to perform such conversions. Especially the translation from Barrett to RMS values is almost exclusively performed in [33, 92]. This work established the direct comparison between muonic and electronic radii, widely used nowadays with well over 1000 citations. However, while this translation of models seems to be fine in general, after spending a lot of time investigating these dependencies on underlying models and the connection to muonic and optical spectroscopy, I would still encourage to proceed with caution if these radii, especially absolute radii, are of critical importance to future measurements.

This holds at least true for cases where further analysis has been applied to decrease systematic uncertainties. For example, the original publication cited by Angeli and Marinova for the charge radius difference of ^{92}Mo versus ^{100}Mo states a measured value of $\delta\langle r^2\rangle = 1.139(39)\,\mathrm{fm}^2$ [94] limited by the (systematic!) uncertainty of the FSF. This uncertainty had already been deduced using a King plot analysis of all experimental data, combined with the muonic values as calibration parameters in the original publication. Further analysis and a recalculation of the FSF performed by Angeli and Marinova now yields the absolute radii of the isotopes and their differential uncertainty such that $\delta\langle r^2\rangle = 1.154(1)\,\mathrm{fm}^2$ [33]. I did not manage to follow or reproduce this derivation and, more importantly, cannot find an argument for the significantly decreased uncertainty. Therefore, the source material for the tabulated values should at least be confirmed to be of similar precision before these radii and their mostly superior precision with respect to other tabulated values, for example [91], are used.

7.2.3 The Search for New Physics

As the theoretical value of the g-factor difference has been derived within the physics of the Standard Model, the agreement with the experimental result can also be applied to set limits on physics beyond the Standard Model instead. One theory, predicting possible new physics (NP), is based on the mixing of a new scalar boson, the relaxion, with the Higgs boson via the Higgs portal [95, 96]. This boson could potentially mediate an interaction between electrons and nucleons. Therefore, the isotope shift provides a sensitive probe to investigate such an effect due to the change of neutron numbers. With the electron in close proximity of the nucleus, highly-charged ions are especially sensitive to short-range interactions and thus to scenarios with a heavy mass of such a proposed boson. If such a boson was found, it could possibly provide a solution to the hierarchy problem [97].

The interaction between such new bosons and atoms can be expressed via a Yukawa-type potential [98], often referred to as *fifth force*. This potential, seen as arising from the nucleus and acting upon the bound electrons, can be written as [99]

$$V_{\mathrm{HP}}(\boldsymbol{r}) = -\hbar c \frac{y_e y_n}{4\pi} A \frac{e^{-\frac{m_\Phi c}{\hbar}|\boldsymbol{r}|}}{|\boldsymbol{r}|}, \tag{7.18}$$

with the coupling constants γ_e for the electron and γ_n for the nucleons, the nuclear mass number A and the boson mass m_Φ. It can be shown that this results in a dependence of the g factor on the combined coupling constant $\alpha_{\mathrm{HP}} = \frac{\gamma_e \gamma_n}{4\pi}$ [99]. The contribution to the g factor can be written in a simple formula for two regimes, where the boson mass is either much smaller or much larger than the product of proton number, fine-structure constant and the mass of the electron $Z\alpha m_e$ as

$$g_{\mathrm{HP}} = -\frac{4}{3}\alpha_{\mathrm{HP}}\, A\, \frac{(Z\alpha)}{\gamma} \qquad \text{for } m_\phi \ll Z\alpha m_e \quad \text{and} \tag{7.19}$$

$$g_{\mathrm{HP}} = -\frac{4}{3}\alpha_{\mathrm{HP}}\, A\, \frac{(Z\alpha)\,(1+2\gamma)}{\gamma}\left(\frac{m_\phi}{2Z\alpha m_e}\right)^{-2\gamma} \quad \text{for } m_\phi \gg Z\alpha m_e, \tag{7.20}$$

where $\gamma = \sqrt{\kappa^2 - (Z\alpha)^2}$, with the relativistic angular quantum number κ [99]. For light boson masses, the contribution to the g factor is treated by considering the effect of the additional potential on α and calculating the first order correction to the g factor by using the Breit formula (see Eq. (1.3)).

As the agreement between the experimental result and the theoretical prediction has been shown, this allows to derive constraints on the mechanism for such NP as described above. These constraints are expressed as a relation between the combined coupling strengths $\gamma_e \gamma_n$ versus the potential mass of the boson.

The thus excluded area, compared with similar constraints derived from multiple other sources are shown in Fig. 7.5. The other boundaries stem from an isotope shift measurement of hydrogen versus deuterium (H-D 1S-2S, [100]), which represents the most stringent limit in the high boson mass regime. Effects of the Casimir force (CF,[101]) and globular clusters (GC, [102]) are limits derived from astronomical observations, the limit of $(g-2)_e \cdot n$ is derived [103] by a combination of the free electron $(g-2)$ measurement [7], combined with neutron scattering data [104–107]. Finally, the measurements on Ca^+ [103] and Yb^+ [108] are based on isotope shift measurements combined with a King plot analysis. Interestingly, in the Yb^+ measurement a non-linearity in the King plot [108] has been observed and has recently been confirmed in an independent measurement [109]. The cause for this non-linearity is still unresolved. While a NP contribution could potentially be the cause, also general possible problems of the assumption of King plot linearity based on nuclear structure effects are being discussed [110].

Therefore, having an additional method to derive the constraints for NP independently of a King plot linearity is already a benefit by itself. The limits derived here independently confirm the limits given by the hydrogen versus deuterium spectroscopy and exclude this range as a cause for the observed non-linearity in the Yb^+ measurement. Furthermore, the method to predict the isotopic effect on the g-factor difference is able to account for

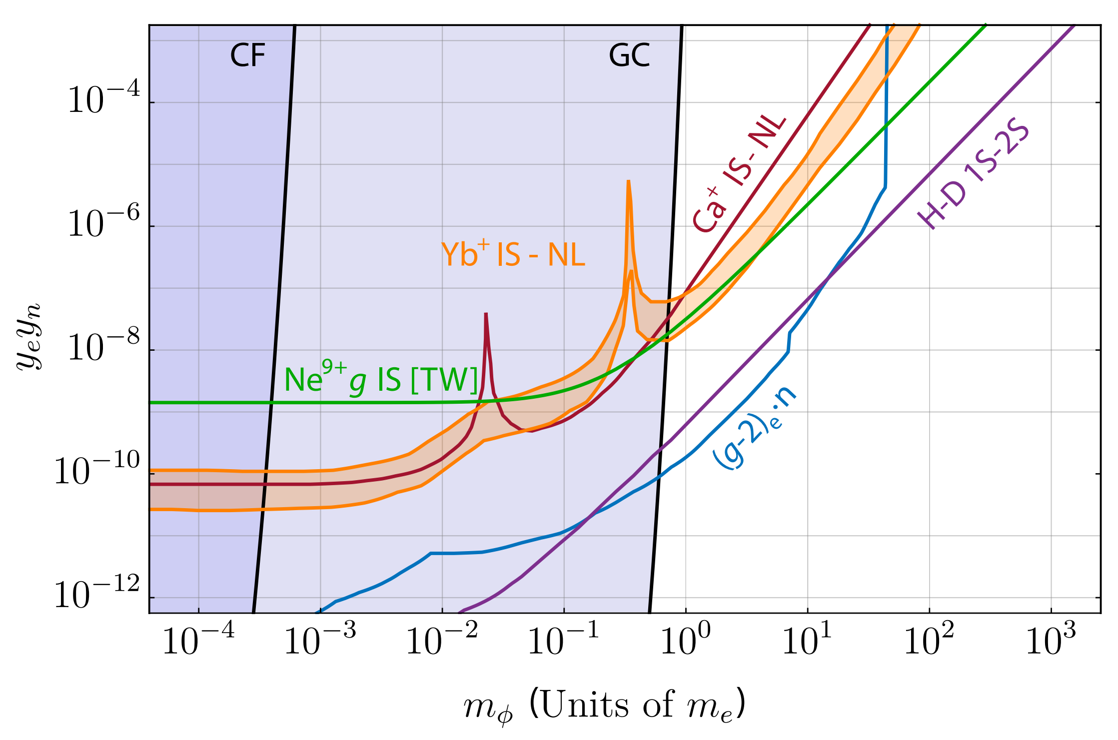

Figure 7.5: Exclusion plot for the relation of interaction strengths $y_e y_n$ versus the potential boson mass $m\Phi$ from the measurement of the Δg isotope shift in neon (green,[TW]). For details see text. Figure taken from T. Sailer et al., submitted 2021 [37].

all nuclear contributions, which might be the cause for the observed non-linearities. As this method remains largely independent of such contributions, this is another benefit when compared to the King-linearity approach [37]. To conclude, it should be noted that the constraints derived here scale directly with the precision of the nuclear charge radii. Thus, a future independent determination of the difference of the nuclear charge radii of the neon isotopes would directly serve to improve the given limits here by up to one order of magnitude, where the experimental precision then becomes the currently limiting factor.

8 Conclusion & Outlook

In this chapter I will provide an overview of all achievements during the course of this thesis. Finally, I will conclude this work by providing an outlook on what can be expected next, with a focus on possible applications of the coupled ion method in the future, combined with potential improvements.

8.1 Setup

The installation of the laser ion source to the setup and the successful injection of $^{9}\mathrm{Be}^{+}$ ions has opened ALPHATRAP to the potential of sympathetic laser cooling. The benefits of that have already been largely discussed in the thesis of Dr. A. Egl [58] and are certain to be an important aspect when considering possible future measurements in the ALPHATRAP setup.
The beamline connecting ALPHATRAP to the HD-EBIT has been designed, built and successfully tested during the course of this thesis. This makes a completely different and vast regime of HCI accessible to ALPHATRAP . Recently, there have already been measurements performed by my colleague J. Morgner on $^{118}\mathrm{Sn}^{49+}$, loaded from the HD-EBIT. This EBIT can be used to produce ions from both, gaseous source matter or solid matter using ovens, leaving the potential measurement cases only limited by the available electron kinetic energy and thus the accessible charge state of the heavy HCI.
In the near future, the HD-EBIT is planned to be replaced by the Hyper-EBIT, which is currently being upgraded for high-voltage operation. The ultimate goal is to reach ionization energies that enable the production of up to hydrogen-like lead to be used for measurements in the ALPHATRAP setup, further pushing the limits of tests for the validity of our theories even in the strongest fields.

8.2 Single Ion *g* Factors

During this work, the *g* factors for three different ion species have been measured. The measurement of the *g* factor of $^{12}\mathrm{C}^{5+}$ (Chap. 4) can be seen as either a verification of the electron mass, albeit with about one order of magnitude less precision than the current literature value [74], or, more importantly, a verification of the performance of the ALPHATRAP experiment. As our previously published results [56, 58], this measurement has been based upon the double-dip technique which has been under investigation for potentially unconsidered systematic effects [72]. At the level of the precision achieved here, similar to that of our previous measurements, no deviation could be observed. This solidifies the trust in the methods used and serves as a benchmark for the performance of the ALPHATRAP experiment.

The measurements of the g factor for the neon isotopes (Chap. 4.2) had multiple purposes. Foremost, these were meant as preparatory measurements for the coupled ions measurement of these isotopes. Secondly, they were the first measurements performed after the phase-sensitive technique of PnA had been implemented at ALPHATRAP . Additionally, the atomic mass of ^{22}Ne had been reported to deviate from the literature value by several sigma [73], which has furthered the interest of this study, as the ion mass can be derived when taking the theoretical value for the g factor as input.
The result of the g-factor measurement of $^{22}\text{Ne}^{9+}$, in combination with the theoretical calculation, has been applied to confirm the AME value [38], decisively excluding such a deviation. Furthermore, the precision of this measurement yields the potential to improve upon the uncertainty of this atomic mass by almost an order of magnitude. However, the measurement campaign for $^{20}\text{Ne}^{9+}$ yielded a deviation of a combined 3σ between experimental result and theory. After an additional thorough investigation of possible sources for this deviation, it was attributed to the input parameter of the atomic mass of ^{20}Ne [38]. This has spiked further interest and independent measurements for the mass of ^{20}Ne are being performed at PENTATRAP [63] at the time of writing the final part of this thesis. First preliminary results [76] of this measurement strongly suggest the atomic mass of ^{20}Ne to be wrong indeed and will likely result in the mass to be reduced by about 3.4σ of its current precision. This update will result in the experimental value for the g factor of Ne20 to agree with theory within 1σ. The agreement of this result gives confidence in both, the underlying theory of both g factors as well as of the newly implemented measurement scheme of PnA and the correct treatment of systematic effects. Due to the agreement, the result of the g factor of $^{20}\text{Ne}^{9+}$ can then be interpreted as a test of BS-QED on the 9×10^{-11} level.

8.3 Coupled Ions

The development and application of the new measurement scheme to directly extract the g-factor difference (Chap. 7.2.1) of coupled ions to unprecedented precision is most certainly the defining result of this thesis, yielding

$$\boxed{\begin{aligned}\Delta g_{\mathrm{exp}} &= 13.475\,24(53)_{\mathrm{exp}}(99)_{\mathrm{sys}} \times 10^{-9} \\ \Delta g_{\mathrm{theo}} &= 13.474(11)_{\mathrm{FNS}} \times 10^{-9} \quad [36, 37].\end{aligned}}$$

Not only has the method been implemented and proven to work, the obtained result confirms the so far unresolved QED contribution to the nuclear recoil and tests it to about 25 % due to the agreement between theory and experiment (see also Tab. 1.1). This agreement serves as a verification of the underlying theory and paves the way to improve upon the precision of similar calculations for even heavier systems.

When taking the theory value as an input instead, it has been shown here that this method can serve to improve the precision of charge radii differences (Chap. 7.2.2) with this independent technique. The charge radius difference of the neon isotopes can thus be improved by one order of magnitude. Furthermore, the agreement with the tabulated values for such differences, which are strongly based on muonic ion spectroscopy, gives credibility to the translation of charge radii measurements performed on muonic systems to their electronic counter parts.

Finally, the agreement of the theoretical calculation with the here obtained result has been applied to constrain parameters of new physics (Chap. 7.2.3). Specifically, such limits are placed upon the parameters in the search for a potential fifth force, based on the Higgs-portal mechanism. While these are currently not the most stringent limits overall, there have been recent observations of a deviation from the King-plot linearity in Yb^{+} [108, 109]. The constraints derived in this thesis clarify, that these deviations are not due to a new physics contribution based upon this present model. Furthermore, the underlying model for the g-factor difference of the 1s electrons takes all nuclear effects, relevant at the current level of precision, into account. Therefore, the result of the measurement performed here can be seen as an unambiguous derivation of the applied bounds, other than from Yb^{+}, where the nuclear deformation might be the reason for the observed non-linearity [111].

8.3.1 Possible Improvements and Outlook

Currently, the achievable precision of this method is limited by the determination of the magnetic field inhomogeneities. While the combined treatment of the related shifts (see section 5.7.1) allows to constrain the systematic effects nicely, the need to shift the equilibrium position of the ions by asymmetric voltages is not yet ideal and there is currently no possibility to reduce the B_1 contribution

Already for the next iteration of modifications to the setup, the implementation of tunable correction coils for B_1 and B_2 is planned. These superconducting coils will be charged in situ to directly compensate and null the inhomogeneities in the centre of the precision trap. This will eliminate the need for a shifted position and therefore minimize possible odd order contributions to the electrostatic potential due to the use of symmetric voltages, reducing the uncertainty for the determination of an absolute value of B_2 due to the C_3 contribution. If extensively tuned, a reduction of the combined shift to below 10 mHz for 500 µm of excitation radii should be entirely possible.

Furthermore, it was shown that smaller separation distances than used for the main result are possible. If the degradation of the signal can be prevented or at least reduced, for example by using negative feedback or even sympathetic laser cooling [44, 112] to lower the temperature of the axial modes, a $d_{\mathrm{sep}} \approx 300\,\mu\mathrm{m}$ should be possible to work with. In combination with smaller inhomogeneities as stated above, this would reduce the total systematic shift of the difference frequency to about 1×10^{-14} in the case of neon.

For identical parameters, the systematic effect for a similar measurement on $^{40}\mathrm{Ca}^{19+}$ and $^{48}\mathrm{Ca}^{19+}$ would only be about a factor of 2 larger. Here, the charge radii would again be the limiting factor, however the QED contribution to the recoil could still be tested to about 10 % [36]. Furthermore, the charge radii of these isotopes are currently considered to be identical within their uncertainty, which could be further explored with such an experiment.

While the ALPHATRAP experiment, equipped with this new technique, can now generally be applied to perform similar measurements to determine the charge radius difference of different isotopes with extreme precision, this cannot be seen as a practical approach for tabulating such values on a large scale. As each difference measurement would require several weeks to months of work, this will only be feasible for systems of particular interest. This could be the case for the isotopes of boron, as the theoretical calculation of the mass shift, the leading contribution of the total isotope shift, has been achieved with a significantly higher precision [89] as for example for neon [31]. The determination of the field shift factor (FSF) has been achieved by comparing the experimental result with the calculation for the mass shift, both obtained within the same work [89]. The therein proposed theoretical approach could be benchmarked by comparing it to an additional independent measurement of the radii difference performed with our method, which could enable further progress towards heavier systems.

It should further be noted, that recent studies have begun to discuss the King approach, specifically in combination with nuclear charge radii [110], where potential problems for the prediction of the FSF cannot be excluded. Our method might become an important tool to resolve such problems by providing a different approach to determine charge radius differences.

Other potential applications include a crucial contribution towards the access of the weighted difference of g factors [113, 114]. To compute such a difference, the g-factor difference of two ions of different nuclear charges Z is required for both their hydrogen-like and lithium-like state. Combined with an absolute g factor of the order of 10^{-11} precision, if ions in the medium Z range were to be chosen, this has the potential to significantly improve upon the fine-structure constant α. However, the required precision of the theory for the absolute g factor has not yet reached this point and will require further work. Similarly, the weighted difference might also allow to put further constraints on new physics, as for example suggested in [99]. Here, several orders of magnitude improvement compared to the limits derived in this work are possible until the theoretical precision would be limited by the uncertainty of the nuclear size correction. Therefore, providing the means of determining the weighted difference experimentally with this method might provide an incentive for theory to focus efforts and advance more quickly.

Lastly, our method could be applied to perform a direct comparison of matter and antimatter, for example with the proton and anti-proton. If compared directly, the expected zero frequency difference of their Larmor frequencies would not be ideal, as the observed coincidental probability of their spins would not undergo any modulation. The method would therefore first have to be proven to work in such a setup, then the missing modulation of the signal would have to be used to infer a zero frequency difference. This is however difficult to implement, as the direct coupling of matter and anti-matter comes with its own complications, e.g. the different sign of the charge.

A substantially more elegant solution to this problem has however already been shown when the charge-to-mass ratio of the anti-proton was compared to that of an H^- ion [115]. Here, the negative hydrogen H^- has been used to circumvent problems related to the different positions within the trap due to the opposite sign of the required trapping voltage if a proton would be used instead.

A similar concept could be applied, when going one step further and coupling the H^- and anti-proton into a magnetron crystal as performed here. This would allow a direct comparison of their magnetic moments, while the observed Larmor frequencies would again differ due to the additional two electrons.

The shielding due to these electrons, described by the dimensionless factor σ_s

$$H = -\boldsymbol{\mu}\boldsymbol{B}(1 - \sigma_s), \tag{8.1}$$

has been improved very recently to $\sigma_s = 17.735\,436(3) \times 10^{-6}$ for an H^- ion [116]. With a proton Larmor frequency of $\nu_{L,p} \approx 80\,\mathrm{MHz}$ in the BASE experiment [117], the Larmor frequency difference would then amount to $\Delta\nu_L \approx 1.4\,\mathrm{kHz}$, which is ideally suited for this method.
The precision of such a measurement would then mostly be limited by the precision of the calculated shielding factor, currently allowing for a potential 3×10^{-12} precision, relative to the proton g factor. This has therefore the potential to achieve similar precision as the comparison of the magnetic moments of electron and positron, yielding a strong test of the charge, parity and time-reversal (CPT) invariance. If this was to be achieved, the precision could be pushed even further by performing a similar measurement with $\bar{H}^+$ versus a proton. This additional difference measurement could serve to circumvent the need of a precise shielding factor by directly comparing two such differences directly.

With these speculative propositions and the conviction that the here developed method will be applied in one form or the other to perform intriguing measurements in the time to come, I conclude this thesis.

List of Publications

1. S. Sturm, I. Arapoglou, A. Egl, M. Höcker, S. Kraemer, **T. Sailer**, B. Tu, A. Weigel, R. Wolf, J. R. Crespo López-Urrutia, and K. Blaum. "The ALPHATRAP experiment", *The European Physical Journal Special Topics*, **227**, 1425-1491, 2019.
   Cited as [18]

2. I. Arapoglou, A. Egl, M. Höcker, **T. Sailer**, B. Tu, A. Weigel, R. Wolf, H. Cakir, V. A. Yerokhin, N. S. Oreshkina, V. A. Agababaev, A. V. Volotka, D. V. Zinenko, D. A. Glazov, Z. Harman, C. H. Keitel, S. Sturm and K. Blaum. "g Factor of Boronlike Argon $^{40}\mathrm{Ar}^{13+}$", *Phys. Rev. Lett.*, **122**, 253001, 2019.
   Cited as [56]

3. A. Egl, I. Arapoglou, M. Höcker, K. König, T. Ratajczyk, **T. Sailer**, B. Tu, A. Weigel, W. Nörtershäuser, K. Blaum and S. Sturm. "Application of the continuous Stern-Gerlach effect for laser spectroscopy of the $^{40}\mathrm{Ar}^{13+}$ fine-structure in a Penning trap", *Phys. Rev. Lett.*, **123**, 123001, 2019.
   Cited as [58]

4. B. Tu, F. Hahne, I. Arapoglou, A. Egl, F. Heiße, M. Höcker, C. M. König, J. Morgner, **T. Sailer**, A. Weigel, R. Wolf and S. Sturm. "Tank-Circuit Assisted Coupling Method for Sympathetic Laser Cooling", *Adv. Quantum Technol.*, **4**: 2100029, 2021.
   Cited as [112]

5. **T. Sailer**, V. Debierre, Z. Harman, F. Heiße, C. M. König, J. Morgner, B. Tu, A. V. Volotka, C. H. Keitel, K. Blaum and S. Sturm, "Direct Bound-Electron g-factor Difference Measurement with Coupled Ions", *Submitted to Nature*, 2021.
   Cited as [37]

Bibliography

[1] A. H. G. Peter, "Dark Matter: A Brief Review", arXiv (2012).

[2] P. J. E. Peebles and B. Ratra, "The cosmological constant and dark energy", Reviews of Modern Physics **75**, 559–606 (2003).

[3] B. Kelvin William Thomson, *Baltimore Lectures on Molecular Dynamics and the Wave Theory of Light* (London : C. J. Clay and sons; Baltimore, Publication agency of the Johns Hopkins university, 1904).

[4] E. Aprile et al., "The XENON1T dark matter experiment", The European Physical Journal C **77**, 881 (2017).

[5] W. E. Lamb and R. C. Retherford, "Fine Structure of the Hydrogen Atom by a Microwave Method", Physical Review **72**, 241–243 (1947).

[6] C. G. Parthey et al., "Improved Measurement of the Hydrogen $1S-2S$ Transition Frequency", Physical Review Letters **107**, 203001 (2011).

[7] D. Hanneke, S. Fogwell, and G. Gabrielse, "New Measurement of the Electron Magnetic Moment and the Fine Structure Constant", Physical Review Letters **100**, 120801 (2008).

[8] T. Aoyama, T. Kinoshita, and M. Nio, "Theory of the Anomalous Magnetic Moment of the Electron", Atoms **7**, 28 (2019).

[9] L. Morel et al., "Determination of the fine-structure constant with an accuracy of 81 parts per trillion", Nature **588**, 61–65 (2020).

[10] H. Müller, "Standard model of particle physics tested by the fine-structure constant", Nature **588**, 37–38 (2020).

[11] R. H. Parker et al., "Measurement of the fine-structure constant as a test of the Standard Model", Science **360**, 191–195 (2018).

[12] B. Abi et al., "Measurement of the Positive Muon Anomalous Magnetic Moment to 0.46 ppm", Physical Review Letters **126**, 141801 (2021).

[13] J. Schwinger, "On Gauge Invariance and Vacuum Polarization", Physical Review **82**, 664–679 (1951).

[14] T. Stöhlker et al., "$1s$ Lamb Shift in Hydrogenlike Uranium Measured on Cooled, Decelerated Ion Beams", Physical Review Letters **85**, 3109–3112 (2000).

[15] J. Ullmann et al., "High precision hyperfine measurements in Bismuth challenge bound-state strong-field QED", Nature Communications **8**, 15484 (2017).

[16] L. V. Skripnikov et al., "New Nuclear Magnetic Moment of ^{209}Bi : Resolving the Bismuth Hyperfine Puzzle", Physical Review Letters **120**, 093001 (2018).

[17] S. Sturm et al., "g Factor of Hydrogenlike $^{28}\text{Si}^{13+}$", Physical Review Letters **107**, 023002 (2011).

[18] S. Sturm et al., "The ALPHATRAP experiment", The European Physical Journal Special Topics **227**, 1425–1491 (2019).

[19] T. Beier, "The g_j factor of a bound electron and the hyperfine structure splitting in hydrogenlike ions", Physics Reports **339**, 79–213 (2000).

[20] B. Sikora, "Quantum field theory of the g-factor of bound systems", PhD thesis (Heidelberg University, June 2018).

[21] H. Cakir, "Quantum Electrodynamic Theory of Few-Electron Highly Charged Ions", PhD thesis (Heidelberg University, 2020).

[22] P. A. M. Dirac, "The quantum theory of the electron", Proceedings of the Royal Society of London. Series A, Containing Papers of a Mathematical and Physical Character **117**, 610–624 (1928).

[23] H. Bethe, "The electromagnetic shift of energy levels", Physical Review **73**, 617–626 (1948).

[24] J. Schwinger, "On quantum-electrodynamics and the magnetic moment of the electron [9]", Physical Review **73**, 416–417 (1948).

[25] T. Aoyama et al., "Tenth-Order QED Contribution to the Electron $g-2$ and an Improved Value of the Fine Structure Constant", Physical Review Letters **109**, 111807 (2012).

[26] B. Odom et al., "New measurement of the electron magnetic moment using a one-electron quantum cyclotron", Physical Review Letters **97**, 6–9 (2006).

[27] W. H. Furry, "On Bound States and Scattering in Positron Theory", Physical Review **81**, 115–124 (1951).

[28] G. Breit, "The Magnetic Moment of the Electron", Nature **122**, 649 (1928).

[29] A. V. Malyshev, D. A. Glazov, and V. M. Shabaev, "QED calculations of the nuclear recoil effect on the bound-electron g factor", arXiv **101**, 012513 (2019).

[30] D. A. Glazov and V. M. Shabaev, "Finite nuclear size correction to the bound-electron g factor in a hydrogenlike atom", Physics Letters, Section A: General, Atomic and Solid State Physics **297**, 408–411 (2002).

[31] B. Ohayon et al., "Isotope shifts in $^{20,22}\text{Ne}$: Precision measurements and global analysis in the framework of intermediate coupling", Physical Review A **99**, 042503 (2019).

[32] G. Fricke and K. Heilig, "Nuclear Charge Radii", edited by H. Schopper, `10.1007/b87879` (2004).

[33] I. Angeli and K. P. Marinova, "Table of experimental nuclear ground state charge radii: An update", Atomic Data and Nuclear Data Tables **99**, 69–95 (2013).

[34] F. Köhler et al., "Isotope dependence of the Zeeman effect in lithium-like calcium", Nature Communications **7**, 10246 (2016).

[35] A. V. Nefiodov, G. Plunien, and G. Soff, "Nuclear-Polarization Correction to the Bound-Electron g Factor in Heavy Hydrogenlike Ions", Physical Review Letters **89**, 081802 (2002).

[36] A. V. Volotka, *Private communication*, 2021.

[37] T. Sailer et al., "Direct Bound-Electron g-factor Difference Measurement with Coupled Ions (*Submitted to Nature*)", (2021).

[38] M. Wang et al., "The AME 2020 atomic mass evaluation (II). Tables, graphs and references", Chinese Physics C **45**, 030003 (2021).

[39] L. S. Brown and G. Gabrielse, "Geonium theory: Physics of a single electron or ion in a Penning trap", Reviews of Modern Physics **58**, 233–311 (1986).

[40] F. G. Major, V. N. Gheorghe, and G. Werth, *Charged Particle Traps* (Springer-Verlag, 2005).

[41] F. T. Köhler, "Bound-Electron g-Factor Measurements for the Determination of the Electron Mass and Isotope Shifts in Highly Charged Ions", PhD thesis (Universität Heidelberg, 2015).

[42] M. Höcker, "Precision Mass Measurements at THe-Trap and the FSU trap", PhD thesis (Universität Heidelberg, 2016).

[43] J. Verdu, "Ultrapräzise Messung des elektronischen g-Faktors in wasserstoffähnlichem Sauerstoff", PhD thesis (Universität Mainz, 2003).

[44] A. Egl, "High-Precision Laser Spectroscopy of the Fine Structure in $^{40}\mathrm{Ar}^{13+}$ at ALPHATRAP", PhD thesis (Universität Heidelberg, Apr. 2020).

[45] J. Ketter et al., "First-order perturbative calculation of the frequency-shifts caused by static cylindrically-symmetric electric and magnetic imperfections of a Penning trap", International Journal of Mass Spectrometry **358**, 1–16 (2014).

[46] K. S. Viswanathan, "The theory of the anharmonic oscillator", Proceedings of the Indian Academy of Sciences - Section A **46**, 203–217 (1957).

[47] S. Rau et al., "Penning trap mass measurements of the deuteron and the HD^+ molecular ion", Nature **585**, 43–47 (2020).

[48] S. Sturm, "The g-factor of the electron bound in $^{28}\mathrm{Si}^{13+}$: The most stringent test of bound-state quantum", Dissertation (Johannes Gutenberg-Universität Mainz, 2012).

[49] A. Weigel, "Detection Electronics Design and First Observation of Bound-Electron Spin Transitions at the ALPHATRAP g-Factor Experiment", PhD thesis (Universität Heidelberg, 2019).

[50] S. Stahl, *Axialfrequenzverstärker mit integriertem Abwärtsmischer AF- DC-b und AF-DC-c*, 2010.

[51] J. B. Johnson, "Thermal Agitation of Electricity in Conductors", Physical Review **32**, 97–109 (1928).

[52] J. G. Ketter, "Theoretical treatment of miscellaneous frequency-shifts in Penning traps with classical perturbation theory", PhD thesis (Universität Heidelberg, 2015).

[53] E. A. Cornell et al., “Mode coupling in a Penning trap: π pulses and a classical avoided crossing”, Physical Review A **41**, 312–315 (1990).

[54] M. Kretzschmar, “A quantum mechanical model of Rabi oscillations between two interacting harmonic oscillator modes and the interconversion of modes in a Penning trap”, AIP Conference Proceedings **457**, 242–251 (1999).

[55] S. Sturm et al., “Phase-Sensitive Cyclotron Frequency Measurements at Ultralow Energies”, Physical Review Letters **107**, 143003 (2011).

[56] I. Arapoglou et al., “g Factor of Boronlike Argon $^{40}\mathrm{Ar}^{13+}$”, Physical Review Letters **122**, 253001 (2019).

[57] Ensinger, *TECAPEEK ELS nanoblack*, Version AC, Ensinger GmbH (Rudolf-Diesel Str. 8, 71154 Nufringen Germany, Feb. 2017).

[58] A. Egl et al., “Application of the Continuous Stern-Gerlach Effect for Laser Spectroscopy of the $^{40}\mathrm{Ar}^{13+}$ Fine Structure in a Penning Trap”, Physical Review Letters **123**, 123001 (2019).

[59] Vespel, DuPont de Nemours, Inc., Wilmington, DE, USA, *DuPont de Nemours*, 2019.

[60] P. Micke et al., “The Heidelberg compact electron beam ion traps”, Review of Scientific Instruments **89**, 063109 (2018).

[61] T. Sailer, *A Laser Ion Source for the Alphatrap Experiment Master Thesis*, 2017.

[62] Litron Lasers, Warwickshire, England, *Litron Nano S*, `https://litron.co.uk/wp-content/uploads/2020/12/Nano-Brochure-December-2020.pdf` (visited on 11/15/2021).

[63] J. Repp et al., “PENTATRAP: a novel cryogenic multi-Penning-trap experiment for high-precision mass measurements on highly charged ions”, Applied Physics B **107**, 983–996 (2012).

[64] QuinStar Technology Inc., Torrance, CA, USA, *Quinstar Broadband detector diode*, `https://quinstar.com/wp-content/uploads/2012/11/QEA_STV01.pdf` (visited on 11/19/2021).

[65] Virginia Diodes Inc., Charlottesville, VA, USA, *WR10AMC-I-M3, Active Multiplier Chain VDI*, `https://www.anritsu.com/en-us/test-measurement/products/mg3690c` (visited on 06/05/2021).

[66] Virginia Diodes Inc., Charlottesville, VA, USA, *WR10AMC-I-M3, Active Multiplier Chain VDI*, `http://www.vadiodes.com` (visited on 06/05/2021).

[67] Mi-Wave, St. Petersburg, FL, USA, *Programmable Rotary Vane Attenuator 511W/387ND*, `https://www.miwv.com/511w-387nd-w-band-wr-10-programmable-rotary-vane-attenuator-frequency-range-75-ghz-110-ghz-attenuation-range-to-70-db/` (visited on 06/05/2021).

[68] S. Sturm et al., “High-precision measurement of the atomic mass of the electron”, Nature **506**, 467–470 (2014).

[69] F. Köhler et al., “The electron mass from g-factor measurements on hydrogen-like carbon $^{12}C^{5+}$”, Journal of Physics B: Atomic, Molecular and Optical Physics **48**, `10.1088/0953-4075/48/14/144032` (2015).

[70] I. Arapoglou, “First measurement of the ground-state *g* factor of boronlike argon $^{40}Ar^{13+}$ in Alphatrap”, PhD thesis (Heidelberg, 2019).

[71] C. Böhm et al., “An ultra-stable voltage source for precision Penning-trap experiments”, Nuclear Instruments and Methods in Physics Research, Section A: Accelerators, Spectrometers, Detectors and Associated Equipment **828**, 125–131 (2016).

[72] S. Rau, “High-precision measurement of the deuteron’s atomic mass”, PhD thesis (Universität Heidelberg, 2020).

[73] T. Segal, “Mass Measurements of Neon Isotopes at THe-Trap”, PhD thesis (Universität Heidelberg, 2019).

[74] E. Tiesinga et al., “CODATA Recommended Values of the Fundamental Physical Constants: 2018”, Journal of Physical and Chemical Reference Data **50**, 033105 (2021).

[75] Edwards, Burgess Hill, England, *STP603 turbomolecular pump*, `https://shop.edwardsvacuum.com/products/yt390z005/view.aspx` (visited on 06/02/2021).

[76] M. Door, *Private communication*, 2021.

[77] J. Ketter et al., “Classical calculation of relativistic frequency-shifts in an ideal Penning trap”, International Journal of Mass Spectrometry **361**, 34–40 (2014).

[78] M. Schuh et al., “Image charge shift in high-precision Penning traps”, Physical Review A **100**, 1–17 (2019).

[79] J. Verdú et al., “Electronic g factor of hydrogenlike oxygen $^{16}O^{7+}$”, Physical Review Letters **92**, 7–10 (2004).

[80] R. J. Hendricks et al., “Laser cooling in the Penning trap: An analytical model for cooling rates in the presence of an axializing field”, Journal of Physics B: Atomic, Molecular and Optical Physics **41**, 2351–2362 (2008).

[81] M. Affolter et al., “Phase-coherent sensing of the center-of-mass motion of trapped-ion crystals”, Physical Review A **102**, 052609 (2020).

[82] S. Rainville, “A Two-Ion Balance for High Precision Mass Spectrometry”, PhD thesis (Massachusetts Institute of Technology, 2003).

[83] S. Rainville, J. K. Thompson, and D. E. Pritchard, “An Ion Balance for Ultra-High-Precision Atomic Mass Measurements”, Science **303**, 334–338 (2004).

[84] J. K. Thompson, “Two-Ion Control and Polarization Forces for Precise Mass Comparisons”, PhD thesis (Massachusetts Institute of Technology, 2003).

[85] E. A. Cornell et al., “Two ions in a Penning trap: Implications for precision mass spectroscopy”, Physical Review A **45**, 3049–3059 (1992).

[86] S. Ulmer, “First Observation of Spin Flips with a Single Proton Stored in a Cryogenic Penning Trap”, PhD thesis (University of Heidelberg, Germany, 2011).

[87] G. W. Drake, *Atomic, Molecular, & Optical Physics Handbook* (American Inst. of Physics, New York, 1996).

[88] J. Li, M. Godefroid, and J. Wang, "Atomic parameters for the $2p^5 3p\ {}^2[3/2]_2$ – $2p^5 3s\ {}^2[3/2]^o_2$ transition of Ne I relevant in nuclear physics", Journal of Physics B: Atomic, Molecular and Optical Physics **49**, 115002 (2016).

[89] B. MaaSS et al., "Nuclear Charge Radii of ^{10,11}B", Physical Review Letters **122**, 182501 (2019).

[90] R. Barrett, "Model-independent parameters of the nuclear charge distribution from muonic X-rays", Physics Letters B **33**, 388–390 (1970).

[91] G. Fricke and K. Heilig, "Nuclear Charge Radii", in *Nuclear Charge Radii*, Vol. 20, edited by H. Schopper, Landolt-Börnstein - Group I Elementary Particles, Nuclei and Atoms (Springer-Verlag, Berlin/Heidelberg, 2004), pp. 1–36.

[92] I. Angeli, "Barrett Moments and *rms* Charge Radii", Acta Physica Hungarica **15**, 87–102 (2002).

[93] V. M. Shabaev, "Finite nuclear size corrections to the energy levels of the multicharged ions", Journal of Physics B: Atomic, Molecular and Optical Physics **26**, 1103–1108 (1993).

[94] F. C. Charlwood et al., "Nuclear charge radii of molybdenum fission fragments", Physics Letters, Section B: Nuclear, Elementary Particle and High-Energy Physics **674**, 23–27 (2009).

[95] C. Englert et al., "Exploring the Higgs portal", Physics Letters, Section B: Nuclear, Elementary Particle and High-Energy Physics **703**, 298–305 (2011).

[96] P. Brax and C. Burrage, "Screening the Higgs portal", Physical Review D **104**, 15011 (2021).

[97] P. W. Graham, D. E. Kaplan, and S. Rajendran, "Cosmological Relaxation of the Electroweak Scale", Physical Review Letters **115**, 221801 (2015).

[98] V. V. Flambaum, A. J. Geddes, and A. V. Viatkina, "Isotope shift, nonlinearity of King plots, and the search for new particles", Physical Review A **97**, 1–12 (2018).

[99] V. Debierre, C. H. Keitel, and Z. Harman, "Fifth-force search with the bound-electron g factor", Physics Letters B **807**, 135527 (2020).

[100] C. Delaunay et al., "Probing new spin-independent interactions through precision spectroscopy in atoms with few electrons", Physical Review D **96**, 115002 (2017).

[101] M. Bordag et al., *Advances in the Casimir effect* (Oxford University Press, 2009).

[102] J. Redondo and G. Raffelt, "Solar constraints on hidden photons re-visited", J. Cosmol. Astropart. Phys. **2013**, 034 (2013).

[103] C. Solaro et al., "Improved Isotope-Shift-Based Bounds on Bosons beyond the Standard Model through Measurements of the ^{2}D$_{3/2}$ - ^{2}D$_{5/2}$ Interval in Ca$^+$", Physical Review Letters **125**, 123003 (2020).

[104] R. Barbieri and T. Ericson, "Evidence against the existence of a low mass scalar boson from neutron-nucleus scattering", Physics Letters B **57**, 270–272 (1975).

[105] H. Leeb and J. Schmiedmayer, "Constraint on hypothetical light interacting bosons from low-energy neutron experiments", Physical Review Letters **68**, 1472–1475 (1992).

[106] Y. N. Pokotilovski, "Constraints on new interactions from neutron scattering experiments", Physics of Atomic Nuclei **69**, 924–931 (2006).

[107] V. V. Nesvizhevsky, G. Pignol, and K. V. Protasov, "Neutron scattering and extra-short-range interactions", Physical Review D **77**, 034020 (2008).

[108] I. Counts et al., "Evidence for Nonlinear Isotope Shift in Yb$^+$ Search for New Boson", Physical Review Letters **125**, 123002 (2020).

[109] K. Ono et al., "Observation of non-linearity of generalized King plot in the search for new boson", arXiv, 1–15 (2021).

[110] R. A. Müller et al., "Nonlinearities of King's plot and their dependence on nuclear radii", Physical Review A **104**, L020802 (2021).

[111] N. L. Figueroa et al., "Precision determination of isotope shifts in ytterbium and implications for new physics", 1–15 (2021).

[112] B. Tu et al., "Tank-Circuit Assisted Coupling Method for Sympathetic Laser Cooling", Advanced Quantum Technologies **4**, 1–9 (2021).

[113] V. M. Shabaev et al., "g-factor of heavy ions: A new access to the fine structure constant", Physical Review Letters **96**, 5–8 (2006).

[114] V. A. Yerokhin et al., "g-Factor of Light Ions for an Improved Determination of the Fine-Structure Constant", Physical Review Letters **116**, 1–5 (2016).

[115] S. Ulmer et al., "High-precision comparison of the antiproton-to-proton charge-to-mass ratio", Nature **524**, 196–199 (2015).

[116] D. Wehrli et al., "QED effects on the nuclear magnetic shielding of ^{3}He", arXiv (2021).

[117] C. Smorra et al., "BASE The Baryon Antibaryon Symmetry Experiment", European Physical Journal: Special Topics **224**, 3055–3108 (2015).

Appendix A: Derivation of Formulas

This appendix is meant to discuss and derive additional formulas that have been used throughout this thesis. These derivation provide further insight and allow to extend ones understanding of the effects (and sometimes approximations) made.

B_1 Positional Shift

This is adapted from [43] to also include the here important magnetron dependency of the B_1 positional shift. For the axial equilibrium position, the net force has to be zero. Therefore, the additional axial force, here stemming from the magnetic moment in a B_1, must be compensated by the electrostatic potential for the ion to experience no force in axial direction, $F_z = 0 = \Delta z(\mu_z B_z) + E_z q$. When using $B_z = B_0 + B_1 z + B_2 z^2$, this leads to

$$\begin{aligned} \mu_z B_1 &= m_\mathrm{ion}\omega_z^2 \Delta z \\ \Rightarrow \Delta z &= \frac{\mu_z B_1}{m_\mathrm{ion}\omega_z^2}, \end{aligned} \tag{8.1}$$

ignoring the B_2 contribution, as $B_2 \ll B_1$. With the definition of the ions magnetic moment (see Eq. (2.18)), neglecting the spin magnetic moment and considering either $\mu_+ \gg \mu_-$ or $\mu_- \gg \mu_+$, this yields

$$\Delta z \approx -\frac{B_1 \omega_\pm}{2\omega_z^2}\frac{q_\mathrm{ion}}{m_\mathrm{ion}} r_\pm^2 \tag{8.2}$$

Finally, using the substitution $B_0 = \omega_c \frac{m_\mathrm{ion}}{q_\mathrm{ion}}$ this can be written as

$$\Delta z \approx -\frac{B_1}{2B_0}\frac{\omega_c \omega_\pm}{\omega_z^2} r_\pm^2 \tag{8.3}$$

Equations of Motions and Shifts

Here, I will explain the assumptions made to derive the first order frequency shift in the case of the coupled ions. First, it is assumed that the ions have a large magnetron separation while their axial motions are thermalized to 4 K. Furthermore, the cyclotron energy is neglected for this derivation. For two ions in the X-Y plane any placement can be written as

$$d_{\text{sep}} = \sqrt{(x_1 - x_2)^2 + (y_1 - y_2)^2}. \tag{8.4}$$

The repelling Coulomb force in radial direction with $k = \frac{1}{4\pi\epsilon_0}$ is then given as

$$F_c = k\frac{q_1 q_2}{d_{\text{sep}}^2} = k\frac{q^2}{d_{\text{sep}}^2}, \tag{8.5}$$

where $q_1 = q_2$ is assumed. If one further considers the thermal axial amplitudes, small compared to d_{sep} for both ions with $\hat{z}_i \approx 18\,\mu\text{m}$, the force in axial direction can be written as

$$F_z = kq^2 \frac{z_1 - z_2}{\sqrt{d_{\text{sep}}^2 + (z_1 - z_2)^2}^3} \tag{8.6}$$

$$\approx k\frac{q^2}{d_{\text{sep}}^3}(z_1 - z_2). \tag{8.7}$$

This additional axial force modifies the motion of the axial harmonic oscillation as

$$\ddot{z}_1 = -\omega_{z1}^2 z_1 + \frac{F_z}{m_1} = -\omega_{z_1}^2 z_1 + \frac{kq^2}{m_1 d_{\text{sep}}^3}(z_1 - z_2) \tag{8.8}$$

$$\ddot{z}_2 = -\omega_{z2}^2 z_2 + \frac{F_z}{m_2} = -\omega_{z_2}^2 z_2 + \frac{kq^2}{m_2 d_{\text{sep}}^3}(z_2 - z_1) \tag{8.9}$$

with the added, axial position dependent-Coulomb force. Due to the large axial frequency difference of the ions, the respective resonant part of excitation exerted onto each other is far detuned and can thus be neglected[a]. The altered axial frequency can now be defined as

$$\tilde{\omega}_{z,i} = \sqrt{\omega_{z,i}^2 - \frac{kq^2}{m_i d_{\text{sep}}^3}} \approx \omega_{z,i} - \frac{kq^2}{2m_i d_{\text{sep}}^3 \omega_{z,i}}. \tag{8.10}$$

---

[a] One ion drives the axial mode of the other with its own axial frequency. As the frequencies of their axial modes are very different, this excitation is about 30 kHz off resonance and can be neglected compared to the stronger constant Coulomb repulsion.

The axial frequency shift for the individual ions i in a coupled state is thus

$$\Delta\omega_{z,i} \approx -\frac{kq^2}{2m_i d_{\mathrm{sep}}^3 \omega_{z,i}}. \tag{8.11}$$

It can be directly seen, that any frequency shift will be towards a smaller axial frequencies and scales inversely with d_{sep}^3 and the ions mass. This shift will also be slightly corrected for higher order contributions as well as the neglected weak perturbation due to the coupling to the other ion (see Eq. (5.11)) – but using it for the general work with the coupled ions this turns out to be a decent approximation. Furthermore, this approximation holds true as long as $\hat{z} \ll d_{\mathrm{sep}}$ and $\Omega_z \ll \Delta\omega_z$, which thus has to be confirmed for the specific ions it is to be applied for.

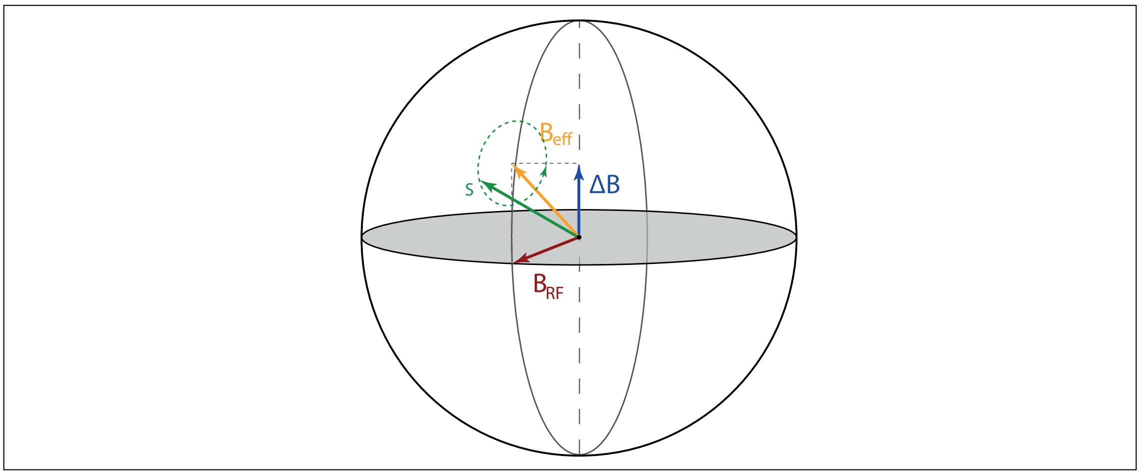

Figure 8.1: The rotation of the spin vector $\boldsymbol{s}$ around the effective magnetic field vector $\boldsymbol{B}_{\text{eff}}$ is illustrated.

Optical Bloch Equations: The Rotational Matrix

The solution of the optical Bloch equations for a system of arbitrary initial state is helpful to simulate the complete measurement sequence for the spin vectors. As such a solution has been difficult to find in literature, this section might proof useful to future students. First, the Bloch sphere is again examined. Here, the rotational axis is given by the effective magnetic field vector $\boldsymbol{B}_{\text{eff}}$, which in the rotating frame of the applied drive is the linear combination of the magnetic field of the applied drive $\boldsymbol{B}_{\text{RF}}$ and the detuning with respect to the Larmor frequency $\boldsymbol{\Delta B}$. The spin vector $\boldsymbol{s}$ will rotate around the effective magnetic field vector as illustrated in Fig. 8.1 The rotational matrix to perform a rotation around an axis defined by the unity vector $\boldsymbol{n} = (n_1, n_2, n_3)$, using the abbreviations $c = \cos\alpha$ and $s = \sin\alpha$ is given as

$$R_n(\alpha) = \begin{pmatrix} n_1^2\,(1-c)+c & n_1 n_2\,(1-c) - n_3 s & n_1 n_3\,(1-c) + n_2 s \\ n_2 n_1\,(1-c) + n_3 s & n_2^2\,(1-c)+c & n_2 n_3\,(1-c) - n_1 s \\ n_3 n_1\,(1-c) - n_2 s & n_3 n_2\,(1-c) + n_1 s & n_3^2\,(1-c)+c \end{pmatrix}. \tag{8.12}$$

In this case, the axis of rotation is defined by the normalized vector $\hat{\boldsymbol{B}}_{\text{eff}} = (-\frac{B_{\text{RF}}}{\beta}; 0; \frac{\Delta B}{\beta})$, where $\beta = \sqrt{B_{\text{RF}}^2 + (\Delta B)^2}$. The rotation matrix, using $1 - \frac{B_{\text{RF}}^2}{\beta^2} = \frac{\Delta B^2}{\beta^2}$ can then be written as

$$R_n(\alpha) = \begin{pmatrix} 1 + \left(\frac{\Delta B}{\beta}\right)^2 (c-1) & -\frac{\Delta B}{\beta} s & \frac{-B_{\text{RF}}\Delta B}{\beta^2}\,(1-c) \\ \frac{\Delta B}{\beta} s & c & \frac{B_{\text{RF}}}{\beta} s \\ \frac{-B_{\text{RF}}\Delta B}{\beta^2}\,(1-c) & -\frac{B_{\text{RF}}}{\beta} s & 1 + \left(\frac{B_{\text{RF}}}{\beta}\right)^2 (c-1) \end{pmatrix}. \tag{8.13}$$

Using the relations

$$\frac{\Delta B}{B_0} = \frac{\delta}{\omega_L} \tag{8.14a}$$

$$\Rightarrow \frac{\Delta B}{\beta} = \frac{\delta}{\sqrt{\Omega_R^2 + \delta^2}} \quad \text{and} \tag{8.14b}$$

$$\frac{B_{\text{RF}}}{B_0} = \frac{\Omega_R}{\omega_L} \tag{8.14c}$$

$$\Rightarrow \frac{B_{\text{RF}}}{\beta} = \frac{\Omega_R}{\sqrt{\Omega_R^2 + \delta^2}}, \tag{8.14d}$$

combined with the normal definition of $\tilde{\Omega}_R = \sqrt{(\Omega_R^2 + \delta^2)}$ this can be written as

$$R_n(\alpha) = \begin{pmatrix} 1 + \frac{\delta^2}{\tilde{\Omega}_R^2}\,(c-1) & -\frac{\delta}{\tilde{\Omega}_R} s & -\frac{\Omega_R}{\tilde{\Omega}_R^2}\delta\,(1-c) \\ \frac{\delta}{\tilde{\Omega}_R} s & c & \frac{\Omega_R}{\tilde{\Omega}_R} s \\ -\frac{\Omega_R}{\tilde{\Omega}_R^2}\delta\,(1-c) & -\frac{\Omega_R}{\tilde{\Omega}_R} s & 1 + \frac{\Omega_R^2}{\tilde{\Omega}_R^2}\,(c-1) \end{pmatrix}. \tag{8.15}$$

The length of the torque vector β defines the rotational speed, which is here just $\tilde{\Omega}_R$. Instead of rotating about a fixed angle α, the rotation can be written in a time dependent form, using $\alpha = \tilde{\Omega}_R t$, where t is the time the microwave drive is irradiated for. For a spin vector initially in the *spin-down* state $s = (0, 0, -1)$, this then leads to the time evolution of the spin vector, given as

$$U(t,\delta) = \frac{\delta_i \Omega_R}{\tilde{\Omega}_R^2}(1 - \cos(\tilde{\Omega}_R t)) \tag{8.16a}$$

$$V(t,\delta) = -\frac{\Omega_R}{\tilde{\Omega}_R}\sin(\tilde{\Omega}_R t) \tag{8.16b}$$

$$W(t,\delta) = -1 + \frac{\Omega_R^2}{\tilde{\Omega}_R^2}(1 - \cos(\tilde{\Omega}_R t)), \tag{8.16c}$$

Appendix B:
Combined Systematic Shifts for the Δg Measurement

This section has originally been compiled by myself as part of the methods section, accompanying the paper submitted concerning the Δg measurement [37]. Large parts are reproduced here without modification, others have only been revised for more clarity or changed where a different notation was chosen to stay consistent throughout this thesis. To clarify the individual radii, the notation $r_\pm$ will be used for magnetron and cyclotron radii of a single ion, whereas the coupled ion magnetron radii will be written as $\boldsymbol{\rho}_1$ and $\boldsymbol{\rho}_2$.

Here, the total systematic shift and the corresponding uncertainty for the specific case of $^{20}\mathrm{Ne}^{9+}$ and $^{22}\mathrm{Ne}^{9+}$ is evaluated. For this approach, only a separation distance and no common mode is considered. For small common mode radii $0 \leq r_{\mathrm{com}} \leq \frac{d_{\mathrm{sep}}}{\sqrt{5}}$, the systematic effects discussed here are actually further reduced [84].

Multiple individual measurements have to be performed with single ions to characterize these frequency shifts and the experimental parameters discussed here. More explanation on the experimental methods used to determine these can be found in [18], the individual frequency shifts are derived in [45]. The electrostatic and magnetic contributions are defined as given in section 2.

First, the two main axial, electrostatic only frequency shifts that depend on the radial amplitudes $r_\pm$ of an ion are given as

$$\left.\frac{\Delta\nu_z}{\nu_z}\right|_{C4} = -\frac{3}{2}\frac{C_4}{C_2 d_{char}^2} r_\pm^2 \tag{9.1}$$

$$\left.\frac{\Delta\nu_z}{\nu_z}\right|_{C3} = \frac{9}{8}\frac{C_3^2}{C_2^2 d_{char}^2} r_\pm^2 . \tag{9.2}$$

If the shift of ν_z is measured to be zero for any radius r_-, these two shifts must cancel (or both be zero) and it can be concluded that $C_4 = \frac{3}{4}\frac{C_3^2}{C_2}$. As it is typically not feasible to tune this for arbitrary radii, especially since higher orders will have to be considered as well for larger radii, a residual shift ϵ_{el,r_-} is introduced, which includes both, the observed residual shift as well as all neglected higher order contributions. This is a relative uncertainty, scaling with r_-^2. Combined, these electrostatic shifts only read

$$\left.\frac{\Delta\nu_z}{\nu_z}\right|_{el} = \frac{9}{8}\frac{C_3^2}{C_2^2 d_{char}^2}r_-^2 - \frac{3}{2}\frac{C_4}{C_2 d_{char}^2}r_-^2. \quad = \epsilon_{el,r_-} \tag{9.3}$$

For cyclotron excitations, the electrostatic contributions are identical to those for the magnetron mode and must therefore also combine to the same ϵ_{el,r_+}, scaling with the cyclotron radius. However, the additional terms that stem from the magnetic field inhomogeneities have to be considered, since they are sizeable only in this mode due to the significantly higher frequency:

$$\begin{aligned}\left.\frac{\Delta\nu_z}{\nu_z}\right|_{B_2} &= \frac{B_2}{4B_0}\frac{\nu_+ + \nu_-}{\nu_+\nu_-}\nu_+ r_+^2 \\ &\approx \frac{B_2}{B_0}\frac{\nu_+^2}{2\nu_z^2}r_+^2\end{aligned} \tag{9.4}$$

$$\begin{aligned}\left.\frac{\Delta\nu_z}{\nu_z}\right|_{B_1,C_3} &= -\frac{3B_1C_3\nu_c\nu_+}{4B_0C_2d_{char}\nu_z^2}r_+^2 \\ &\approx -\frac{3B_1C_3\nu_+^2}{4B_0C_2d_{char}\nu_z^2}r_+^2.\end{aligned} \tag{9.5}$$

Additionally, for large cyclotron excitations the relativistic effect and resulting mass increase has to be considered, also slightly shifting the axial frequency:

$$\left.\frac{\Delta\nu_z}{\nu_z}\right|_{rel.} = -\frac{3B_1C_3\nu_c\nu_+}{4B_0C_2d_{char}\nu_z^2}r_+^2 \tag{9.6}$$

The combined shift depending on magnetic inhomogeneities can be expressed as

$$\left.\frac{\Delta\nu_z}{\nu_z}\right|_{mag} = \left(\frac{B_2}{B_0}\frac{\nu_+^2}{2\nu_z^2} - \frac{3B_1C_3\nu_+^2}{4B_0C_2d_{char}\nu_z^2}\right)r_+^2 = \epsilon_{mag}. \tag{9.7}$$

While the B_1 and B_2 contributions currently cannot be tuned actively (which could be implemented by using active compensation coils [47]), the ion can be slightly shifted from its equilibrium position to a more preferable position along the z-axis to minimize the B_2 coefficient. Doing so, frequency shifts of ν_z close to zero for any cyclotron excitations have been achieved as well, which means these terms have to cancel as well. To allow for another residual error from higher orders, as well as a small residual shift, ϵ_{mag} is chosen to represent these. The observed difference of the frequency shift between cyclotron and magnetron excitations $\epsilon_{\text{mag}} + \epsilon_{el,r_+} - \epsilon_{el,r_-}$ can be used to cancel the identical electric contributions ϵ_{el,r_+} and ϵ_{el,r_-} when measuring at the same radius. If this combined equation is solved for C_3, only the magnetic field dependent terms B_1 and B_2 are left, which is what the Larmor frequency difference is sensitive to:

$$\begin{aligned} C_3 &= \frac{2}{3}\frac{B_2 C_2 d_{char}}{B_1} - \underbrace{\frac{4}{3}\frac{B_0 C_2 d_{char} v_z^2}{B_1 v_+^2 r_+^2}\epsilon_{mag}}_{\xi} \\ &= \frac{2}{3}\frac{B_2 C_2 d_{char}}{B_1} - \xi. \end{aligned} \tag{9.8}$$

This means, that without further measurement it is impossible to discern a C_3 from a B_2 contribution. Now, instead of looking at frequency shifts of individual ions, the effects on coupled ions are considered. Due to their mass difference, the coupled state is not perfectly symmetrical but slightly distorted due to the centrifugal force difference. In the case of the neon isotopes, this leads to a deviation of $\delta_{\text{mag}} = 0.87\%$, with the definition of $\rho_1 = d_{\text{sep}}\frac{(1+\delta_{\text{mag}})}{2}$ and $\rho_2 = d_{\text{sep}}\frac{(1-\delta_{\text{mag}})}{2}$, when choosing ion 1 as $^{22}\text{Ne}^{9+}$ and ion 2 to be $^{20}\text{Ne}^{9+}$. Consequently, the frequency difference $\nu_{L_2} - \nu_{L_1}$ will be positive, as the g factor (and therefore the Larmor frequency) of $^{20}\text{Ne}^{9+}$ is larger than that of $^{22}\text{Ne}^{9+}$. Finally, the axial position shift due to C_3 as given in Eq. (2.13) is considered as a function of the slightly different r_-^2. The shifts of ν_L are to very good approximation only dependent on the absolute magnetic field. The effect of B_1 and all shifts along the z-axis can then be expressed as

$$\left.\frac{\Delta\nu_L}{\nu_L}\right|_{B_1} = \Delta z\frac{B_1}{B_0}. \tag{9.9}$$

The difference of the shift for the individual ions can then be written as

$$\begin{aligned} \left.\frac{\Delta(\Delta\nu_L)}{\nu_L}\right|_{B_1} &= \frac{\Delta\nu_{L_2} - \Delta\nu_{L_1}}{\nu_L} \\ &= (\Delta z_2 - \Delta z_1)\frac{B_1}{B_0} \\ &= \frac{3}{4}\frac{C_3}{C_2}\frac{B_1}{B_0 d_{char}}\left(\rho_2^2 - \rho_1^2\right) \\ &= \left(\frac{1}{2}\frac{B_2}{B_0} - \frac{3}{4}\frac{B_1\xi}{B_0 C_2 d_{char}}\right)\left(\rho_2^2 - \rho_1^2\right) \\ &=: \nu_{L,B_1}^{rel}. \end{aligned} \tag{9.10}$$

The additional uncertainties are now all summarized in the term scaling with the above-defined factor ξ. The final shift to consider is the same radial difference as mentioned before in the presence of B_2. This leads to additional individual shifts in the ν_L of the ions as

$$\left.\frac{\Delta\nu_L}{\nu_L}\right|_{B_2} = \frac{-B_2}{2B_0}r^2. \tag{9.11}$$

As a relative shift with respect to the measured Larmor frequency difference, this can be written as

$$\begin{aligned}\left.\frac{\Delta(\Delta\nu_L)}{\nu_L}\right|_{B_2} &= \frac{\Delta\nu_{L_2} - \Delta\nu_{L_1}}{\nu_L} \\ &= -\frac{1}{2}\frac{B_2}{B_0}\left(\rho_2^2 - \rho_1^2\right) \\ &=: \nu_{L,B_2}^{rel}.\end{aligned} \tag{9.12}$$

Combining these shifts, $\nu_{L,B_2}^{\mathrm{rel}}$ and $\nu_{L,B_1}^{\mathrm{rel}}$, results in

$$\begin{aligned}\frac{\Delta(\Delta\nu_{L,tot})}{\nu_L} &= \nu_{L,B_1}^{rel} + \nu_{L,B_2}^{rel} \\ &= \left[\frac{1}{2}\frac{B_2}{B_0} - \frac{3}{4}\frac{B_1\xi}{B_0C_2d_{char}} - \frac{1}{2}\frac{B_2}{B_0}\right]\left(\rho_2^2 - \rho_1^2\right) \\ &= -\frac{3}{4}\frac{B_1}{B_0C_2d_{char}}\xi\left(\rho_2^2 - \rho_1^2\right) \\ &\overset{(9.8)}{=} -\frac{3}{4}\frac{B_1}{B_0C_2d_{char}}\frac{4}{3}\frac{B_0C_2d_{char}\upsilon_z^2}{B_1\nu_+^2}\frac{\epsilon_{mag}}{r_+^2}\left(\rho_2^2 - \upsilon_1^2\right) \\ &= -\frac{\upsilon_z^2}{\upsilon_+^2}\frac{\epsilon_{mag}}{r_+^2}\left(\rho_2^2 - \upsilon_1^2\right) \\ &= 6 \times 10^{-13}.\end{aligned} \tag{9.13}$$

Note the sign change due to $\rho_1 > \rho_2$. In the ideal case, where the trap was tuned such that neither magnetron nor cyclotron excitations produce shifts of the measured axial frequency υ_z, it is thus found that the final difference of the Larmor frequency is also not shifted at all, when considering the dominant contributions of C_3, C_4, B_1 and B_2.
The determined systematic shift due to the measured dependency of $\frac{\epsilon_{mag}}{r_+^2} \approx 0.63(17)$ (see section 6.3.2) corresponds to $\frac{\Delta(\Delta\nu_{\mathrm{L,tot}})}{\Delta\nu_{\mathrm{L,tot}}} = 6 \times 10^{-13}$, which is corrected for in the final result. This has been additionally confirmed by performing two measurements on different separation distances, of $d_{\mathrm{sep}} = 340\,\mu\mathrm{m}$ and $d_{\mathrm{sep}} = 470\,\mu\mathrm{m}$. Both measurements have been in agreement after correcting for their respectively expected systematic shift. The uncertainty of this correction of 5×10^{-13} has been evaluated numerically by combining the uncertainties of ϵ_{mag} and the radii intrinsic to its determination, an uncertainty of δ_{mag} and the potential of a systematic suppression of the systematic shift by a residual common mode radius (see the work of Thompson [84]).

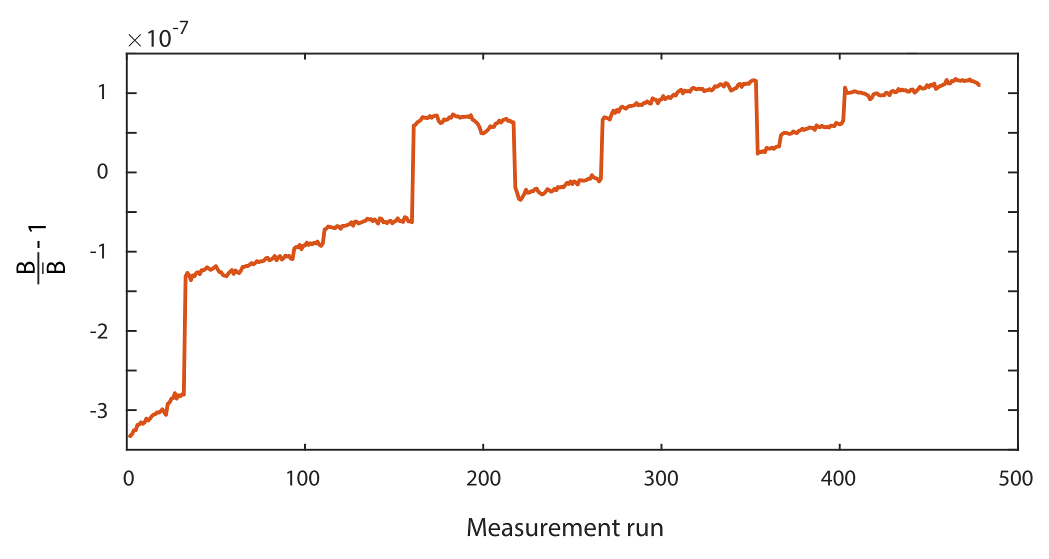

Figure 9.1: The relative change of the magnetic field over the course of the full Δg measurement campaign. The relative change of less than 5×10^{-7} is of no concern for the measurement. The abrupt changes correspond to interruptions of the measurement and the filling of cryogenic liquids.

Magnetic Field for the Δg Measurement

Here, the magnetic field, determined via the free cyclotron frequency measurement of $^{20}\mathrm{Ne}^{9+}$ during every measurement run, is shown for the full duration of the Δg measurement. All immediate jumps in the measurement correspond to longer interruptions of the measurement. The largest deviations are additionally related to the filling of liquid helium and nitrogen. After each measurement interruption, the magnetic field is once determined manually before starting the measurement cycle, required to use the correct microwave frequency for such an initial run.

The complete relative change of the magnetic field, $\frac{B}{\bar{B}} - 1$, is of less than 5×10^{-7}. This change is of no concern with respect to the determined Larmor frequency difference yet, otherwise the extracted phases could easily be corrected for such a drift as well.

Acknowledgments

Mit Abgabe dieser Arbeit bin ich nun bereits seit beinahe 8 Jahren ein nicht loszuwerdendes Mitglied der Gruppe Blaum, bzw. von ALPHATRAP. Dafür gibt es mehrere Gründe, aber in erster Linie liegt das sicher daran, wie zufrieden ich mit der Arbeit hier am Institut und vor allem der Arbeitsatmosphäre war, die ich hier erleben durfte.
Mein Dank im Folgenden gilt damit nicht nur den speziell hervorgehobenen Personen, die mich während meiner Promotion begleitet und geholfen haben, sondern auch nochmals allen, die mich auch schon davor auf diesen Weg gebracht haben.

Ganz vorne dabei ist hier natürlich **Klaus**.
Lieber Klaus, seit langen Jahren darf ich das angenehme und unkomplizierte Arbeiten mit dir genießen. Ich finde es besonders schön, dass du die einzelnen Personen deiner großen Abteilung nicht aus dem Blick verlierst, sondern zu jeder Zeit den Status aller Leute kennst. Zu jeder Zeit hatte ich das Gefühl, mich mit Problemen an dich wenden zu können. Dabei schaffst du es nicht nur innerhalb von meistens Minuten(!) zu antworten, sondern häufig auch direkt eine Lösung anbieten zu können.
Deine Betreuung und das Arbeiten mit dir während Bachelor und Master hat die Entscheidung auch meine Promotion mit dir als Doktorvater zu beginnen einfach gemacht und ich zweifle nicht daran, dass das die beste Wahl war, die ich dafür treffen konnte.
Danke für deine langjährige Unterstützung, das Vertrauen und die Möglichkeiten, die du mir und anderen Doktoranden bieten kannst. Vielen Dank.

Ebenso wichtig warst auch du, **Sven**.
Bei jedem Gespräch mit dir gibt es immer wieder Neues zu lernen. Es ist einfach beeindruckend, wie du in jeder Situation direkt Ideen hast, um Probleme anzugehen oder neue Methoden umzusetzen. Ich bin dir sehr dankbar für deine zahlreichen (und anschaulichen!) Erklärungen, die mich mehrfach wieder einen Schritt weiter bringen konnten. Während der vielen Jahre und nun drei absolvierten Arbeiten in deiner Gruppe wurde es nie langweilig, sondern gab immer wieder neue Erkenntnisse und Aufgaben.
Mit dir zu arbeiten war stets spannend und hat vor allem Spaß gemacht und ich bin mir sicher, dass es dir auch in Zukunft nicht an neuen und genialen Ideen für ALPHATRAP

mangeln wird. Danke für die gemeinsame Zeit, all dein vermitteltes Wissen und dafür, dass du für Vorschläge und Ideen stets offen bist. Zuletzt auch ein Dank für die schönen Gruppenabende bei dir und natürlich das stets ehrenhafte Einlösen von Wettschulden!
Ich bin mir sicher, von Dir, LIONTRAP und natürlich ALPHATRAP in den kommenden Jahren noch viel zu hören und wünsche dir das Allerbeste. Danke.
Lieber Herr **Quint**, Ihnen gilt an dieser Stelle der besondere Dank für die Übernahme des Zweitgutachtens und ebenso auch für Ihr Empfehlungsschreiben, durch das ich Mitglied der IMPRS-QD wurde. Vielen Dank für die Mühe und Zeit, die solch eine Aufgabe mit sich bringt.
Vielen lieben Dank auch an dich, **Gabi**. Mit deinem Organisationstalent sorgst du überhaupt dafür, dass es immer rund läuft. Danke, dass du immer mit Rat zur Seite stehst und es für dich ganz natürlich ist, immer direkt zu helfen. Einen besonderen Dank auch nochmal für dein Engagement während der letzten MATS-Tage – die Organisation der Gleitschirmlieferung deiner Schwester im Porsche war dabei natürlich mein absolutes Highlight.
Mein großer Dank gebührt auch allen Mitgliedern der ALPHATRAP Gruppe, aktuell und ehemalig. Durch die Vorarbeit meiner ehemaligen Kollegen konnte ich gut vorbereitet an einem bereits funktionierenden Experiment starten.
Speziell hier ein Dank an **Andreas** und **Ioanna** für das Weitergeben eurer Erfahrung und die Arbeit, die ihr bereits in das Experiment gesteckt habt. Hierdurch war der Umfang dieser Ergebnisse überhaupt erst ermöglich.
Vielen Dank auch an **Martin**, du hättest zu keiner besseren Zeit ein Teil von ALPHATRAP werden können. Ohne deine Beiträge zum Control-System und der strukturierten Umsetzung wäre die Arbeit mit zwei Ionen sicher noch komplizierter gewesen. Vielen Dank auch für deine Erklärungen, mit denen du es so oft geschafft hast, komplizierte Probleme in ein verständliches Licht zu rücken. Es war beeindruckend und hilfreich, wie du deinen Blickwinkel auf Probleme ändern, erklären und weitergeben konntest. Danke dafür. Dein Blog war natürlich auch sehr hilfreich.
Ein großes Dankeschön auch an meinen langjährigen Kollegen und guten Freund **Alex** – ohne dich wäre die Zeit am Institut bestimmt nicht so spaßig gewesen. Auch die Diskussionen im Bezug zur Arbeit haben mich immer wieder einen Schritt weitergebracht. Ich wünsche dir und Ale das Beste für eure gemeinsame Zukunft.
Last but not least among the former members of ALPHATRAP is **Bingsheng**. It has been an amazing time working with you, thank you for all the hours spend together, optimizing ion beams and loading them into the trap. Thank you for all the support when handling ion production, all the analysis you checked for me and all the discussion we had. I wish you the best for your new experiment!

Auch der neuen Generation von ALPHATRAPPERN möchte ich danken: Vielen Dank **Fabian**, für deine Unterstützung bei meinen Messungen. Deine Recherchekünste haben nicht wenige Probleme lösen können und es ist immer wieder toll, wie du für jede Situation das richtige Paper aus dem Ärmel schüttelst. Ich bin mir sicher, dass zukünftige Mitglieder ebenso von deiner Hilfe und Übersicht profitieren werden.
Danke **Jonathan**, du hattest die große Lücke eines fehlenden Bürokollegens zu füllen, der du aber offensichtlich absolut gewachsen bist. Deine riesige Begeisterung für die Physik ist dir täglich anzumerken und wird dir sicher helfen, die kolossale Aufgabe des Umbaus der Hyper-EBIT zu meistern. Danke für die großartigen Monate im Büro und die (beinahe) Großmeister-würdigen Schachabende. Ebenso auch ein Danke an **Chralotte**[a], dein Humor (gewollt und vor allem ungewollt) hat den Alltag und vor allem die letzten Monate der Schreibphase deutlich aufgelockert. Deine Art Probleme anzugehen ist erfrischend und ich habe keinen Zweifel, dass du deine Messungen erfolgreich umsetzen wirst. Ich wünsche dir das Allerbeste – und vor allem funktionierende Pumpen – für deine weitere Doktorandenzeit.

Ein großer Dank gebührt auch dem Team von PENTATRAP. Die Kooperation und der Austausch unserer Gruppen ist sicherlich ein wichtige Basis der zahlreichen genialen Ergebnisse. Speziell möchte ich **Sergey**, und vor allem **Kathrin** und **Menno** dafür danken, dass ihr einen Teil eurer generell üblichen, chronisch zu knappen Messzeit für die Messung der Neon Masse verwendet habt. Dafür herzlichen Dank und ein lautes MOIN!

Ebenso ein großes Danke an **Sascha**, für die zahlreichen Diskussionen, Programmiertipps und -hilfen und vor allem die extrem aufmerksame Durchsicht vieler Seiten dieser Arbeit. Ich wünsche dir viel Erfolg für deine Zukunft.

Zuletzt auch einen Dank an alle, die das Institut am laufen halten und den alltäglichen Problemen eines Doktoranden begegnen. Vielen Dank Herr **Klaiber**, dass Sie Ihre Aufgaben um den sicher nicht einfachen Zeitplan der Wissenschaftler planen. Vielen Dank an Herrn **Wagner**, dass Sie unseren Elektronikbasteleien mit Rat und Tat zur Seite stehen und mir bei vielen Fragen weiterhelfen konnten. Vielen Dank auch an Herrn **Spranz**, der die ständigen Notfälle einer dringend benötigten Fertigung immer passend einzuplanen weiß, und ebenso an Herrn **Zeiske**, der selbst für die kleinen Sorgen direkt seine Säge anwirft. Zum Schluss hier auch einen Dank an **Christian Kaiser & Team**, die mir mehrfach spontan und umkompliziert aushelfen konnten.

Vielen Dank auch dir, **Lena**. Ich weiß, dass der Stress dieser Arbeit auch an dir nicht

---

[a] Not a typo.

vorbei gegangen ist. Danke für deinen Beistand, die gemeinsame Zeit und dein Verständnis, vor allem in Wochen und Monaten der Messkampagnen und dem Schreiben dieser Arbeit. Danke, dass du immer für mich da bist.

Abschließend möchte ich **meinen Eltern** danken. Ohne euch wäre ich nicht da angekommen, wo ich heute stehe. Danke für eure uneingeschränkte Unterstützung und euer Vertrauen.